UNIVERSITY OF OKLAHOMA

GRADUATE COLLEGE

CHARGE STRUCTURE AND LIGHTNING PATTERNS IN A SIMULATED MESOSCALE CONVECTIVE SYSTEM

A DISSERTATION

SUBMITTED TO THE GRADUATE FACULTY

in partial fulfillment of the requirements for the

Degree of

DOCTOR OF PHILOSOPHY

By

ALLISON SILVEIRA
Norman, Oklahoma
2016

CHARGE STRUCTURE AND LIGHTNING PATTERNS IN A SIMULATED MESOSCALE CONVECTIVE SYSTEM

A DISSERTATION APPROVED FOR THE
SCHOOL OF METEOROLOGY

BY

Dr. Jerry Straka

Dr. Edward Mansell

Dr. Michael Biggerstaff

Dr. Lance Leslie

Dr. Sheena Murphy

Dr. Conrad Ziegler

Acknowledgements

I must first whole-heartedly thank my advisor, Dr. Ted Mansell, for his unwavering patience and guidance. From an early pep talk modestly describing himself as knowing a little about a lot of things, it turns out he knows a lot about a lot of things. Having a walking encyclopedia in an office across the hall made life much easier. Beginning to end, this was not possible without his help and encouragement.

I would also like to thank my chair, Dr. Jerry Straka, for his support since I entered the program as a Master's student. He is someone I have always been able to ask a stupid question, and the friendship I have with him and his wife, Dr. Kathy Kanak, has kept me afloat during periods of discouragement. Their collective curiosity is enough to inspire any budding scientist.

The many phases of my committee must also be acknowledged. I would like to recognize early members Drs. Bill Beasley and Stewart Ryan for their time on my committee through my General Exam. Likewise, the feedback and communication from Drs. Mike Biggerstaff and Conrad Ziegler has proved indispensable. I must also acknowledge newer members Drs. Lance Leslie and Sheena Murphy, who were kind enough to step in with relatively short notice. Conversations with both Lance and Dr. Pete Lamb played a big part in my decision to stay on for my doctorate.

In addition to the help from my committee, I would like to thank Dr. Don MacGorman for all of his input. Despite having a seemingly infinite depth of knowledge, he was an invaluable resource and was able to give suggestions in a way that was never intimidating. I could not have completed this work without the help of Henry

Neeman, the Director OSCER, who would always find time to help while I was porting the model to MPI. I also must thank Dr. Mike Buban, who has one of the most curious scientific minds I know.

Finally, I would like to thank my family in various forms: My mother for making me who I am, my grandfather for being someone to aspire to, my step-father for being one of the biggest influences on my academic success, my children for giving me a reason to set a good example, and my husband for doing everything he could to make sure I saw this through.

Table of Contents

List of Tables

List of Figures

Abstract

Observational analyses of electric field measurements and inferred charge structure within the stratiform region of a mesoscale convective system (MCS) repeatedly reveal quasi-steady, horizontal charge layers at and above the melting level. Previous studies have concluded charge advection can explain the uppermost layers as charged ice particles are ejected from the convective line into the weaker downdrafts of the transition zone. These layers have been observed to slope through and persist beyond the transition zone into the weak, broad mesoscale updrafts of the stratiform region. Likewise, significant electric fields are consistently measured in the layer below -10°C through the melting level, indicative of appreciable charge density, yet are apparently independent of the convective line. The contribution of several possible charge separation processes to the generation and maintenance of charge layers near the melting level are examined in this study. A high-resolution, three-dimensional model with full dynamics and two-moment microphysics was employed. The cloud microphysics were improved to include the prediction of liquid water fractions on graupel and snow to better parameterize the hypothetical charge separation mechanisms.

Similar structure to the standard conceptual model of a leading-line, trailing stratiform MCS was exhibited in the model solutions with respect to observed kinematics, microphysics, and charge. In contrast with earlier two-dimensional modeling studies, charge advection did not account for any appreciable charge beyond the transition zone. However, through use of the new mixed-phase particle microphysical scheme, a charging mechanism associated with particle melting was found to be capable of

simulating widespread, appreciable charge near the melting level of the stratiform region.

Chapter 1

Introduction

Mesoscale convective systems (MCSs) are prodigious producers of many types of meteorological phenomena affecting vast areas, including hazards such as hail events, high winds, and frequent lightning (Fritsch et al. 1986; Goodman and MacGorman 1986). While individual MCSs have different kinematic, microphysical, and electrical features, an archetypal form is the so-called leading-line, trailing-stratiform (LLTS) MCS (e.g., Rutledge et al. 1988; Parker and Johnson 2000), wherein a propagating convective line leads the stratiform region, separated by a transition zone. These types of storms are also considered symmetric MCSs, whereas asymmetric MCSs have more of a comma shape resulting from Coriolis forcing, with a bowed convective line and the stratiform region favoring one end of the bow.

Studies have shown repeatable cloud-to-ground (CG) lightning polarity patterns and vertical charge structure within various sections of LLTS MCSs (e.g., Goodman and MacGorman 1986; Stolzenburg et al. 1994). In these electrically active squall-lines, the convective line typically has a much larger CG flash rate than the trailing stratiform region, where often the CG flashes are of positive polarity, whereas the convective line contains primarily −CG flashes (Goodman and MacGorman 1986; Rutledge and MacGorman 1988; Orville et al. 1988). Interestingly, large-current positive CG flashes in the stratiform region are also linked to certain types of transient luminous events (TLEs), such as sprites, a mainly red vertical discharge column in the upper atmosphere above the flash, and elves, a rapidly expanding red disk that occurs in or near the ionosphere (Sentman et al. 1995; Lyons et al. 1998).

Many observational studies have been conducted to examine the electrical properties of MCSs using a variety of lightning detection and mapping techniques, as well as surface and sounding electric field meter (EFM) information. Electric field data have demonstrated horizontally consistent charge layers that are steady in both space and time through the depth of the storm (Stolzenburg et al. 1994, 1998). The persistence of these layers suggests the charge regions are used as a conduit for both intracloud (IC) and CG lightning with a steady charge separation mechanism to maintain the layers.

Total lightning (IC and CG) data from very high frequency (VHF) radiation sources detected by Lightning Mapping Arrays (LMA), in conjunction with National Lightning Detection Network (NLDN) data for CG flashes, allow for a consistent qualitative representation of the inferred location of charge with better spatial and temporal coverage than EFM soundings. The LMA data tend to show that the positive CG flashes that strike ground within the stratiform region often initiate in the convective line (Lang et al. 2004), but propagate through horizontally expansive layers of charge that extend nearly the width of the MCS (Dotzek et al. 2005; Carey et al. 2005). Recent total lightning observations show that as the storm matures, however, there can be a significant increase in the number of flashes originating from the stratiform region, as well as a general increase in the number of positive CG flashes (Hodapp et al. 2008).

With continued observational investigations regarding the source of the charge layers in the stratiform region, more insight regarding active processes has been pursued through numerical modeling, albeit limited to a single two-dimensional study. Schuur and Rutledge (2000a,b) found that consistency between two-dimensional model results and observations required that charge advection be included. Additionally, charge structure near the melting level in the stratiform region only demonstrated the quasi-horizontal layer structure when *in situ* charge separation processes were included, though results from the two non-inductive (i.e., does not require an ambient electric field) collisional schemes presented had discrepancies with observation.

Much remains to be understood about the dynamics, microphysics, and electrification of the stratiform region of an MCS, including the processes leading to the mesoscale updraft. The observed broad, weak updraft located above the 0°C isotherm can lead to ice and water supersaturation, and the presence of supercooled water droplets. The collocation and coexistence of significant charge layers with a bright band in radar reflectivity (indicative of melting snow aggregates) suggests that melting may play a role in charge processes (Shepherd et al. 1996). One possibility for charge generation by melting was tested with the 2-D Schuur and Rutledge (2000b) model, but will be re-evaluated here with a higher-resolution 3-D dynamical model. Understanding the processes affecting the charge structure near the melting level of the stratiform region is a critical component in the explanation of positive CG flashes that occur in that region of MCSs.

1.1 Previous Research

1.1.1 Observation

1.1.1.1 Mesoscale Convective Systems

The decade of the 1980s was a prolific period for observational studies of mid-latitude squall-line systems. Early in this period, composite rawinsonde data and emerging dual-doppler velocity techniques painted a basic understanding of flow fields for individual tropical and continental case studies (e.g., Ogura and Liou 1980; Smull and Houze 1987a). Toward the end of the decade and into the next, much of this research benefited from data collected during the Preliminary Regional Experiment for STORM-Central (PRE-STORM) field experiment (Cunning 1986). At the turn of the century, the Bow-echo and MCV Experiment (e.g., BAMEX; Davis et al. 2004) looked at particular features of primarily asymmetric MCSs, although some of the analysis is applicable to LLTS-type MCSs.

Some of the initial publications from the PRE-STORM experiment revolved around the role of the rear-to-front flow. Smull and Houze (1987b) noted that in many instances, peak horizontal velocities at mid-levels (≈550mb) near the rear of an MCS exceeded the storm translation speed, reaching nearly $17\,\mathrm{m\,s^{-1}}$. This "rear inflow jet" (RIJ) appeared to control the breadth of the stratiform rain region by penetrating the storm with drier environmental air. Additionally, the authors suggested the rear inflow could be driven by processes occurring within the MCS, and not necessarily forced by environmental flow.

Rear-to-front inflow was linked to the presence of a mesoscale downdraft in the trailing stratiform region by the case study analysis of Rutledge et al. (1988). Interestingly, a mesoscale downdraft was evident above the 0°C isotherm at the interface of the front-to-rear and rear-to-front flows, although most intense at the melting level. Their analysis suggested that the intensity and dryness of the RIJ varied in tandem with the intensity of the mesoscale downdraft. This led to the conclusion that the mesoscale downdraft was a consequence of evaporation and sublimation enhanced by the dry inflow.

Houze et al. (1989) summarized the contemporaneous knowledge of typical MCSs into a conceptual model, replete with characteristic pressure fields, and bolstered by radar imagery (Fig. 1.1). The study showed a clear separation of the reflectivity maxima in the convective line from the secondary maxima in the stratiform region by the reflectivity minimum in the transition zone. The conceptual model of a LLTS MCS was more fully developed by Biggerstaff and Houze (1991), who added microphysical detail as well as possible particle trajectories (Fig. 1.2). Moreover, the authors differentiated the breadth and probable forcing of the mesoscale downdraft from that of the mesoscale updraft. The shallower, more intense mesoscale downdraft is likely related to precipitation dynamics, primarily from evaporative cooling and latent heat of melting (Leary and Houze 1979), whereas the mesoscale updraft may feasibly result from the large-scale motion of trailing stratiform cloud. As the conceptual model of Biggerstaff and Houze (1991) was built from that of Houze et al. (1989), both are still frequently referenced as squall-line archetypes.

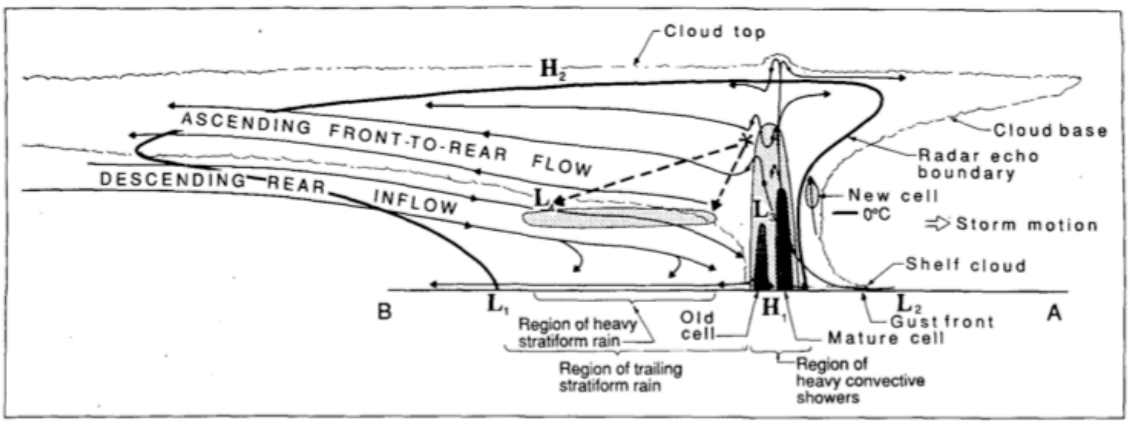

Figure 1.1: Conceptual model of a mesoscale convective system. Source: Houze, et al., 1989.

1.1.1.2 Electrification

Two main aspects of electrification observations apply to thunderstorm research. One is laboratory experiments involving charge separation of individual or colliding particles, the other is *in situ* measurements of electrical properties within a storm via sounding data and lightning detection. As the laboratory experiments provide a background for charge separation hypotheses for observed storm systems, it is prudent to begin this summary with pivotal laboratory research.

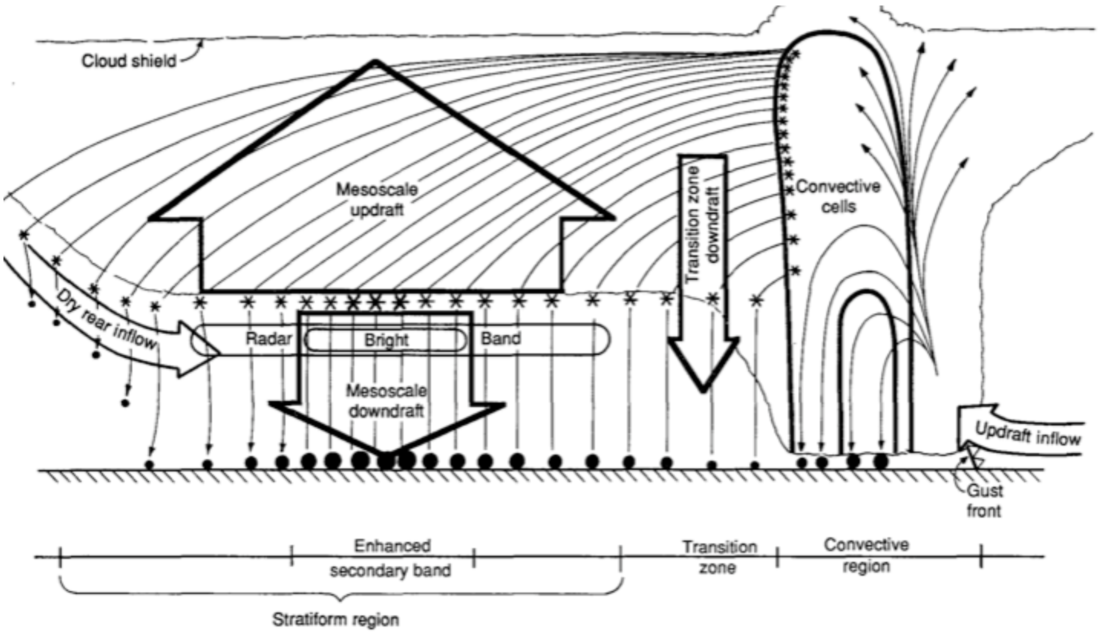

Figure 1.2: Conceptual model of a mesoscale convective system. Source: Biggerstaff and Houze, 1991.

Non-inductive, ice-ice collisional charge transfer requires that two particles contact each other then nearly instantaneously separate, with each particle carrying off opposite charge polarity through mass transfer (Mason and Dash 2000). Empirically, the polarity of the charge transfer depends primarily on the ambient liquid water content (LWC) and temperature, which effectively control the rime accretion rate in the presence of supercooled water (Reynolds et al. 1957). Takahashi (1978) tested various temperature and cloud water content (CWC) regimes to conclude that a riming graupel particle charges positively except at temperatures between $-10°C$ and $-30°C$, and approximate CWC of 2 to 4 $\mathrm{g\,m^{-3}}$ (Fig. 1.3). At very low CWC, below 10^{-1} $\mathrm{g\,m^{-3}}$, Takahashi (1978) did not find a secondary charge reversal temperature, a temperature at which the polarity acquired by a target alternates. Instead, the rimer rod was always positively charged for very low CWC.

To the contrary, Jayaratne et al. (1983) found that the riming target could acquire negative charge for lower temperatures at CWCs less than 2 $\mathrm{g\,m^{-3}}$. The results of

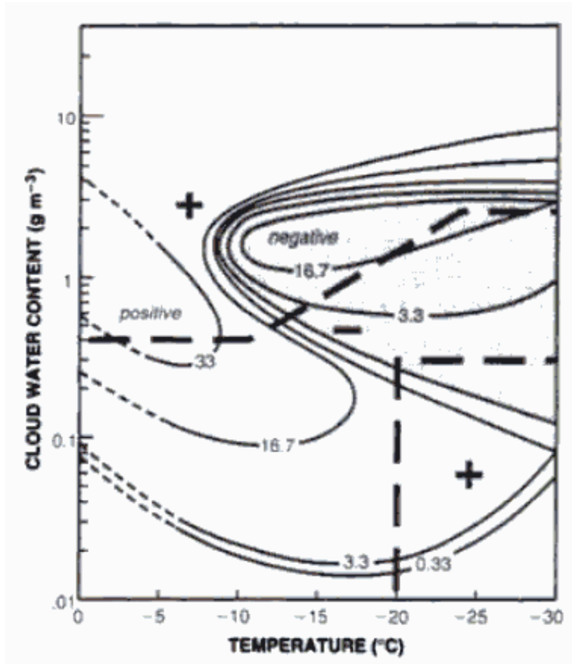

Figure 1.3: Composite plot of laboratory results for charge acquired by target graupel particle. Contours are interpolated from Takahashi 1987. Dashed lines are Saunders 1991 data, modified in terms of cloud water content.

Jayaratne et al. (1983) were supported by Baker et al. (1987), a follow-up study that included a theoretical hypothesis for charge transfer between graupel and ice based on the differential diffusional growth rates of the colliding particles. Now known as the Relative Growth Rate (RGR) hypothesis, the crux of the hypothesis proposed that for colliding graupel and ice particles, the particle growing faster by vapor deposition acquires positive charge during the collision. When the experimental results were put in terms of effective liquid water content (EW, the LWC multiplied by the collection efficiency) to incorporate collisional efficiency between the riming target and droplets, subsequent research found that low EW regimes demonstrated a charge reversal temperature, albeit with limited data points (Saunders et al. 1991; Saunders and Peck 1998). The data from the later studies were also intended to fill an anomalous zone at very low EW and temperatures, where data were sparse and inconclusive (Fig. 1.3). More recent work reproduced the low LWC charge reversal temperature (Saunders et al. 2001), although the technique of laboratory experiments for graupel charging seems to be a point of contention owing to experimental design and measurement techniques (Saunders et al. 2006).

An extension of the RGR hypothesis studied charging in regions free of liquid water, specifically at very cold temperatures (e.g., $<-40°C$; Mitzeva et al. 2006b). Although this was not a laboratory experiment, the study tested various signs and magnitudes of graupel-ice charge separation with a 1-D model. The results suggested that under ice-supersaturated conditions, in absence of liquid water, a weak ice-graupel charge separation mechanism could amplify charge densities in upper portions of deep convection. However, the authors note the modeled results are difficult to compare with limited, sometimes contradictory observations for charge in upper levels, in addition to the lack of experimental data. Furthermore, Mitzeva et al. (2006b) focused on the upper portions of convection, and the significance of this proposed mechanism to the ice-supersaturated areas in anvils or just above the melting level of the stratiform region would need further testing.

One non-inductive charging mechanism that does not require particle collisions is the theory of charge generation by melting suggested by Drake (1968), initially developed to explain the lower positive charge in thunderstorms. The theory relies on the existence of an electric double layer, a preferential transport of negative ions within a liquid particle toward the surface, with an inner layer of net positive charge. Essentially, Drake (1968) hypothesized that under some conditions air bubbles trapped in a frozen graupel-like particle rupture the electric double layer, leaving the graupel particle with positive net charge as small droplets break off with negative net charge. The results of the laboratory study indicated that the charging was dependent on internal convection currents in melting graupel, which may or may not be realistic for particles not in isolation, thus likely to be involved in collisions. Additionally, the laboratory experiments used graupel-like pellets, and the results may not be applicable to melting snow aggregates. In either case, melting occurs over a shallow layer in the stratiform region and it is possible this mechanism could be a significant contributor to charge generation.

Considerable attention has been given in literature to the electrification of convective storms, including the convective line of an MCS, as those types of storms are frequent lightning producers. The laboratory experiments established that non-inductive, graupel-ice collisional charge separation can largely explain observed main charge regions within convective zones of thunderstorms, and with the appropriate time scales. As the linkage between the convective line and the stratiform precipitation was being established in a kinematic and microphysical sense (see previous discussion), similar interest developed for the relatively unknown charge structure of the stratiform region. This was further motivated by the identification of a "bi-polar" pattern to CG strikes, in which −CG strikes tend to occur mainly in the convective region and +CG strikes are more common behind the line and in the stratiform region (Goodman and MacGorman 1986; Rutledge and MacGorman 1988).

Radiosonde and EFM data from balloon launches through all regions of various MCSs revealed significant charge layers in the transition zone as well as the stratiform region (e.g., Schuur et al. 1991; Hunter et al. 1992). The charge structure of the stratiform region was more complex than the "normal" or "inverted" tripole models of thunderstorms (Williams 1989; MacGorman and Rust 1998), having four or more significant charge layers. These charge layers were horizontally extensive, spanning most of the length of an MCS line-perpendicular cross-section (Hunter et al. 1992).

After more EFM soundings were made available by the Cooperative Oklahoma Profiler Studies experiment (COPS-91; Jorgensen and Smull 1993), Marshall and Rust (1993) distinguished recurring electric field structures of the stratiform region into two modes: Type A and Type B (Fig. 1.4). Type A soundings were representative of LLTS MCSs, with five main charge regions. Type B soundings, representative of asymmetric MCSs, typically only contained four main charge regions. A noted difference between the two types was the polarity of significant charge regions near the 0°C isotherm. For Type A soundings, negative charge was found at the melting level, whereas positive charge was predominant for Type B soundings. The overall polarity and depth of the lower two main charge regions for both sounding types were not vastly different, but the location of the 0°C isotherm was used for categorization purposes, and similar structure was found by other studies (e.g., Bateman et al. 1995; Shepherd et al. 1996).

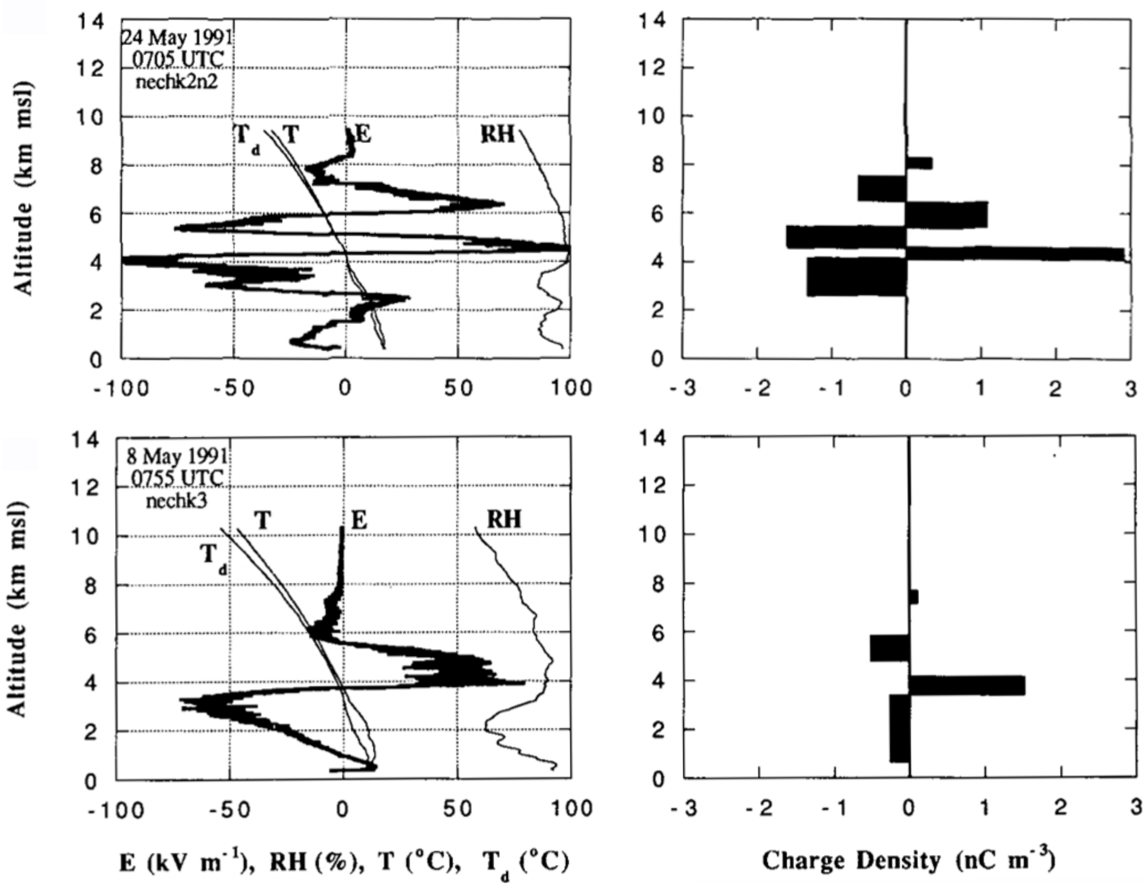

Figure 1.4: Sounding data from the COPS-91 experiment, including temperature, dew point, electric field, and relative humidity. Charge density was calculated from the vertical component of electric field measurements. Source: Marshall and Rust, 1993.

In addition to providing a useful classification tool, the COPS-91 project sampled MCSs at a higher spatial and temporal scale than previously available. An analysis of five soundings from one particular storm during the experiment supported the assertion that charge layers in the stratiform region are horizontally extensive and select layers are consistent with the convective line (Stolzenburg and Marshall 1994). The slope of continuous charge layers from the convective line into the stratiform region also supported earlier arguments that the charge layers found in the transition zone and stratiform region resulted from charge advection (e.g., Rutledge and MacGorman 1988). In contrast, the layer at 0°C in the stratiform region was not consistent with any particular polarity of charge, yet persisted at nearly the same level throughout the soundings (Fig. 1.5, Stolzenburg et al. (1994)).

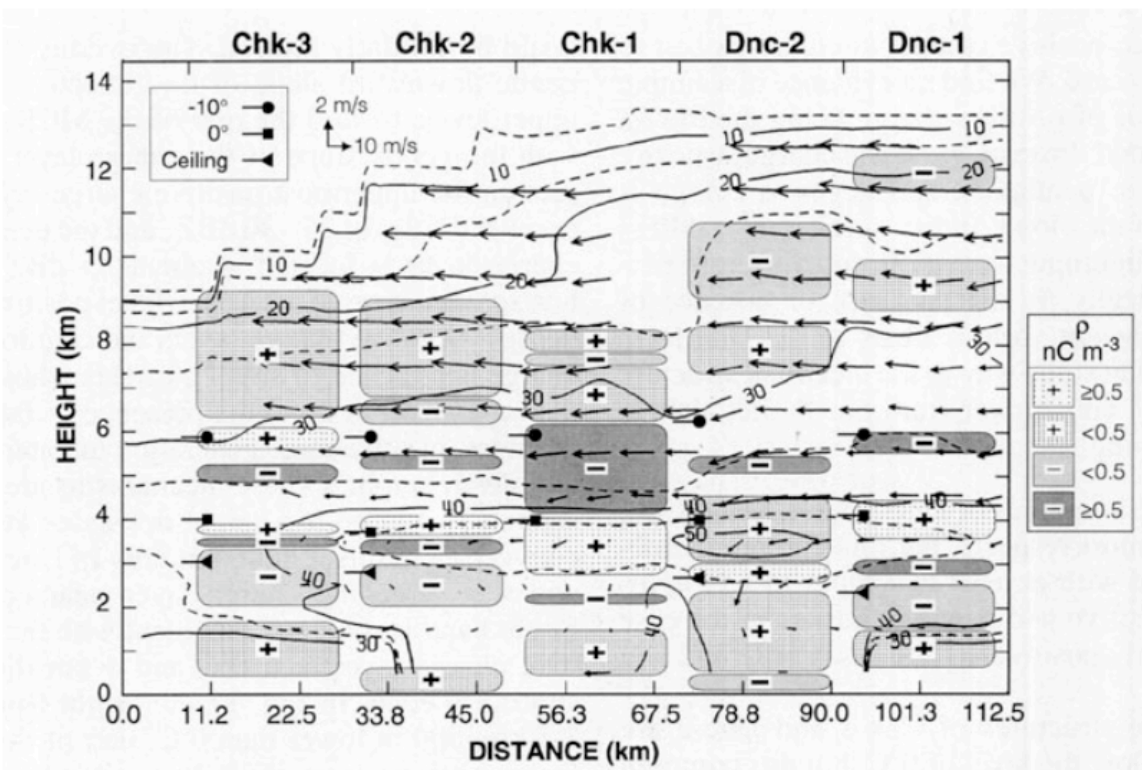

Figure 1.5: Interpreted charge structure overlaid with reflectivity data for an MCS that occurred on 2-3 June 1991. Source: Stolzenburg et al., 1994.

The observations of quasi-steady layers not originating from the convective line led to the hypothesis that an *in situ* process is likely occurring (Marshall and Rust 1993; Bateman et al. 1995; Shepherd et al. 1996). Specifically, Shepherd et al. (1996)

suggested a melting charge generation process based on the collocation of the bright band, isothermal layer, and large charge densities in the stratiform region. The measurements of Bateman et al. (1995) indicated the appreciable negative charge inferred was likely carried by small particles, whereas larger precipitation particles carried positive charge. The possible contributions of charge advection, noninductive graupel-ice collisional charge separation, and melting charge generation were considered by Schuur and Rutledge (2000a,b) in a two-part study analyzing COPS-91 data and comparing results with numerical simulations.

The observational portion of Schuur and Rutledge (2000a) compared microphysical data with EFM soundings of two MCSs to determine the likelihood of *in situ* charge separation as a significant mechanism leading to typical charge structure. A key result of their study was that the trailing stratiform region just behind the convective line and transition zone of a symmetric MCS was more favorable than the asymmetric case to non-inductive, *in situ* charging owing to the presence of supercooled water above the melting level in the relatively stronger mesoscale updraft. A 2-D kinematic model simulating the symmetric case suggested that non-inductive charge separation could account for up to 70% of the charge density in the stratiform region (Schuur and Rutledge 2000b), and will be discussed in more detail in section 3b.

The positive charge layer near the melting level in the stratiform region is thought to have a key role in most +CG lightning, thus identification of these regions is critical to the understanding of stratiform +CG initiation (Orville et al. 1988; Rutledge and MacGorman 1988; Stolzenburg and Marshall 1994). Although positive charge densities are inferred in numerous EFM soundings near the melting level (Stolzenburg and Marshall 1994; Bateman et al. 1995; Shepherd et al. 1996; Marshall and Stolzenburg 2001; Stolzenburg et al. 2001), if there is a charging mechanism active on a small spatial or temporal scale creating these local charge regions, such a mechanism may not have been reproducible by past low-resolution numerical models, either through microphysical or charging parameterizations. This is particularly relevant to a melting charging mechanism, as melting of precipitation occurs over a shallow layer (on the order of 500-1000 m) that is poorly resolved on coarser grids (e.g., Δz= 400 m in Schuur and Rutledge 2000b).

1.1.1.3 Lightning

Studies of mesoscale convective systems are an integral part of lightning research as these systems often exhibit high flash rates and copious amounts of lightning over the lifetime of the storms Goodman and MacGorman (1986). Analyses of data from CG lightning detection instrumentation suggest that flashes tend to occur in a bipolar pattern in which −CG flashes are generally confined to the convective line and +CG flashes are less frequent, but dominate the stratiform region (Goodman and MacGorman 1986; Rutledge and MacGorman 1988; Rutledge et al. 1990). Concomitant with the demarcation of CG polarity across the horizontal extent of a system, vertical lightning structure contributes to our understanding of significant charge layers and generation mechanisms. Networks like the Oklahoma LMA can detect 3-D structure of both IC and CG flashes, inferring charge structure in a spatial sense that is difficult to capture with EFM data alone. For example, Carey et al. (2005) were able to identify two sloping charge layers that extended from the convective line through the transition zone. The flashes that corresponded with these charge layers often initiated in the convective line, extended through the stratiform region. In at least one instance a +CG flash terminated under the stratiform region.

Figure 1.6 illustrates the gentle slope of lightning sources, and therefore the inferred charge layers, through the transition zone, which became mostly horizontal above the melting level near the enhanced precipitation in the stratiform region (Dotzek et al. 2005; Carey et al. 2005). In a similar fashion, Ely et al. (2008) noted at

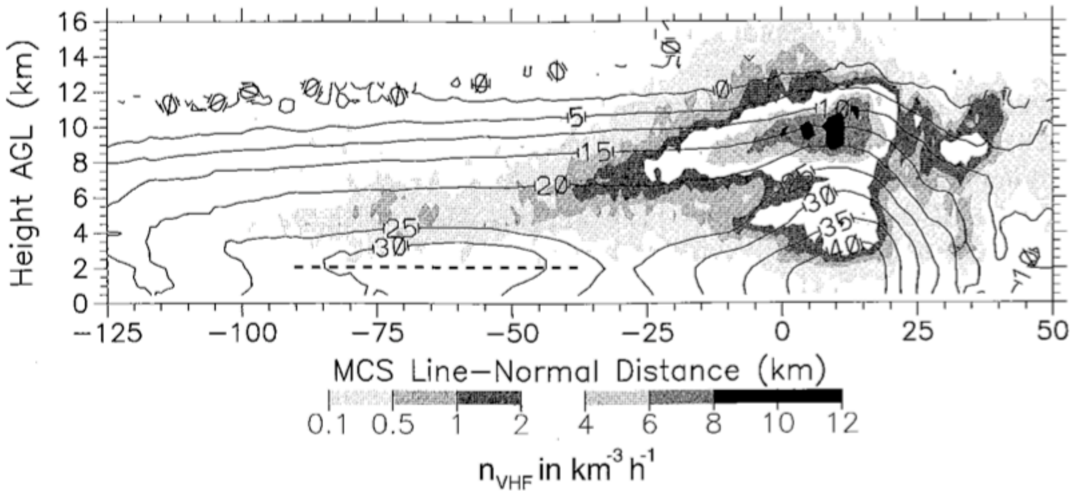

Figure 1.6: Lightning source density and reflectivity for an MCS that occurred on 8 April 2002. Source: Dotzek, et al., 2005.

early stages of MCS evolution, lightning paths tended to be more horizontal than at later stages when the slope increased to resemble the more slanted layers of previous research (e.g., Dotzek et al. 2005). Lang and Rutledge (2008) also corroborated the sloping charge layer evidence, as well as nearly horizontal lightning paths near the melting level.

With our current understanding of microphysical processes that are functioning in various regions of an MCS, differential particle sedimentation is at the crux of any charge separation argument (Schuur and Rutledge 2000b). This puts an emphasis on the geometry of the charge layers within LMA data, in particular, the way the slope or lack of slope relates to hydrometeors that are either sampled by probes or inferred via radar data. Dotzek et al. (2005) reasoned that the slope of the source region could be accounted for by assuming a steady storm motion and fall speeds typical of hydrometeors observed in the region just behind the convective line. Their calculations support the case for charge advection occurring behind the convective line, whereas it is unclear what charging mechanisms are operating in the horizontal layer near the melting level where charge is weaker, fewer collisions are occurring, and the distance from the convective line makes charge advection unlikely.

1.1.2 Numerical Modeling

Numerical models are useful tools when observations are limited or the feasibility of a hypothesis needs to be developed or tested. Early numerical investigations of MCSs focused mainly on the conditions necessary to sustain a squall line for the duration of their typical lifetimes (Thorpe et al. 1982; Rotunno et al. 1988; Fovell and Ogura 1988). In both two- and three-dimensions, with the latter having north-south periodic boundary conditions, the numerical studies found that low-level speed shear was required to sustain long-lived convection, where the circulation of the cold pool essentially balanced the ambient shear circulation. Though both models were fully dynamical, the microphysics were very simple and did not include ice phase particles.

In contrast, Rutledge and Houze (1987) developed a 2-D kinematic model to include the ice phase, but using two imposed wind fields derived from Ogura and Liou (1980) and Smull and Houze (1985). The study essentially supported the hydrometeor advection hypothesis of Smull and Houze (1985) through numerical solutions that modeled frozen particle advection from the convective line, which ultimately melted and precipitated in accordance with observed surface rain rate distributions. Their results reinforced the importance of representing frozen hydrometeors in microphysical parameterizations to more realistically reflect rain rates through the stratiform region.

Skamarock et al. (1994) elaborated on the model results of Rotunno et al. (1988) with a larger domain to simulate the full system without imposing periodic boundary conditions. But again, the model did not include an ice phase so the solutions were limited in their realism, but there was something to be gained qualitatively. In particular, this study was able to incorporate Coriolis forcing and substantiate its role in generating mesoscale convective vortices (MCVs) for asymmetric systems.

As shown by Bryan et al. (2003), finer resolution simulations of squall lines can better resolve entrainment of environmental air, which in turn leads to more realistic updraft widths and affects the microphysics and dynamics of the trailing stratiform region. The differences in resolution are apparent when comparing a 3-D squall-line simulation using 1000 m grid spacing with a simulation using 125 m grid spacing but filtered to 1000 m grid spacing. The filtered results indicated a narrow, cellular structure for the convective line, separated from the stratiform region, whereas the 1000 m simulation resulted in a wider, diluted convective line with marked differences from the filtered run. In weak shear without filtering, the 125 m simulation thermals carrier relatively higher θ_e air to upper levels of convection, whereas at 1000 m horizontal resolution the highest θ_e air never penetrated higher than mid-levels. Although the study did not show a qualitative convergence of modeled convection type with decreasing grid spacing, it demonstrated the need for finer grid spacing than the commonly used 1 km spacing.

Electrification adds a layer of complexity to thunderstorm simulations, particularly owing to the dependence of non-inductive charging on having an ice phase (Takahashi 1974, 1979, 1984). Early electrification modeling studied the possibility of warm rain charging using inductive charging and ion attachment (Chiu 1978). Though it is now generally understood ice is required for significant charging, the 2-D axisymmetric model was able to reproduce the normal dipole structure, with a lower positive charge later in the simulation. In addition to the 2-D studies with and without ice phase, Rawlins (1982) was also on the forefront of investigating thunderstorm charging mechanisms with a 3-D numerical model. The Rawlins (1982) study considered both non-inductive charging as well as an inductive charging mechanism and aimed to determine the efficacy of these mechanisms in reaching the electric field breakdown threshold. It was found that for thunderstorms, the non-inductive charging mechanism was capable of producing electric fields that reached the breakdown threshold for lightning in a time frame similar to what is actually observed. As in Takahashi (1984), the 2-D model of Helsdon and Farley (1987) incorporated small ion processes to replicate screening layers at cloud boundaries. Although a screening layer was not sampled by the aircraft E-field data they were attempting to simulate, screening layers are a regularly occurring phenomenon, thus the addition of small ion processes is beneficial.

More than a decade later, Schuur and Rutledge (2000b) used a two-dimensional kinematic model to test a variety of charging schemes specific to the stratiform region of an MCS. The flow field was initialized as an idealized version of the stratiform region, and a "buffer zone" was specified at the inflow boundary to replicate the convective line using heating, microphysical, and charge profiles across the rightmost five grid points (20 km) of the domain. Although this was a crude representation of the processes occurring in the convective line, using observed profiles of a typical squall line was suitable for testing their hypothesis concerning charge generation in the stratiform region.

The originality of the Schuur and Rutledge (2000b) study was to consider both charge advection and *in situ* charging as significant contributors to the charge structure of the transition zone and stratiform region, as hypothesized by concurrent observational studies. As stated previously, the authors found that up to 70% of the charge density could be attributed to a non-inductive charge mechanism, and the remainder was attributed to charge advection. Alternative charging mechanisms (e.g., Drake 1968) that do not require particle collisions were found to be insignificant in their results. There have been limited subsequent numerical modeling studies that explore the role of alternative non-inductive charging mechanisms, in particular melting charging or inductive charging, in charge structure evolution of the stratiform region.

For thunderstorms with significant charge, lightning modeling becomes a necessity to handle extreme charge densities. There are two main approaches for lightning parameterization: simple removal of charge from the system or a method that generates channels. Early implementations of lightning parameterization included removal of charge from the model domain once reaching a threshold (Rawlins 1982; Takahashi 1987; Ziegler and MacGorman 1994). Then, channel parameterizations began to add more details to the physics of lightning flashes and to the realism of the flash itself, beginning with the bidirectional breakdown model of Helsdon and Farley (1987) and Helsdon et al. (1992). Following that model, MacGorman et al. (2001) allowed the flash to propagate farther into regions of significant charge density. An even more complicated parameterization is that of Mansell et al. (2002), which used step-by-step stochastic methods to determine leader propagation given the ambient electric field. That model will be discussed in more detail in the next chapter.

1.2 Research Objectives

Despite advances in MCS observations, many questions remain, such as unknowns surrounding charging theory, and these questions are prime candidates for laboratory research and applied numerical modeling research. Although observations consistently show significant charge layers near the melting level, there is no consensus in the literature regarding the mechanisms responsible for the charge generation. Continuous, large spread *in situ* sampling of MCSs is extraordinarily difficult, if not impossible, given the typically large area they cover for a significant amount of time. Our understanding of gross charge structure has been improved by charge inference from LMA total lightning data. Simultaneous electrical and microphysical observations for the extent of an MCS are scarce, however. It is easy to argue that microphysics, in particular hydrometeor interaction, must be adequately explained to completely understand the generation of charge for any electrified storm.

With advances in technology leading to exponential increases in computational speed, we are on the forefront of a new era with larger domain sizes and higher resolution. These capabilities make fully 3-D MCS simulations feasible with appropriate grid spacing to resolve updraft elements and turbulence quantities. As discussed previously, Bryan et al. (2003) demonstrated the deficiencies of settling on greater than 500 m grid spacing for simulating squall lines. Additionally, much of the previous research regarding the melting level of MCSs was limited due to the large spatial extent of the full system compared with the fine vertical grid spacing needed to resolve the relatively thin melting layer. Computational cost also restricted many of these models to simplified microphysics, often neglecting larger ice hydrometeors. Alleviating the computational constraints allows for improved resolution of the microphysics near this shallow layer and therefore the charge generation that may subsequently occur. Ultimately, this research is motivated by the uncertainty of explanations for observed charge structure in the stratiform region, particularly near the melting level.

1.2.1 Main Hypothesis: The charge structure near the 0°C isotherm is significantly affected by charge generated as a result of melting hydrometeors.

The compendium of soundings in Shepherd et al. (1996) demonstrated the frequent collocation of the melting level with a significant charge region. As data collection improved (e.g., Stolzenburg et al. 2001) and LMAs broadened the continuity of data within charge layers, analyses suggested charge advection may be responsible for sloping charge layers just behind the convective line. The quasi-horizontal charge layer near the bright band is not always continuous with the convective line (e.g., Dotzek et al. 2005), yet it is sustained, suggesting a different mechanism is contributing to charge generation. This is further substantiated by Ely et al. (2008) who argue the strengthening of the mesoscale updraft can contribute to *in situ* charging, although they do not specifically implicate a melting charging process.

1.2.2 Alternate Hypothesis 1: The charge structure near the 0°C isotherm is significantly affected by charge generated as a result of depositional growth.

While non-inductive charging is certainly plausible and may likewise be active, laboratory studies suggest charge generated during particle melting can account for weak charge densities. Schuur and Rutledge (2000b) found mechanisms such as Drake (1968) and Dong and Hallett (1992) had insignificant effects on charge separation, however the shallowness of the melting layer may have limited adequate representation of charging by the model. Having access to a high-resolution model and newer microphysical and charging parameterization schemes warrants a revisitation of this hypothesis.

1.2.3 Alternate Hypothesis 2: The charge structure of the melting layer depends on inductive charging.

Inductive charging has not been thought to be a primary electrification mechanism for thunderstorms or MCS convective lines, owing to the low theoretical probability that particles collide in a favorable position relative to the electric field (e.g., Gaskell 1981; Brooks and Saunders 1994). Additionally, for inductive charging to be effective, an electric field must already be present, thus requiring another mechanism to be active. That said, some laboratory studies have shown that charge can be separated between an ice particle and liquid droplets in the presence of an electric field (Aufdermaur and Johnson 1972; Brooks and Saunders 1994), or possibly through raindrop "disjection" when drops collide but do not coalesce (Canosa and List 1993). If we assume that charge advection is responsible for the charge densities in the transition zone, and assume that *in situ* non-inductive charging is significant in the stratiform region near the 0°C isotherm, the criterion for a pre-existing electric field is met to make inductive charging a plausible, albeit secondary charge generation mechanism for the stratiform region.

1.2.4 Alternate Hypothesis 3: The charge structure near the 0°C isotherm results from *in situ* charging and, in particular, charging in a liquid-free, ice supersaturated environment.

In addition to ice-ice collisions and rebounding, non-inductive charging can depend on the presence of supercooled water droplets, leading to rimed surfaces on the graupel target. The kinematics of the stratiform region are such that a broad mesoscale updraft is often found just above the melting layer. The weak updraft on the order of 0.1 $\mathrm{m\,s^{-1}}$, may provide enough forcing that water saturation is maintained and small droplets become supercooled in the presence of other frozen hydrometeors. The resultant mixed-phase environment would be conducive to appreciable non-inductive charging.

This hypothesis was tested with the two-dimensional model of Schuur and Rutledge (2000b), who found that non-inductive charging could account for up to 70% of the total charge density. Their model used older Takahashi (1978) and Saunders et al. (1991) laboratory data to parameterize charge separation, and as mentioned previously, newer data exist for low LWC regimes even at higher temperatures (Saunders and Peck 1998), which could result in solution variance near the melting level. In the absence of supercooled droplets, the ice supersaturation mechanism of Mitzeva et al. (2006b) may also influence charging in absence of supercooled droplets, as Willis and Heymsfield (1989) reasoned that ice fragmentation is active above the melting level, leading to the possibility of ice-ice collisional non-inductive charging.

Chapter 2

Model Description

2.1 Dynamical Model

The numerical model used for this study was the three-dimensional Collaborative Model for Multiscale Atmospheric Simulation (COMMAS; Wicker and Wilhelmson 1995). The model included prognostic equations for momentum, pressure, temperature (Klemp and Wilhelmson 1978), hydrometeor mass (Ziegler 1985; Mansell et al. 2010), and subgrid closure for turbulent kinetic energy (TKE; Deardorff 1980). The governing equations were as follows:

$$\begin{aligned} \frac{\partial u_i}{\partial t} &= -u_i \frac{\partial u_i}{\partial x_i} - C_p \bar{\theta} \frac{\partial \pi'}{\partial x_i} - \varepsilon_{ijk} f_j (u_k - \bar{u}_k) + \delta_{i3} B + D_{u_i} \\ B &= g \left[\frac{\theta'}{\bar{\theta}} + 0.61(q_v - \bar{q}_v) + q_{liq} + q_{ice} \right] \end{aligned} \tag{2.1}$$

$$\frac{\partial \pi'}{\partial t} + \frac{\bar{c}^2}{C_p \bar{\rho} \bar{\theta}_v} \frac{\partial (\bar{\rho} u_i)}{\partial x_i} = F_\pi \tag{2.2}$$

$$\frac{\partial \theta}{\partial t} = -u_i \frac{\partial \theta}{\partial x_i} + D_\theta + M_\theta, \tag{2.3}$$

$$\frac{\partial q_n}{\partial t} = -u_i \frac{\partial q_n}{\partial x_i} - \frac{1}{\bar{\rho}} \frac{\partial (\bar{\rho} V_i q_i)}{\partial z} + D_{q_n} + M_{q_n} \tag{2.4}$$

where u_i are the three components of the wind vector, π is the Exner pressure, θ is the potential temperature, and q_n are the mixing ratios for the hydrometeors. The air density is given by ρ, c is the sound speed, V_i are the particle fall speeds, and primed terms are perturbations from the base state. B is buoyancy term as defined and C_p is the specific heat of air at constant pressure. D and M were the turbulent mixing terms were the microphysical sources and sinks, respectively. The mixing terms for each equation were defined as:

$$D_{ui} = \frac{\partial}{\partial x_i}\left[K_m\left(\frac{\partial u_i}{\partial x_j} + \frac{\partial u_j}{\partial x_i}\right) + \frac{2}{3}\delta_{ij}E\right] \tag{2.5}$$

$$D_\theta = \frac{\partial}{\partial x_i}\left(K_m\frac{\partial \theta}{\partial x_i}\right) \tag{2.6}$$

$$D_{q_i} = \frac{\partial}{\partial x_i}\left(K_m\frac{\partial q_i}{\partial x_i}\right). \tag{2.7}$$

The prognostic equation for TKE (E) was solved for K_m using

$$\frac{dE^{\frac{1}{2}}}{dt} = \frac{C_m l}{2}S + \frac{C_m l Pr}{2}B_{tke} + \frac{\partial}{\partial x_i}\left[2K_m\frac{\partial E^{\frac{1}{2}}}{\partial x_i}\right] - \frac{C_e E}{2l}, \tag{2.8}$$

where

$$\begin{aligned}
K_m &= C_m l E^{\frac{1}{2}}, && (2.9)\\
S &= -K_m\left(\frac{\partial u_i}{\partial x_j} + \frac{\partial u_j}{\partial x_i}\right) + \frac{2}{3}\delta_{ij}E, && (2.10)\\
E &= \frac{1}{2}\overline{(u_i')^2}, && (2.11)\\
B_{tke} &= -A_{tke}K_h\frac{\partial \theta_e}{\partial z} + K_h\frac{\partial q_{liq}}{\partial z}, and && (2.12)\\
A_{tke} &= \frac{1 + \frac{1.61\epsilon_a L q_v}{R_d T}}{\bar{\theta}(1 + \frac{\epsilon L^2 q_v}{C_p R_d T^2})}. && (2.13)
\end{aligned}$$

Time integration of these equations was performed with a third-order Runge-Kutta (RK) method (Wicker and Skamarock 2002). The spatial derivatives for momentum and scalar advection were solved using a fifth-order, upwind finite difference scheme for the first two RK iterations, and a fifth-order weighted essentially non-oscillatory (WENO) scheme for the final RK iteration. The use of the WENO scheme served as a numerical filter, but was more computationally expensive than the fifth-order upwind scheme, thus was reserved for only the last step in the time integration. Pressure terms were calculated using an iterative small step solution to handle faster wave velocities. The buoyancy term in the vertical momentum equation was a simple 1st order finite difference. Coriolis terms were a straightforward calculation. Sedimentation was calculated using a 1st order upwind scheme.

2.1.1 Microphysical Parameterizations

The essential conclusions of this work depend on the microphysics parameterizations. The core of the parameterizations were based on the work of Ziegler (1985), and updated to two-moment for six hydrometeor categories (cloud droplets, rain, ice crystals, snow, graupel, and hail) as described in Mansell et al. (2010). In addition to the improvements of Mansell et al. (2010) such as variable density graupel and hail, a bulk liquid water fraction for partially frozen snow and graupel was calculated and advected with the respective particles (Ferrier 1994). The details of the new terms are described in Chapter 3.

2.2 Electrification Parameterizations

This study relied heavily on the electrical parameterizations of Ziegler et al. (1986), Ziegler et al. (1991), and Mansell et al. (2005). Mansell et al. (2005) included collisional inductive and non-inductive charge separation, sedimentation, small ion processes, and charge transfer between hydrometeor categories from microphysical conversions of species type.

2.2.1 Inductive Charging

Inductive charging was based on the method of Ziegler et al. (1991), using the rate equation

$$\frac{\partial \varrho}{\partial t} = \frac{\pi^3}{8} E_{gw} E_r N_w N_h \alpha D_{n,w}^2 \sqrt{\frac{6V_h}{\Gamma(4.5+\alpha_h)}} \left[\pi \Gamma(3.5) \varepsilon E_z \langle \cos\theta \rangle D_{n,h}^2 - \frac{\Gamma(1.5+\alpha_h)\varrho_h}{3N_h} \right] \tag{2.14}$$

for collisions between graupel pellets and supercooled cloud droplets. The equation describes the probability of a graupel particle colliding and rebounding with the cloud water droplets at an average cosine of the rebounding collision angle of $\langle \cos\theta \rangle$, yielding the change in graupel space charge, ϱ_h. Furthermore, $D_{n,c}$ is the cloud droplet diameter, E_{gw} is the collision efficiency, E_r is the rebound probability, N_w and N_h are the total cloud water and graupel number densities, $D_{n,h}$ is the characteristic diameter of graupel, E_z is the vertical component of the electric field, α is the fraction of droplets with grazing trajectories, and ε is the permittivity of air.

2.2.2 Non-inductive Charging

For collisional non-inductive charging, the charge separation rate between two hydrometeor species, x and y, is given as

$$\frac{\partial \varrho_{xy}}{\partial t} = \int_0^\infty \int_0^\infty \frac{\pi}{4} \delta q'_{xy} (1 - E_{xy}) |V_x - V_y| (D_x + D_y)^2 n_x(D_x) n_y(D_y) dD_x dD_y \tag{2.15}$$

Essentially, the equation describes the number of collisions for a volume swept out by the larger particle, and assigns a charge transfer per collision through the term $\delta q'_{xy}$. Assuming constant diameter dependency for the charge separation per event, this term can be pulled outside of the integral using the form

$$\delta q_{xy} = A D^a V^b q. \tag{2.16}$$

where A, a, and b are constants determined by empirical data and D is the constant diameter. An additional simplification was made to use an approximation for the mass-weighted fall speed differential, V. The rate equation then becomes a product of the collection efficiency, the charge separation approximation, and the number concentration rate tendency.

As described in Section 1.1.1.2, the polarity and amount of charge transferred can depend on several variables, like liquid water content, temperature or rime accretion rate. This study analyzed two of the charging schemes from (Mansell et al. 2005): one method, S91, followed the parameterization of Saunders et al. (1991), and the other used a methodology relating rime accretion rate (RAR) to charging, RR (Brooks et al. 1997). Beginning with S91, The first step was to determine the polarity of charge transferred to the target hydrometeor (generally graupel or hail). Figure 2.1 is a graphical depiction of the polarity zones for the S91 parameterization, where charge reversal temperature was described by:

$$S(T) = \begin{cases} 0.22, & T > -7.38 \\ -0.49 - 0.0664T, & -24 < T < -7.38 \\ 1.1, & T < -24 \end{cases} \tag{2.17}$$

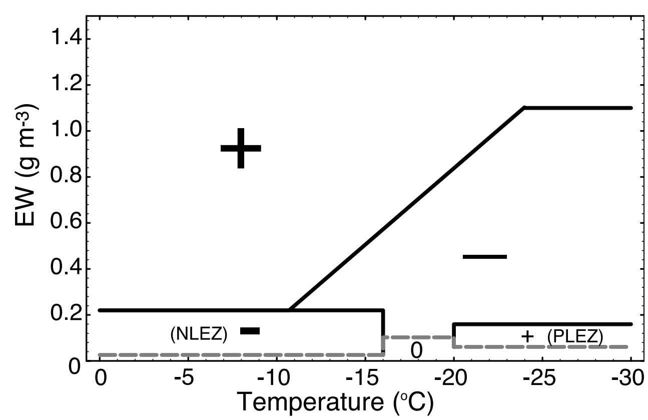

Figure 2.1: Diagram of charge polarity acquired by a target as a function of effective water content and temperature. Source: Mansell, et al., 2005.

Table 2.1: Empirical constants for a positively charging particle as a function of diameter.

Diameter	A	a	b
D < 155 μm	4.9×10^{13}	3.76	2.5
155 < D < 452 μm	4.9×10^{6}	1.9	2.5
D > 452 μm	52.8	0.44	2.5

Table 2.2: Empirical constants for a negatively charging particle as a function of diameter.

Diameter	A	a	b
D < 253 μm	5.24×10^{8}	2.54	2.8
D > 253 μm	24.0	0.5	2.8

For EW, the magnitude of charge separation was then given by

$$q_+ = \begin{cases} 20.22(EW - 0.22), & T > -7.38 \\ 20.22EW + 1.36T + 10.05, & T < -7.38 \end{cases} \tag{2.18}$$

$$q_- = 3.02 - 31.76EW + 26.53EW^2 \tag{2.19}$$

For low EW, empirical data is either lacking or gives little indication of a trend. This study tested two variations of charge separation for this region. The first replicated the S91 experiment of Mansell et al. (2005), with

$$q_{naz} = \begin{cases} -314.4EW + 7.92, & 0.026 < EW < 0.14 \\ 419.4EW - 92.64, & 0.14 \le EW < 0.22 \end{cases} \tag{2.20}$$

$$q_{naz} = q_{naz}|\frac{T}{7.38}| \tag{2.21}$$

for the anomalous zones.

The second method used in this study extrapolates the charge reversal temperature from $EW = 0.22$ at $T = -10.69$°C to $EW = 0$, and does not include any

Table 2.3: Empirical constants used to determine charge reversal temperature in the rime accretion rate scheme.

Constant	Value
C_1	7.9262×10^{-2}
C_2	4.4847×10^{-2}
C_3	7.4754×10^{-3}
C_4	5.4686×10^{-4}
C_4	1.6737×10^{-5}
C_5	1.7613×10^{-7}

anomalous zones. Therefore, equation 2.18 is used above the charge reversal temperature, and equation 2.19 below. The charge magnitude is linearly interpolated to 0°C from T=-7.38°C.

The other non-inductive charging method was based on Saunders and Peck (1998) for charging approximated by RAR. Here, the threshold for polarity change was demarcated by a critical RAR. The RAR was calculated as

$$RAR = EXWq_w\rho_0 V_h \tag{2.22}$$

and the critical RAR was determined to be

$$RAR_{crit} = \begin{cases} \min(3.29, -1.47 - 0.2T), & T > -15.0°\mathrm{C} \\ 0, & T < -32.47°\mathrm{C} \\ 1 + C_1T + C_2T^2 + C_3T^3 + C_4T^4 + C_5T^5 + C_6T^6, & \text{otherwise} \end{cases} \tag{2.23}$$

For RAR that was lower (higher) than the critical value for a given temperature a target hydrometeor was negatively (positively) charged, consistent with the method of Saunders et al. (1991). For the case tested here, RAR_{crit} was modified by a factor of $1 + \frac{T+25}{32.47-25}$ for the temperature range -25° to -32.47°C. The magnitude of

Table 2.4: Empirical constants for the rime accretion rate scheme as a function of diameter.

Target Diameter	A	a	b
$D < 155\ \mu m$	$4.9x10^{13}$	3.76	2.5
$155 \leq D \leq 452\ \mu m$	$4.0x10^{6}$	1.9	2.5
$D > 452\ \mu m$	52.8	0.44	2.5

charge separated per event used empirical results from Saunders and Peck (1998), with diameter dependence for the positive charge scenario.

2.2.3 Ion Processes

Ion processes are considered in order to maintain charge conservation. Ions were separated into two categories: small ions with a determinant mobility, μ (Chiu 1978; Helsdon 1980; Mansell et al. 2005), and large ions (e.g., aerosols) with limited or no mobility (Takahashi 1979, 1984). Ion sources began with a background fair weather field and were altered by parameterized cosmic ray generation, G, lightning flashes, S_{ltg}, evaporation of charged hydrometeors, S_{evap} (Takahashi 1979), drift, attachment to hydrometeors, S_{att}, corona discharge from the ground, S_{pd}, or recombination of ions with opposite polarity. The conservation equations associated with ions were

$$\frac{\partial n_{\pm}}{\partial t} = -\nabla\cdot(n_{\pm}\mathbf{V} \pm n_{\pm}\mu_{\pm}\mathbf{E} - K_m\nabla n_{\pm}) + G - \alpha n_{+}n_{-} - S_{\text{att}} + S_{\text{pd}} + S_{\text{evap}} + S_{\text{ltg}} \quad (2.24)$$

$$\frac{\partial n_{l\pm}}{\partial t} = -\nabla\cdot(n_{l\pm}\mathbf{V} \pm n_{l\pm}\mu_{\pm}\mathbf{E} - K_m\nabla n_{l\pm}) + G - \alpha n_{l+}n_{l-} - S_{\text{latt}} + S_{\text{lpd}} + S_{\text{levap}} + S_{\text{lltg}} \quad (2.25)$$

2.3 Lightning

Three dimensional lightning channels were parameterized using the stochastic dielectric breakdown model of Mansell et al. (2002). For grid points exceeding a given threshold of net electric field, a random point was selected for lightning initiation, with a preferential adjacent point completing the channel. The channel was extended step-by-step with positive and negative leaders. Propagation was determined on both ends of the channel randomly, from all possible points weighted by the net electric field. The electric potential was recalculated after each step using the internal electric field for the channel itself, and electric potential from Poisson's equation for all other points given by

$$\nabla^2 \phi = -\frac{\varrho}{\epsilon}. \tag{2.26}$$

Poisson's equation was solved using a multigrid "Black Box Multigrid" (BoxMG; Dendy 1982; Moulton et al. 1998) method after a given number of steps and red-black Gauss-Seidel iterative numerical methods otherwise. Channel propagation is continued until all channel points have electric field magnitudes below the minimum threshold, or until the channel reaches the ground (or some height threshold) as a CG flash.

The lightning grid was extended in all three dimensions from the dynamical model in order to reduce errors from boundaries near charge regions. The lightning domain was extended using an equivalent or higher resolution in the horizontal direction. In most cases, the lightning grid spacing was the same as the dynamic grid spacing.

Chapter 3

Experimental Setup

The experiments were separated into three main groups. The first set, the Parameterization Group, was a set of experiments designed to test sensitivity to new parameterization schemes. The experiments isolated each of the new parameterizations - both microphysical and dynamical - to analyze its effects on the solution. The conclusions of the experiment led to the development of a control test for the remaining two groups.

The second set, the Resolution Group, tested solution sensitivity to the spacing of the dynamics grid. As stated in Section 1.1.2, the evolution of a system can vary extensively with grid spacing. This set of tests analyzed three different resolutions for dynamical grids. As a self-contained experiment, the resolution dependence will be discussed in depth.

The third set, the Hypotheses Group, contained the hypotheses tests germane to the research. From the conclusions of the other two experimental groups, a control test was established and compared to cases developed using previous research. The main conclusions of this study arise from this group.

In the Parameterization and Hypotheses Groups, the experiments were compared to a control run. The text refers to the control run as "CONTROL" but the figures will reflect the simulation name, either PFRZ or CTRL500R, respectively. Additionally, Appendix A will explain the use of PFRZ for the Parameterization Group.

Table 3.1: Description of experiments in each group.

GROUP	EXPERIMENT	SUMMARY
PARAM	NOQXW	Does not include liquid water fraction on snow or graupel.
PARAM	NOQSMUL	Does not include ice multiplication by snow fracturing.
PARAM	CTRLS91OPT4	Electrification option without anomalous zones.
PARAM	CTRLOPT12	Electrification option using rime accretion rate dependence.
RESO	CTRL1KM	Horizontal grid spacing set to 1 km.
RESO	CTRL500	Horizontal grid spacing set to 500 m.
RESO	CTRL250	Horizontal grid spacing set to 250 m.
HYPO	DRAKE500	Allows for melting charging of snow and graupel.
HYPO	DONGHALLETT	Allows for snow depositional charging.
HYPO	CANOSALIST	Allows for inductive charging via raindrop disjection.
HYPO	MST06	Allows for charging in regions where no liquid water is present.
CONTROL/CTRL500R/PFRZ: The control experiment included liquid water fraction, ice fracturing, and 500 m resolution.		

3.1 Parameterization Group

Drake (1968) demonstrated that a particle undergoing melting and retaining some liquid could acquire a net charge, independent of collisions. Implementation of such an electrification mechanism necessitated an improvement to the melting process in the microphysical model by explicitly tracking the surface liquid.

The new scheme to predict the liquid water fraction was based on the work of Ferrier (1994) and was used for snow, graupel and hail (though hail was not used in this study). If any liquid water was present in a grid cell, it was assumed the entire distribution for that hydrometeor type had the same liquid water fraction and the number concentration was identical to the frozen hydrometeor category. A frozen particle could acquire a non-zero liquid water fraction through rapid collection of cloud water or rain (i.e., wet growth), collection of another partially wet hydrometeor type, or melting. In all simulations, the liquid water fraction was limited to 50% of the total mass.

Snow and graupel collection terms were treated as in Mansell et al. (2010) for two-component collection. The integral itself did not change, but collection efficiency was increased for wet distributions when collecting other ice particles. Wet graupel collection efficiency was unity for cloud ice collection, but limited to 0.5 for snow collection. Preliminary tests revealed unrealistic scavenging of snow by graupel when collection efficiency was set to 1.

Once the wet growth approximations were calculated, a heat balance equation was solved to determine how much of the accreted mass would freeze (T $<$ 0°), or if any melting was occurring (T $>$ 0°) (Ferrier 1994). The heat balance equations for rain, snow, and graupel, respectively, were given as

$$F_{qzr} = \min(\frac{q_r}{\Delta t}, max(0.0, \frac{M_1}{1 - M_2} N_r F_r)) \tag{3.1}$$

$$F_{qzs} = \max(0.0, \frac{M_1}{1 - M_2} N_s F_s + (W_2 - 1) QSACI) \tag{3.2}$$

$$F_{qzh} = \max(0.0, \frac{M_1}{1 - M_2} N_h D_{n,h} F_h + (W_2 - 1)(QHACI + QHACS)) \tag{3.3}$$

where the ventilation coefficients were

$$F_r = (1.6 + 124.9(10^{-3}\rho_0 q_r)^{0.2046}) \left(\frac{\Gamma(\alpha_r + \frac{4}{3})}{\Gamma(\alpha_r + 1)(\alpha_r + 1)^{\frac{1}{3}}} \right) \tag{3.4}$$

$$F_s = 0.65 + 0.44 Sc^{\frac{1}{3}} \nu_k^{-\frac{1}{2}} (V_s D_{n,s})^{\frac{1}{2}} \tag{3.5}$$

$$F_h = 0.78 \frac{\Gamma(2 + \alpha_h)}{\Gamma(1 + \alpha_h)} + 0.308 \frac{\Gamma(2.5 + \alpha_h + 0.5 b_h)}{\Gamma(1 + \alpha_h)} Sc^{\frac{1}{3}} D_{n,h}^{\frac{1}{2} + \frac{1}{2} b_h} \left(\frac{a_h}{\nu_k} \frac{\rho_h}{\rho_{0h}} \frac{\rho_{00}}{\rho_0} \right)^{\frac{1}{2}} \tag{3.6}$$

and the melting and wet growth constants, M_1, M_2, W_1, and W_2, were defined as

$$M_1 = 2\pi \frac{L_v}{L_f} \psi (q_{ss}(0) - q_v) - K_a \frac{T}{\rho_0} \tag{3.7}$$

$$M_2 = -C_w \frac{T}{L_f} \tag{3.8}$$

$$W_1 = 2\pi \frac{L_v \psi \rho_0 (q_{ss}(0) - q_v) - K_a T}{\rho_0 (L_f + C_w T)} \tag{3.9}$$

$$W_2 = \frac{1 - C_i T}{L_f + C_w T}. \tag{3.10}$$

The maximum freezing rate for snow and graupel was

$$F_{fms} = (1 - \Delta t \frac{QHCNS}{q_s}) F_{qzs} \tag{3.11}$$

$$F_{fmh} = \Delta t (F_{qzr} \frac{QSACR}{q_r} + F_{qzs} \frac{QHCNS}{q_s}) \tag{3.12}$$

whereas the maximum liquid mass available to be frozen was

$$F_{qls} = \frac{q_{sw}}{\Delta t} + QSACW + QSACR - F_{sw}(QHCNS + QHACS) \tag{3.13}$$

$$F_{qlh} = \frac{q_{hw}}{\Delta t} + QHACW + QHACR + F_{hw}(QHCNS + QHACS) \tag{3.14}$$

for mixing ratio of the liquid portion of snow and hail, q_{sw} and q_{hw}, respectively.

The physical process would be limited to the smaller rate, and thus the rate of freezing for temperatures below freezing became

$$QSFZS = \min(F_{fms}, F_{qls}) \tag{3.15}$$

$$QHFZH = \min(F_{fmh}, F_{qlh}). \tag{3.16}$$

Melting was handled in a similar fashion, first calculating the amount of liquid water collected available for melting, normalized by the bulk mass of frozen water available.

$$QSMLR = \min(0.0, M_1 N_s F_s D_{ns} + M_2(QSACR + QSACW))(1.0 - \frac{q_{sw}}{q_s}) \tag{3.17}$$

$$QHMLR = \min(0.0, M_1 N_h F_h D_{nh} + M_2(QHACR + QHACW))(1.0 - \frac{q_{hw}}{q_h}) \tag{3.18}$$

Although this rate determines the amount of frozen mass that melts, not all liquid mass is retained on the frozen hydrometeor (Rasmussen and Heymsfield 1987). To determine the amount of liquid shed, a preliminary sum, q^*, was calculated for known sources and sinks of each hydrometeor type. It was then assumed any liquid in excess of the maximum liquid water fraction, F_{xwm}, was shed from the distribution.

$$q_s^* = q_s + (\Delta Q_{s+} - \Delta Q_{s-}))\Delta t \tag{3.19}$$

$$q_{sw}^* = q_{sw} + (\Delta Q_{sw+} - \Delta Q_{sw-})\Delta t \tag{3.20}$$

$$QSSHR = -\left(q_{sw} - q_s^* - q_{sw}^\star \frac{F_{swm}}{1 - F_{swm}}\right) \tag{3.21}$$

$$q_h^* = q_h + (\Delta Q_{h+} - \Delta Q_{h-})\Delta t \tag{3.22}$$

$$q_{hw}^* = q_{hw} + (\Delta Q_{hw+} - \Delta Q_{hw-})\Delta t \tag{3.23}$$

$$QHSHR = -\left(q_{hw} - q_h^* - q_{hw}^\star \frac{F_{hwm}}{1 - F_{hwm}}\right) \tag{3.24}$$

It was assumed that the particles that completely melt and the water drops shed from the frozen hydrometeors were large enough to be considered rain. The change in number concentration for the frozen distribution does not change for wet growth, however, the rain distribution increased by

$$CSSHR = \frac{N_s}{q_s} QSSHR \tag{3.25}$$

$$CHSHR = \frac{N_h}{q_h} QHSHR. \tag{3.26}$$

For the more traditional electrification schemes involving collisions, the amount of charging depends on the number of collisions between ice particles. Preliminary simulations indicated an underestimation of ice crystal concentration in and near the melting layer, the region of interest for this study. A mechanical ice multiplication process proposed by Willis and Heymsfield (1989) was included to closer approximate observed ice crystal distributions (Passarelli 1978; Lo and Passarelli 1982). For snow with an equivalent diameter of 100μm to 2 mm, the rate of ice crystal production was given as

$$QSMUL = K_{frag}\left(q_s - \frac{\pi}{\rho_{air}}\rho_s N_s[5\times10^{-6}]^3\right) \tag{3.27}$$

$$CSMUL = \frac{\rho_0}{M_{frag}} QSMUL, \tag{3.28}$$

adapted from Schuur and Rutledge (2000b). The enhanced ice crystal concentrations were observed just above the 0°C isothermal layer, through about -7°C (Willis and Heymsfield 1989). For this study, ice fragmentation was limited to temperatures above -8°C.

After establishing the microphysical parameters to be used in the control test, a corresponding evaluation of the electrification schemes was performed. Three (collisional) non-inductive schemes were tested and compared to observation for verisimilitude. The schemes were presented in Section 2.2.2.

Additionally, a large ion category was added to the electrification model to ascertain whether ion mobility can influence charging near the stratiform melting layer. Although this mechanism could be tested within the Parameterization Group, it was found to be most applicable to the Hypotheses Group and is described therein.

3.2 Resolution Group

With increasing computational efficiency, simulation of larger systems with greater resolution becomes possible. Within this group, the effects of increasing horizontal resolution are analyzed for dynamical and electrical solutions. The spacings examined for the dynamical grid were 1 km, 500 m, and 250 m. The vertical resolution remained constant throughout the experiment at 250 m for the depth of the simulated storm.

3.3 Hypotheses Group

The main objective of this research was to test the validity of existing hypotheses regarding observed significant charge layers in the stratiform region. Because the two lowermost charge layers tend to coincide with the 0°C isothermal layer, the primary hypothesis involved the effect of charge separation resulting from a melting process (Drake 1968). A secondary hypothesis examined the influence of charging that occurs during depositional growth of snow, which is possible in the ice supersaturated region above the melting layer (Dong and Hallett 1992). Likewise, this research tested an alternative hypothesis for liquid-free charging, which may be relevant for the subsaturated region below the melting layer (Mitzeva et al. 2006b). Finally, the breadth of significant charge densities which reside in the convective line begged the question of influence by an inductive process. Thus, a collisional inductive process for liquid particles was tested (Canosa and List 1993).

3.3.1 Charge acquired by melting: Drake Mechanism

For snow and graupel distributions with a characteristic diameter between 1 and 8 mm, charge was generated on a liquid-coated particle at a rate of

$$SCHMLR = -QHMLR\frac{\rho_0}{\rho_r}q. \tag{3.29}$$

As a first approximation, q was set to 2.67 x 10^{-3} C m^{-3}, an upper limit of the experimental results from Drake (1968). It should be noted that the measurement is per unit volume of meltwater, not air. Additional experiments revealed the numerical solutions were not sensitive to the range of values found in the laboratory results.

It was assumed the particles carrying the opposite charge were smaller than cloud-scale, thus were distributed into ions. As in Takahashi (1984), the number of large ions (aerosols) were limited to 10^9. If the charge exceeded this value, the remaining charge was added to the small ion concentration.

3.3.2 Charge acquired by deposition

Snow was shown to acquire charge when undergoing depositional growth (Dong and Hallett 1992). The amount of charge gained depends on the temperature and surface area of the snow particle. Following Schuur and Rutledge (2000b), the charging rate is described by

$$F_q(T) = 0.0008T^3 - 0.0025T^2 - 0.4477T - 1.286 \tag{3.30}$$

$$SCSDEP = 2\times10^{-12}\pi N_s D_s^2 F_q(T) \tag{3.31}$$

where $F_q(T)$ is in C cm^{-2} s^{-1}, but converted to C m^{-2} s^{-1} to agree with model units. A plot of the charge transferred from small ions as a function of temperature is shown in Fig. 3.1. Note that at temperatures just below freezing, snow can acquire negative charge.

3.3.3 Charge acquired by raindrop disjection

No changes to the microphysics were necessary to include wet particle disjection since it is assumed there is no change in number concentration or mass transfer between species. The number of collisions was approximated using the assumptions for collision and rebound efficiency from Canosa and List (1993). Additionally, to

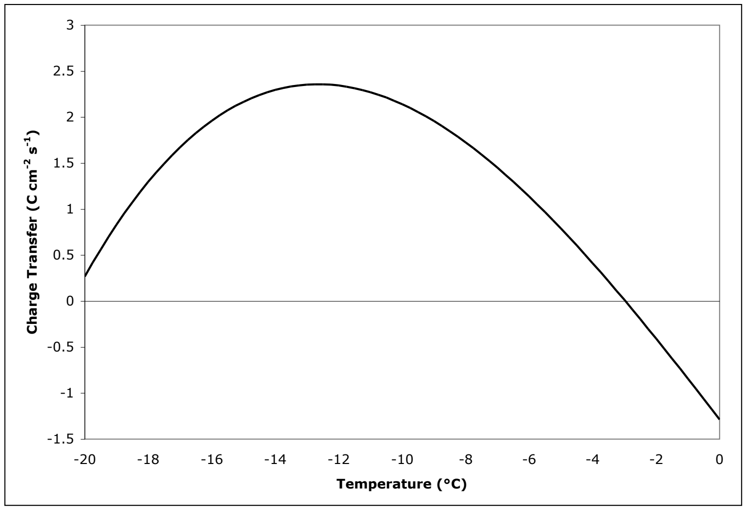

Figure 3.1: Charge transferred to snow undergoing depositional growth as a function of temperature, in C cm^{-2} s^{-1}.

obtain a non-zero fall speed differential, it was assumed the collisions were occurring between raindrops and wet snow, which is appropriate for the melting layer. Charge separation used the vertical component of the electric field in the Canosa and List (1993) formulation

$$SCSSHR = \frac{11\pi}{4}|V_r - V_s| E_{rs} E_r F_{dgt} N_r N_s D_r^2 cos\theta \frac{E_z}{E_{ref}} \tag{3.32}$$

where $E_{ref} = 50 \times 10^3$ to agree with results of Canosa and List (1993), F_{dgt} is an estimate of the fraction of droplets experiencing grazing trajectories (set to 1 for this experiment), and the above equation is multiplied by 10^{-12} to convert to model units.

3.3.4 Charge acquired by collisions in a liquid-free, ice supersaturated environment

The numerical study of Mitzeva et al. (2006a) demonstrated that liquid-free collisional charging is a possible source of observed charge in storm anvils of various types. An extension of this was to test the efficacy of this mechanism in the liquid-free subsaturated region near the melting layer of the stratiform region. The charge separation was only allowed for $T < 273$K and only when supersaturated with respect to ice. For non-inductive charging in the absence of cloud water, this parameterization is simplified by holding q constant (Mitzeva et al. 2006b). The charge polarity was determined by ice supersaturation. Negative charge was assigned to a target in an environment supersaturated with respect to ice. The charge transfer per event was set to $q = 0.1$ fC based on the results of Mitzeva et al. (2006b) and preliminary testing. The empirical constants from Table 2.1 and Table 2.2 were used for diameter and fall speed weighting.

Chapter 4

Simulation Results

The experiments were performed using a "channel" domain, capitalizing on the symmetry of squall-line systems in the absence of Coriolis forcing. This required periodic boundary conditions for the north and south sides of the domain, for a west-east moving system. Preliminary examination indicated no major differences when reducing the width of the channel to 40 km. As such, for performance enhancement, some channel experiments were run with a 40 km-wide domain and others at 80 km, noted by the plot scales. All simulations had a vertical resolution of 250 m for the lowest 10 km of the domain. Above that, the vertical grid spacing was stretched to a maximum of 700 m. Horizontal resolution was 500 m, with the exception of those examined in the Resolution Group.

The simulations were initialized with three thermal bubbles in a stably stratified environment (Weisman and Klemp 1982). The temperature profile of each thermal was a cosine squared function from the maximum temperature perturbation at the center of the thermal, 2.0°C in these cases. The disc-like thermals had a 10 km horizontal radius and a 1.4 km vertical radius. The initial wind profile was unidirectional, with 10 s^{-1} speed shear in the lowest 2.5 km of the domain, remaining constant above that level (Skamarock et al. 1994). Surface water vapor mixing ratio was initialized at 12.5 g kg^{-1}.

In the following sections, the control experiment (CONTROL) used the methodology described by Appendix B, but includes the liquid water fraction prediction described in Section 3.1. Allowing a particle to melt and maintain meltwater was essential to many of the hypotheses, and thus included in the control experiment for comparison. A description of the CONTROL results can be found in the next section.

4.1 Parameterization Group

This section examines the effects of modifying two microphysical parameterizations: turning off liquid water fraction (NOQXW) and turning off ice multiplication via snow fracturing (NOQSMUL). A more thorough description and discussion of the CONTROL experiment is provided with the liquid water fraction experiment, as those effects impacted all ensuing experiments.

In the CONTROL experiment, convection initiated quickly given the +2.0°C temperature perturbation and high surface vapor content. The system began as initially isolated cells with maximum updraft velocity of typically 20-25 m s^{-1}, and a simulation maximum of 39 m s^{-1}. After approximately 1 hour, cold pools formed at the surface from the descending precipitation of the original cells, and new cells developed between the initial three thermals. These cells cycled in a similar manner, until a line of cells had formed by approximately 2 hours. By 3 hours, convection was sustained by a continuous supply of high-θ_e air ahead of the cold pool outflow, which began to surge ahead of the storm (Fig. 4.1). Diagnostic radar reflectivity demonstrated the upright characteristic for updrafts in long-lived squall lines suggested by Rotunno et al. (1988). The longevity of the system also suggested the choice of buoyancy forcing and shear profile were appropriate to simulate a typical leading-line, trailing stratiform squall line (i.e., symmetric MCS) (Thorpe et al. 1982; Weisman and Klemp 1982).

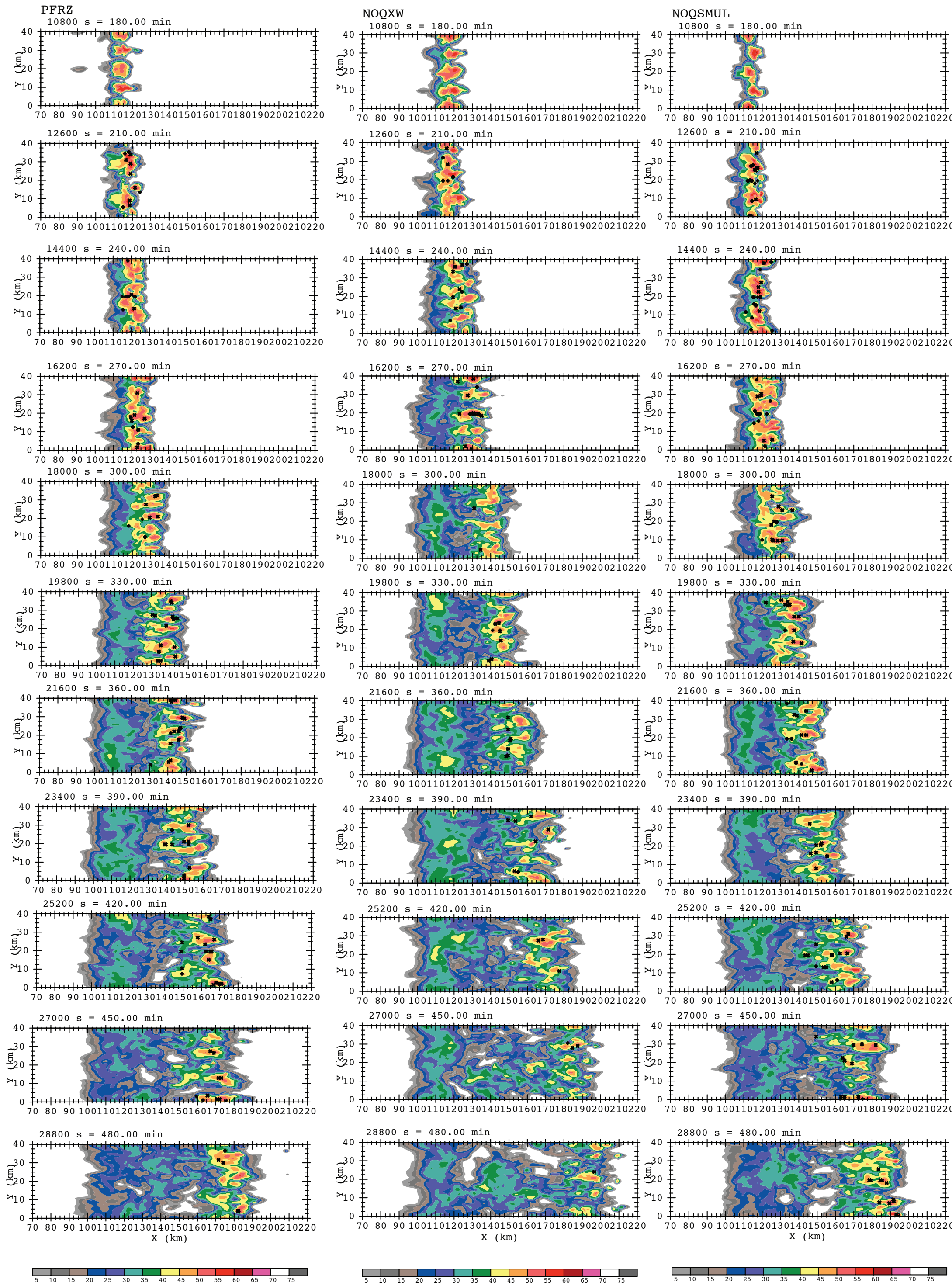

Figure 4.1: Surface reflectivity and CG locations (x negative; + positive) for CONTROL, NOQXW, and NOQSMUL.

Beyond 5 hours, the system developed a trailing stratiform rain region. Surface reflectivity maximums in the stratiform region were approximately 35-40 dBZ, compared to > 60 dBZ in the convective line. Including a liquid water fraction on graupel and snow eliminated the need to recombine rain and snow to diagnose a mixed-phase region to infer reflectivity, yet yielded a more conspicuous bright band than previous studies (Rutledge and Houze 1987; Fovell and Ogura 1988; Skamarock et al. 1994). In the CONTROL experiment, the bright band was evident by 6 hours, with reflectivity of 40-50 dBZ spanning over 10 km near the melting level. By 8 hours − the termination of the simulation − the stratiform region (defined by > 35 dBZ) spanned over 40 km. The low-reflectivity, precipitation-free transition zone increased in span from about 15 km at 5 hours to approximately 20 km by the end of the simulation.

Comparing simulated thermodynamic results to observation, Figure 4.2 is a simulated, representative sounding plot through an area of the stratiform region that contained supercooled liquid water (Fig. 4.3). The presence of supercooled liquid cloud water suggests that localized charging by traditional non-inductive methods would be possible. Additionally, the sounding shows a deep saturated layer above the 0°C isothermal layer that is present in observed soundings (e.g., Fig. 1.4).

4.1.1 The effect of adding a liquid water fraction to snow and graupel

The system without a liquid water fraction (NOQXW) had a much faster evolution than the CONTROL experiment (Fig. 4.1). By 5 hours of simulation time, the transition zone between the stratiform region and the convective line in the CONTROL experiment was just developing. In contrast, at the same simulation time, the NOQXW experiment had a well-defined stratiform region marked by surface reflectivity as high as 41 dBZ. Additionally, the translation speed of the convective cores was approximately equivalent to the domain translation speed (11 m s^{-1}) through 4

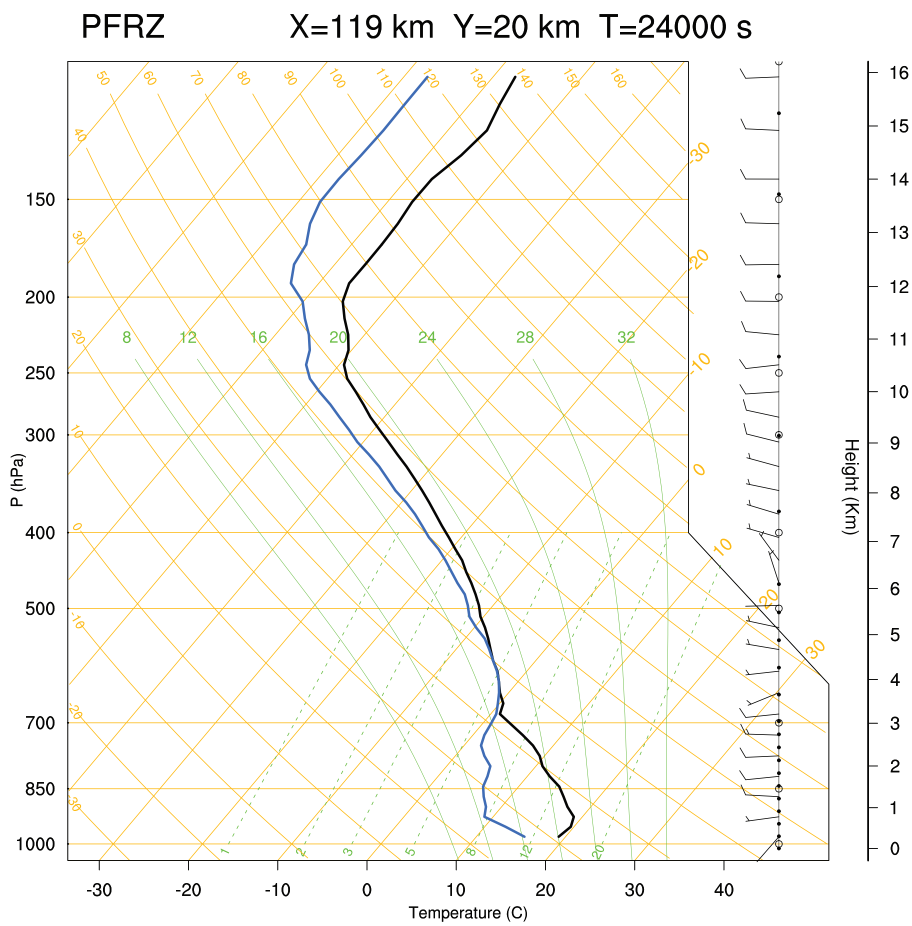

Figure 4.2: Skew-T diagram for PFRZ at 6 hrs 40 min for x = 119 km, y = 20 km. Vertical temperature profile in black, dew point in blue.

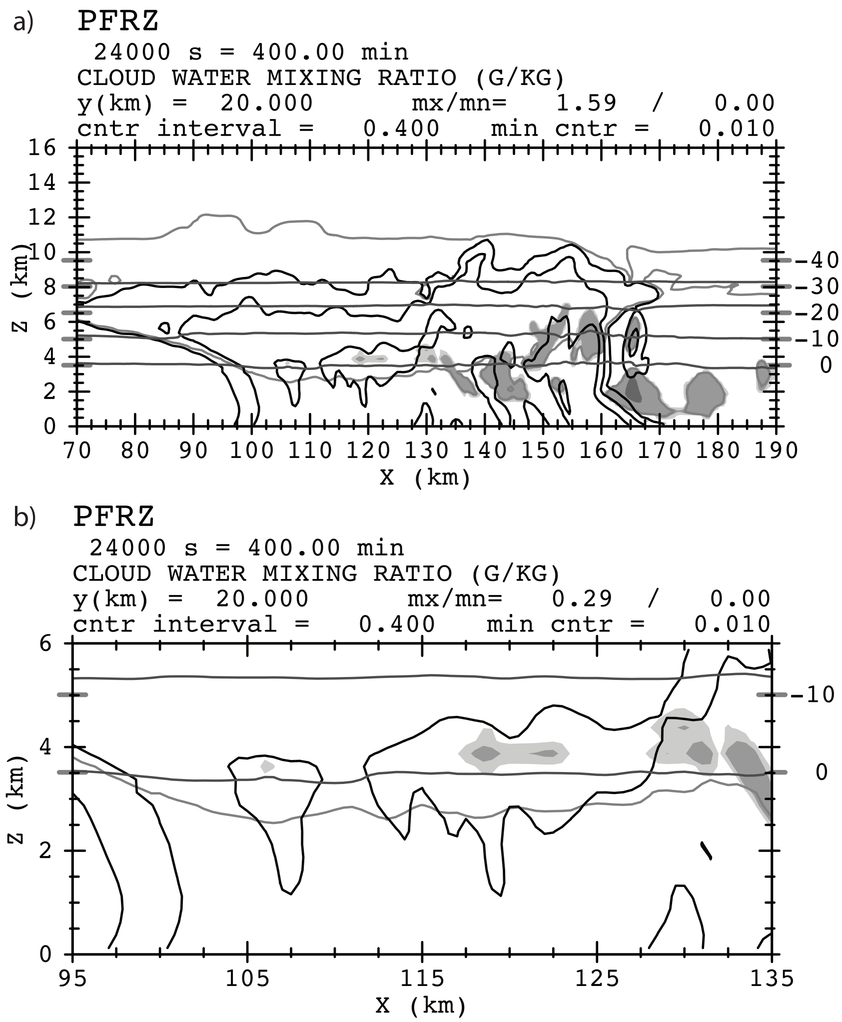

Figure 4.3: a) Vertical cross section through the line-perpendicular center of the domain at 6 hrs 40 mins for liquid cloud water content exceeding 0.01, 0.1, and 1.0 g kg^{-1} (light grey, grey, and dark grey) with reflectivity by 5 dBZ, temperature in °C, and cloud outline. b) A closer look at the same variables for x spanning 95 to 135 km and z spanning 0 to 6 km.

hours for CONTROL, but accelerated around 3.5 hours in NOQXW. In both cases, the back edge of the stratiform rain moved at a nearly constant velocity, but the width of the rainband increased as the convective line accelerated upstream.

Vertical cross-sections revealed slightly shallower convection in the NOQXW case than CONTROL. Storm tops exceeded approximately 12 km, with overshooting tops reaching approximately 14 km in the CONTROL experiment, compared to 10 km and 12 km in NOQXW, respectively. Both experiments showed enhanced (diagnosed) reflectivity near the melting level in the stratiform region, though with slightly different characteristics and explanations. The enhanced reflectivity in CONTROL was mainly the result of wet snow, as expected. This led to a shallow layer, approximately 1-1.5 km deep, of increased reflectivity that persisted once formed, and straddled the 0°C isotherm.

Without a predicted liquid coating, the increase in reflectivity near the melting level of NOQXW came primarily from large snow aggregates and rain before evaporation reduced the backscattering diameter. Figure 4.4 shows the relatively equivalent values of snow mass between CONTROL and NOQXW just above the 0°C level, yet the 1 L^{-1} contour does not descend into the high reflectivity area for NOQXW (Fig. 4.5). This assessment was further corroborated by the equivalent median volume diameter, which highlights the disparity in aggregate size between the two cases (Figs. 4.6 and 4.7). The bright band in NOQXW was marked by these pockets of high reflectivity, with wider bands of reflectivity exceeding 35 dBZ below the regions of large aggregates.

4.1.2 The effect of adding a liquid water fraction on storm electrification

The most apparent trend in electrical parameters was the significant reduction in IC flashes without including the liquid water fraction (Fig 4.8). Intracloud flashes were

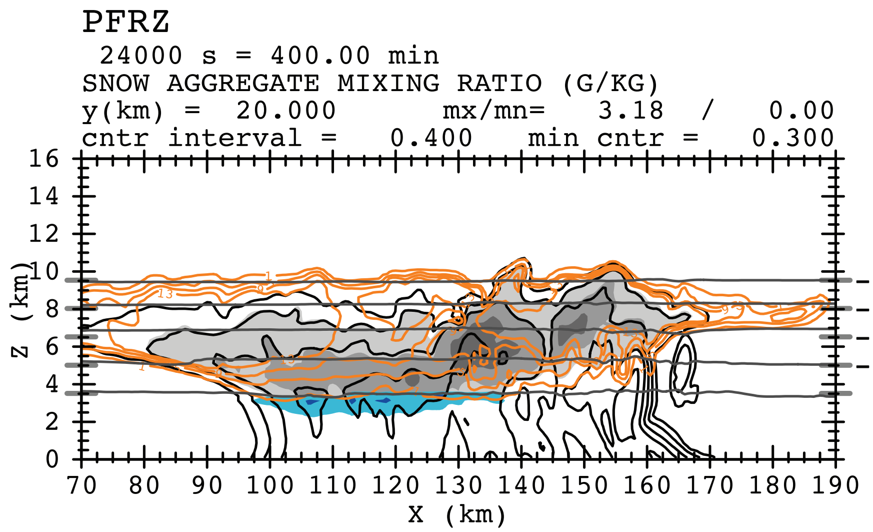

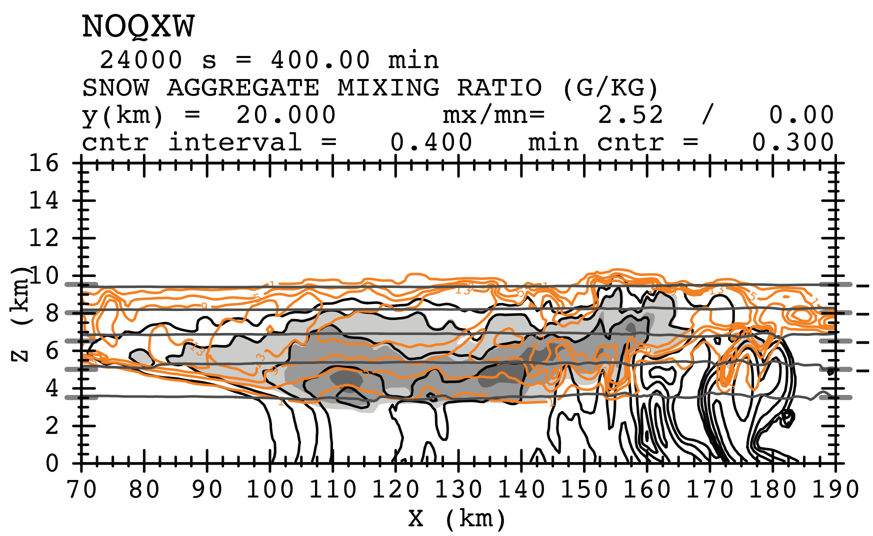

Figure 4.4: Shaded grey contours are mixing ratio (0.3, 1.0, 2.0 g kg^{-1}), shaded blue contours are liquid water fraction (0.2, 1.0 g kg^{-1}), reflectivity is black contours (10 dBZ intervals starting at 5 dBZ), orange contours are snow concentration (1-13 L^{-1} by 4 L^{-1})

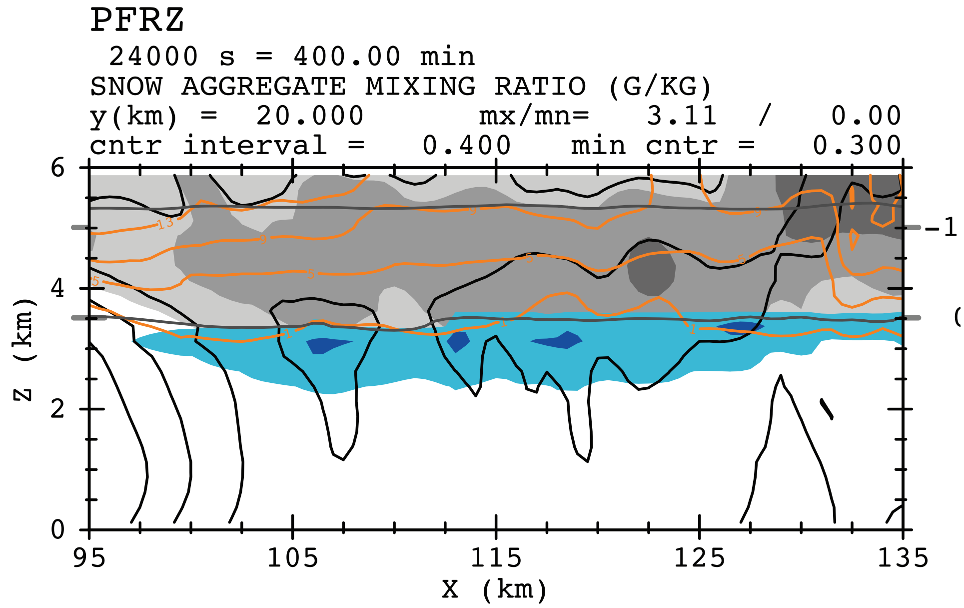

Figure 4.5: A closer look at snow mixing ratio and liquid water fraction for PFRZ. Contours as in Fig. 4.4

often 40-90% less frequent in NOQXW than CONTROL, only a few times exceeding 20 per min after 3.5 hours of simulation time (giving 30 minutes of electrical "spin up"). The IC flash rate was complemented by a reduction in CG flashes for NOQXW, particularly for the period from 5.5-6.5 hours. In absolute terms, CG flash rates were fairly similar, on the order of 1 to 2 per min. Additionally, -CG flashes dominated both simulations, with only 10 +CG in the last 3 hours of NOQXW, and 28 in CONTROL.

The overall charge structure was similar between the two cases when examining comparable periods of evolution (Figs. 4.9 and 4.10). The normal tripole signature was apparent in both experiments. Snow and graupel carry the most charge, but the smaller amount of graupel in NOQXW led to weaker net charge and fewer flashes overall (Figs. 4.11 and 4.12). One caveat is that these are unaveraged plots, thus lightning can change charge density locally when only looking at one time step.

Beyond the sloping main charge centers, neither case had significant upper-level charge in the transition zone or stratiform region. This suggests that charge advection

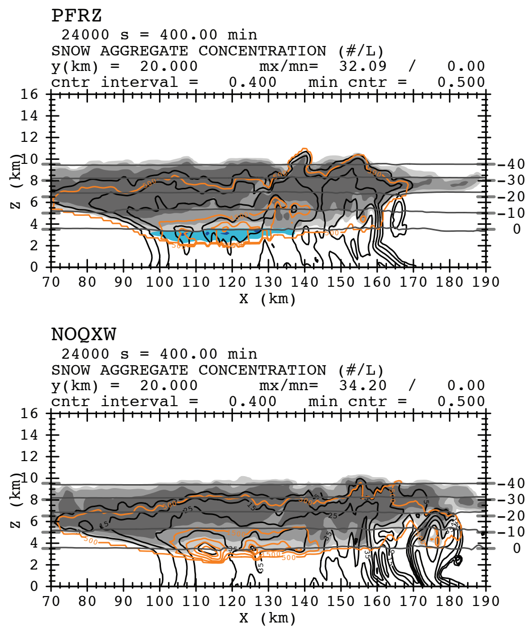

Figure 4.6: Reflectivity in black over the range 5-75 by 10 dBZ. Left panels: snow concentration shaded grey for 0.5, 3, 10 L^{-1}, liquid on snow mixing ratio is shown by blue-filled contours of 0.2 (light), 1.0 (dark) g kg^{-1}, and snow median volume diameter in orange over the range 500-5000 by 1000 microns. Right panels: rain concentration shaded grey for 5, 50, 100 L^{-1} and rain median volume diameter in orange over the range 100-2000 by 300 microns

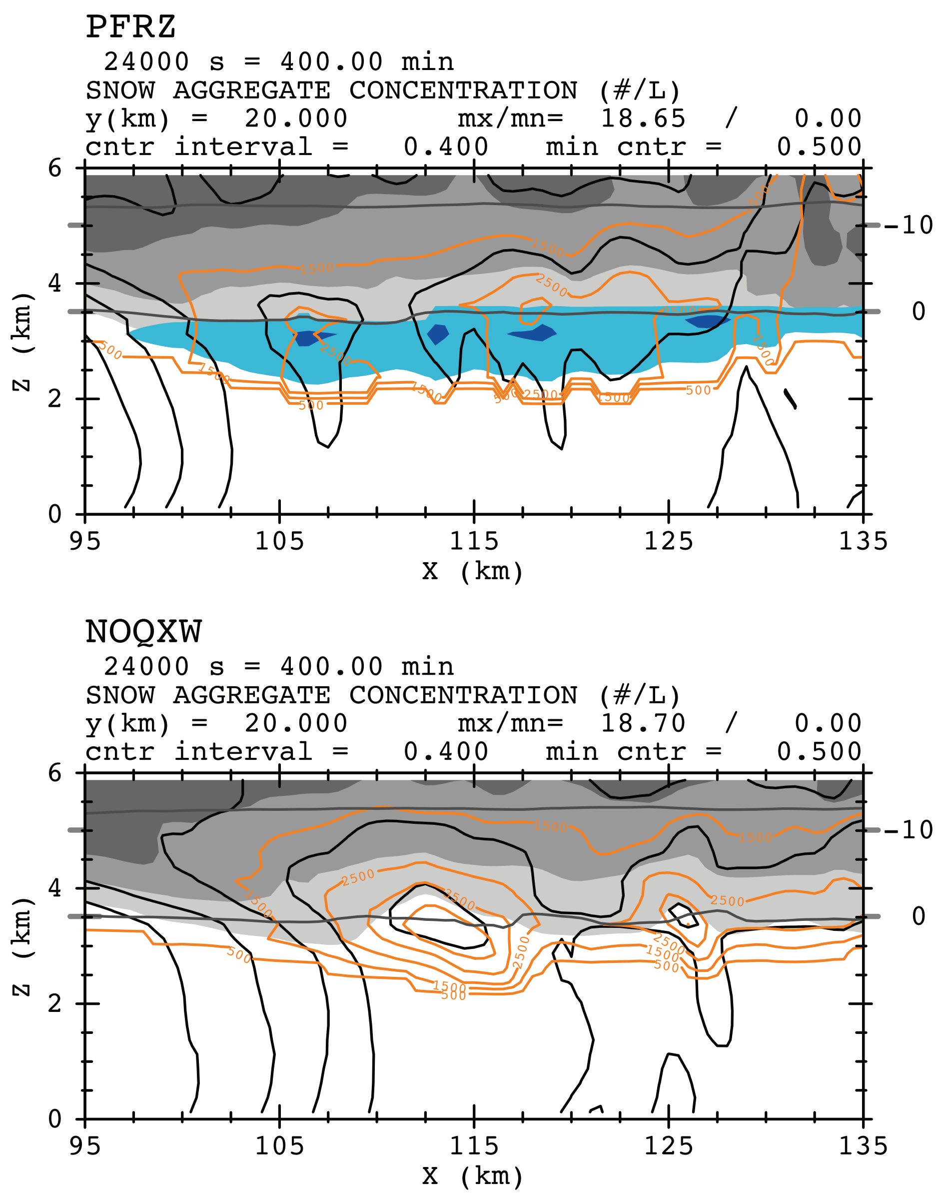

Figure 4.7: As in Fig. 4.6, for the region near the melting layer of the stratiform precipitation.

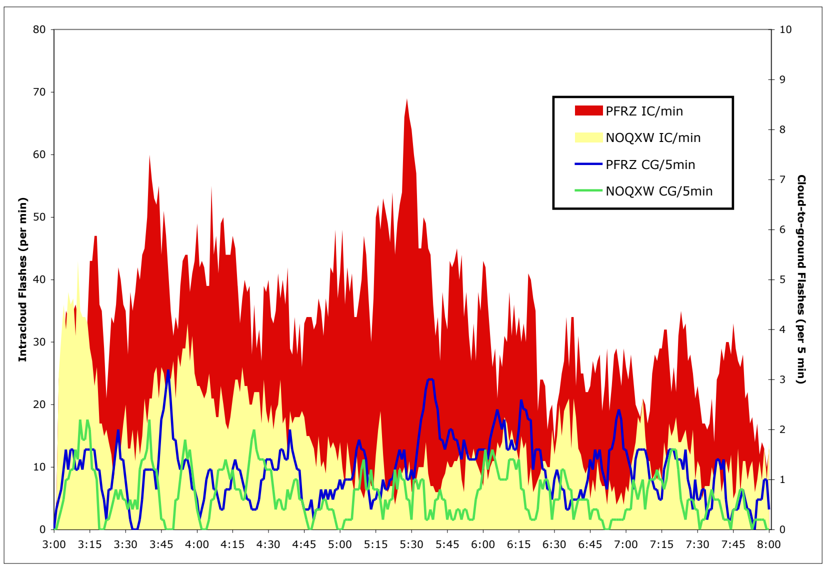

Figure 4.8: Intracloud flashes per minute for PFRZ (red) and NOQXW (yellow) on left axis, cloud-to-ground flashes per 5 minutes for PFRZ (blue) and NOQXW (green) on right axis.

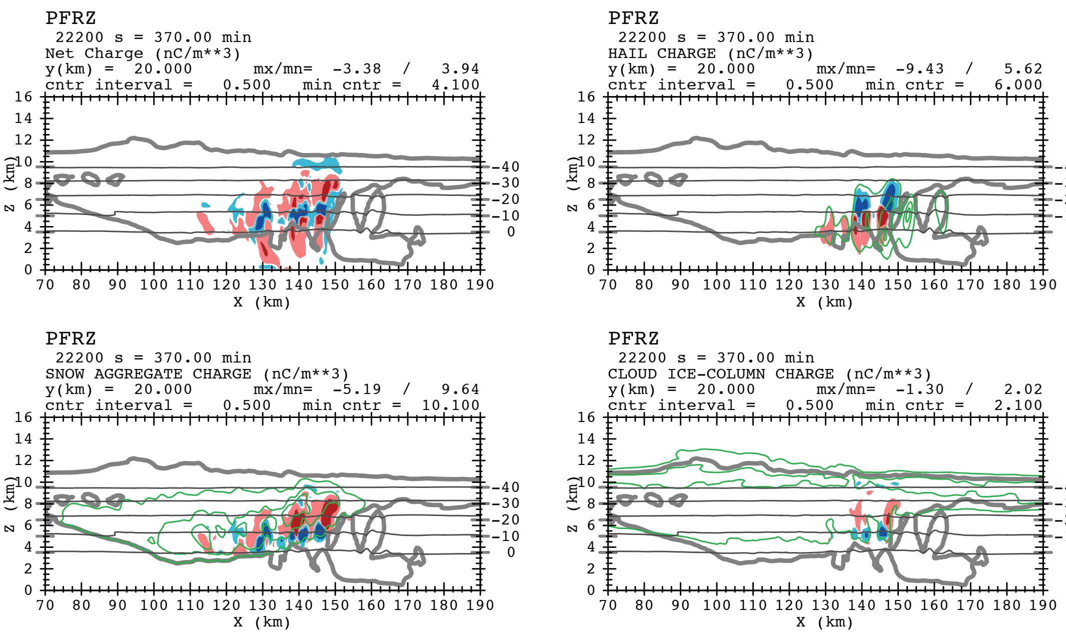

Figure 4.9: Charge density in nC m^{-3} for PFRZ case (solid contours) for values > 0.5 light red, > 2.0 dark red, < 0.5 light blue, and < 2.0 dark blue. Graupel and snow mass over the range 0.1 to 6.1 g kg^{-1} by 1 g kg^{-1} and ice mass from 1 to 11 g kg^{-1} by 5 g kg^{-1}.

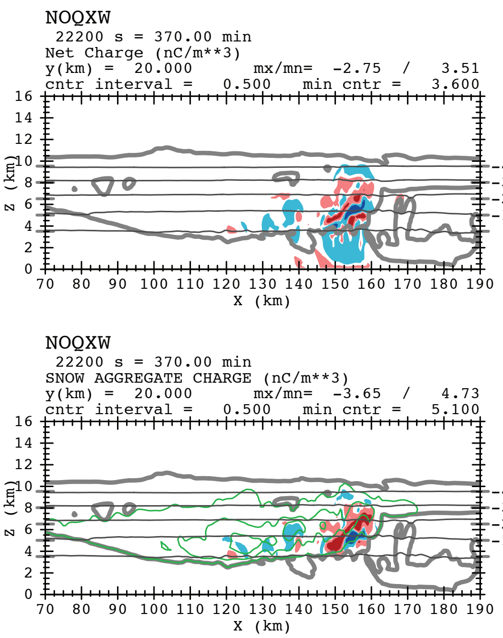

Figure 4.10: Charge density in nC m^{-3} for NOQXW case (solid contours) for values > 0.5 light red, > 2.0 dark red, < 0.5 light blue, and < 2.0 dark blue. Graupel and snow mass over the range 0.1 to 6.1 g kg^{-1} by 1 g kg^{-1} and ice mass from 1 to 11 g kg^{-1} by 5 g kg^{-1}.

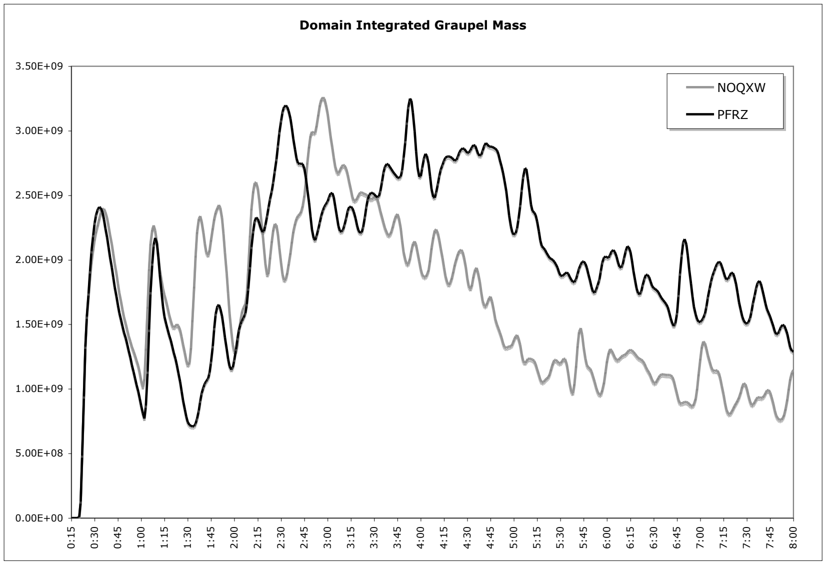

Figure 4.11: Domain integrated graupel mass (kg).

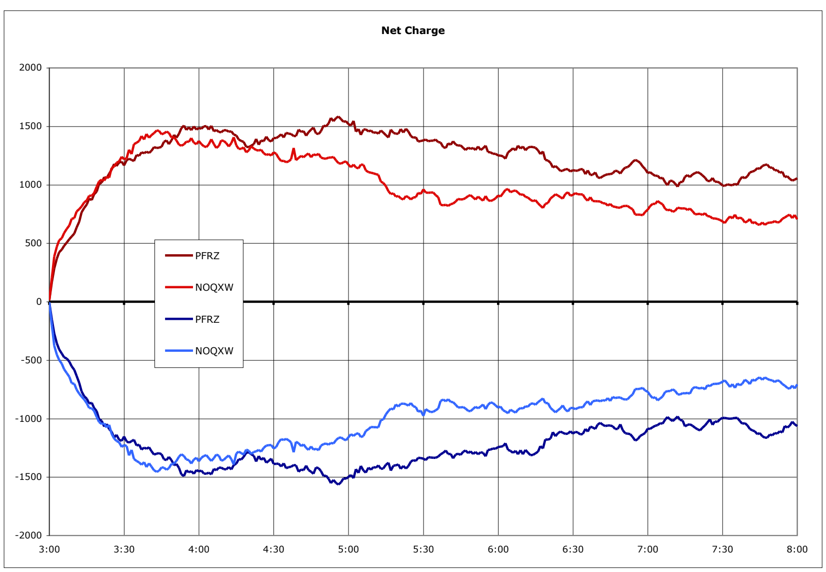

Figure 4.12: Domain integrated net positive and negative charge density for CONTROL (dark red/blue) and NOQXW (light red/blue) in C.

may be satisfactory for the main charge regions, but does not account for observed charge in the upper levels of the stratiform region.

4.1.3 Influence of the ice fracturing process

With the current parameterizations, the effect of including an ice fracturing process (Willis and Heymsfield 1989; Schuur and Rutledge 2000b) was minimal to the overall evolution of the system (Fig. 4.13). The initial convection formed a nearly continuous line by approximately 3 hours, and both experiments formed a stratiform region by approximately 5 hours. Translations speeds were in parity with the leading edge of convection in both cases extending to 172 km, spanning about 30 km rearward to the transition zone. The transition zone was about 10-15 km wide at the surface, and the trailing stratiform region was further downwind with similar values of reflectivity.

Without greatly affecting the evolution, the fracturing process significantly increased the ice crystal concentration just above the melting level (Fig. 4.14). The effects are clearest in the stratiform region near the -8°C isotherm, where the fracturing process is thought to be active. Total ice concentration was approximately 3-4 L^{-1} in this region for NOQSMUL. Those values are compared to over 8 L^{-1} in CONTROL, shown by the nearly continuous area surrounding the -8°C level for the CONTROL case. Observed values are closer to 100 L^{-1} (Willis and Heymsfield 1989), and reach a maximum between -3 and -1°C, so the current parameterization was an improvement but still unsatisfactorily representing total ice concentration above the isothermal layer.

The net charge on ice particles was also plotted in Fig. 4.14. The charge structure of the convective region did not change significantly as a result of the variation in ice concentration. Domain-width averages demonstrate a main positive charge region exists above a main negative region, with lower positive charge present. Single-slice

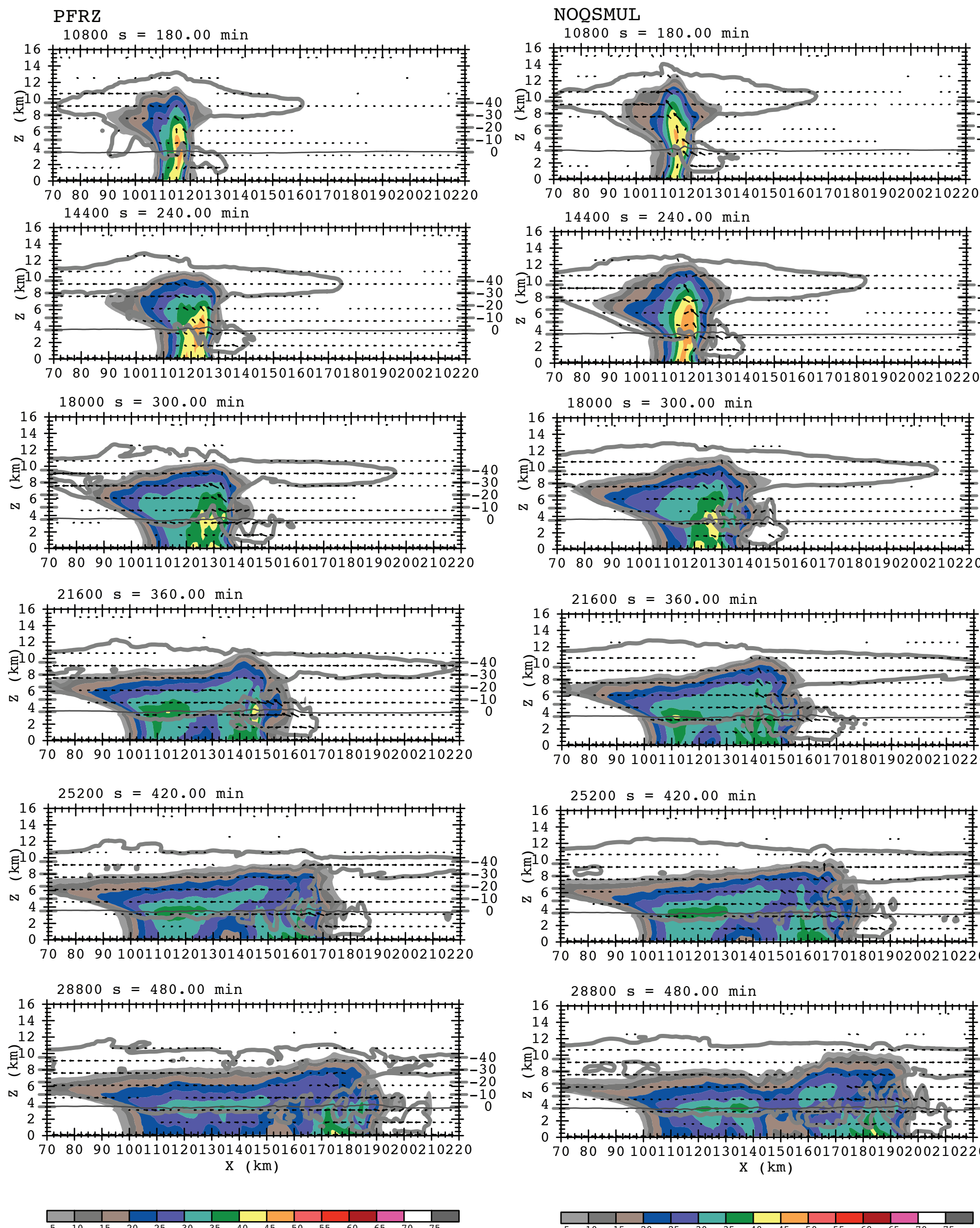

Figure 4.13: Vertical cross section displaying along-line averaged reflectivity and center-line windspeeds. Cloud outline shown, as well as 0°C isotherm.

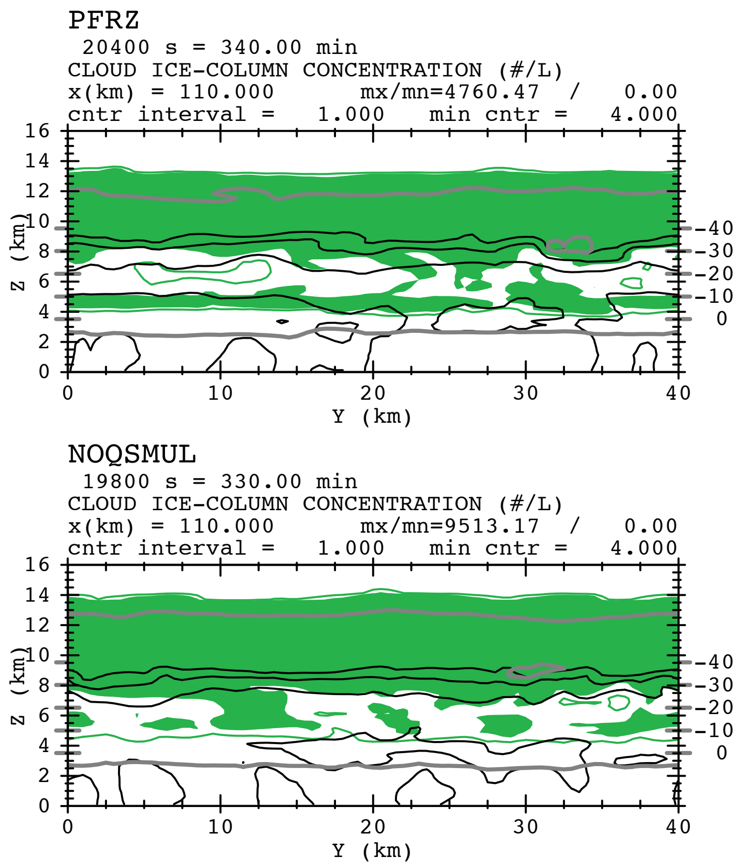

Figure 4.14: Cloud ice concentration in green for 4 (line) and 8 (solid) per L for y-z vertical cross section through the stratiform region at x = 110 km. Cloud outline shown in grey, with radar reflectivity as black contours over the range 5-75 by 10 dBZ. Times chosen for evolution similarity.

plots show more variation in charge structure (as in Fig 4.14), but do not impact the conclusions of the main hypotheses. Additionally, a test was run to increase the fragmentation rate by an order of magnitude. The conclusion was that although ice concentration in the stratiform region was increased substantially, no significant net charge was present and thus had no bearing on the main hypotheses. The choice was made to remain at the conservative value of fragmentation rate, consistent with previous literature. Sensitivity of this parameter could be reexamined in future research.

4.1.4 Non-inductive charging parameterization

Although the main hypotheses are primarily focused on charging in the stratiform region, where weak vertical velocities and a scarcity of graupel imply a charging mechanism other than traditional non-inductive charging, care must be taken to reproduce charge structure in the convective line as well. Three non-inductive charging schemes were tested to ascertain their applicability to an organized MCS system, as opposed to shorter-duration convection. Two tests were based on temperature and liquid water content dependency (CONTROL and CTRLS91OPT4), the other was based on rime accretion rate (CTRLOPT12). In all experiments, for computational efficacy, the simulation was run for 3 hours before activating non-inductive charging.

The CONTROL experiment demonstrated the typical semblance of a normal tripole in the convective line (Fig. 4.15): a main positive charge center above a main negative charge center, with a weaker region of lower positive charge below the main negative area. Charge densities were on the order of ± 1 nC m^{-3}, with local maxima reaching ± 2-4 nC m^{-3}. Occasionally the lower positive charge would dominate the other two charge centers, but generally as a local feature. Additionally, upper charge layer(s) were present for much of the simulation.

Downstream of the convective line, the main charge regions extended into the transition zone and exhibited a downward slope apparent in observations (Stolzenburg

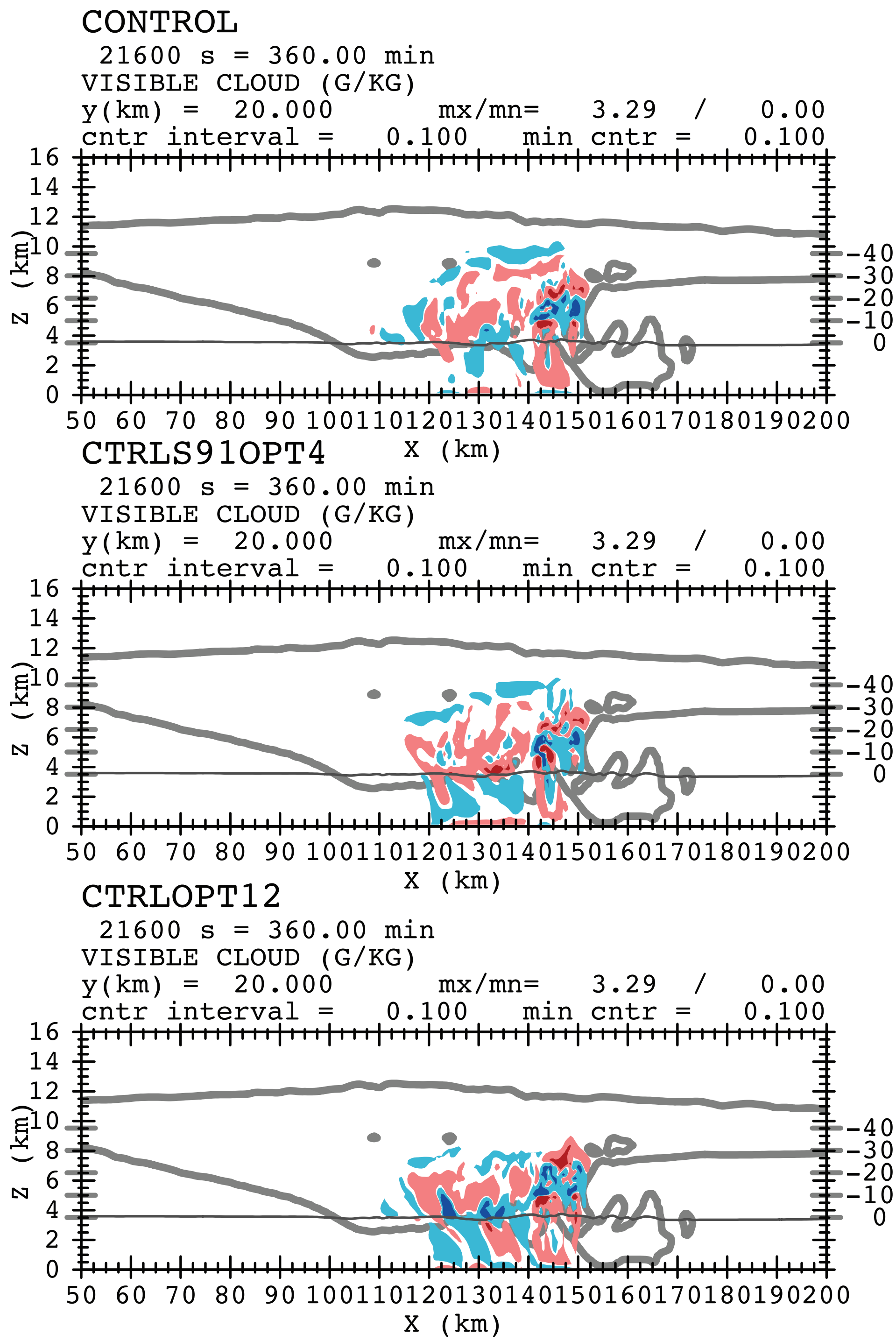

Figure 4.15: Vertical cross sections of net charge (nC m^{-3}) at 21600s through the center of CONTROL, CTRLS91OPT4, and CTRLOPT12. Charge density (solid contours) in nC m^{-3} for values $>$ 0.1 light red, $>$ 1.0 dark red, $<$ 0.1 light blue, and $<$ 1.0 dark blue.

et al. 1994, 1998, 2001; Dotzek et al. 2005; Ely et al. 2008). There was no appreciable net charge in the stratiform region of the system for the duration of the simulation.

The CONTROL system exhibited two periods of lightning patterns (Fig. 4.16a). While the system was developing and composed primarily of strong convection (i.e., before the system developed a stratiform rain region), +CG flashes outnumbered −CG flashes 2:1. Once the system matured and the stratiform rain region developed rearward, the −CG flash rate increased slightly to approximately 1 per min. To the contrary, +CG flashes were very infrequent, with only 13 flashes during the last 2 hours of the simulation.

The electrical features of the CONTROL case were remarkably different from the CTRLS91OPT4 case, despite the only variance being in the anomalous zones. For example, there was a lack of lower positive charge in the convective area and transition zone for CTRLS91OPT4. The main charge regions were stronger in CTRLS91OPT4 than the CONTROL case, with larger regions of 1-2 nC m^{-3}, and maximums often reaching 3-5 nC m^{-3}. As a result, the CG flashes mainly lowered negative charge to ground with intermittent +CG flashes. Near the end of the simulation, total CG flash rates were minimal, at about 0.25 per min. The scheme was also able to reproduce upper charge layers as in the CONTROL case (Fig. 4.15).

The results of the RAR-based scheme (CTRLOPT12) were similar to the CONTROL experiment. The convective line had the common tripole signature, with main positive over negative charge regions and a lower positive charge. The charge regions sloped through the transition zone and terminated near the stratiform precipitation. The main charge regions were stronger in CTRLOPT12 than the control case, with larger regions of 1-2 nC m^{-3}, and maximums typically reaching 3-5 nC m^{-3}.

CG flashes steadily increased in number during the convective phase of the MCS for CTRLOPT12 (Fig. 4.16c). During this phase +CG flashes were infrequent, approximately 1 per 10 minutes. After the MCS reached its mature phase around 5

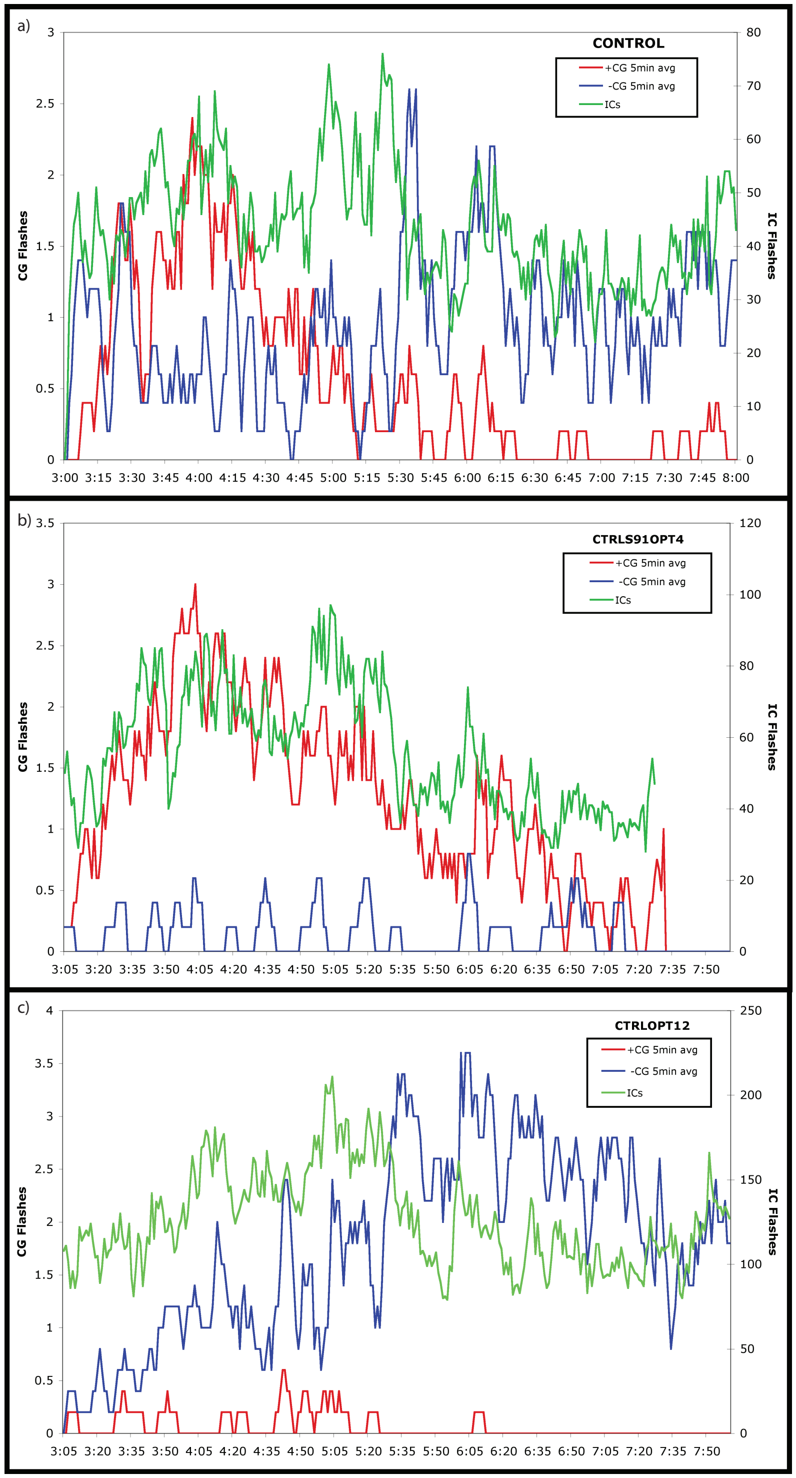

Figure 4.16: Intracloud flashes (green, right ordinate), +CG (red, left ordinate), −CG (blue, left) for a) CONTROL, b) CTRLS91OPT4, CTRLOPT12. CG flashes are smoothed by a 5-min running average.

hours, there were no +CG flashes and −CG flashes were steady around 2.5 per minute. The IC flash rate was notably higher than the other two cases. The CONTROL and CTRLS91OPT4 cases had maximum IC flash rates of 80-90 flashes per min, and averaged about 35-40 flashes per min during the mature, steady-state phase. The CTRLOPT12 case exceeded 200 flashes per min, and averaged just over 100 flashes per min when in steady state.

4.2 Resolution Group

Having established the microphysical and electrical parameters to be used in the study, an important facet to explore was the effect of grid spacing on the solutions. Three different horizontal grid spacings were tested: 1 km (CTRL1KM), 500 m (CTRL500), and 250 m (CTRL250). Vertical grid spacing was held constant at 250 m for each of the runs through a depth of 10 km, the approximate depth of the storm, and stretched above that level. The channel width in these cases was increased to 80 km to prevent noise or aliasing that might occur, particularly for the coarse resolution test.

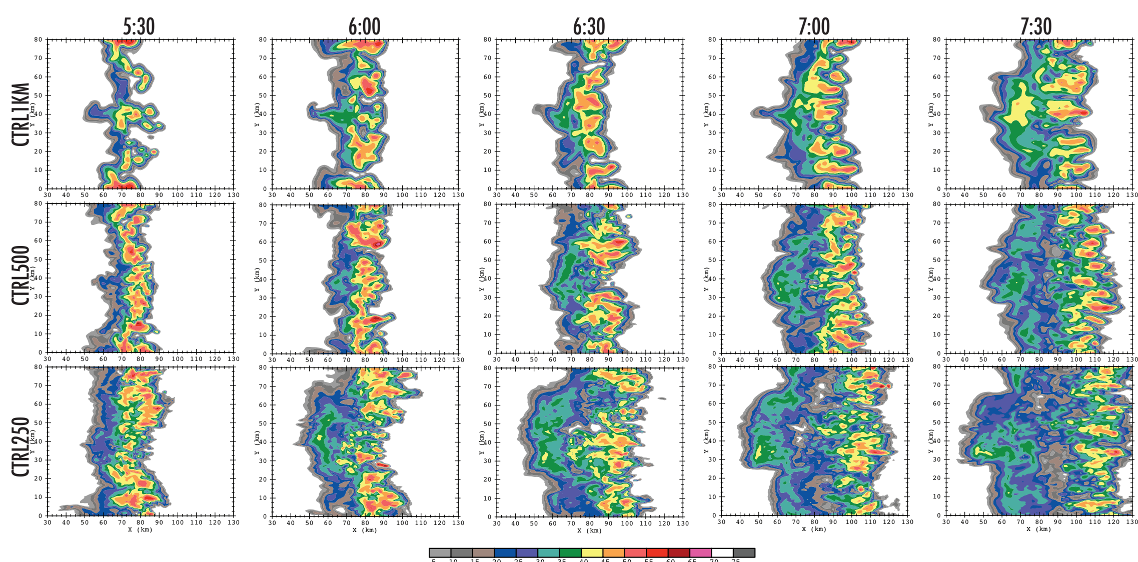

Figure 4.17: Surface reflectivity for the resolution test group from 5-7 hours.

The evolution of the three experiments contained differences in convective mode, line speed, and stratiform rain development (Figs. 4.17and 4.18). The CTRL1KM system exhibited fewer, more intense cells in the convective line than the other two cases. From the surface reflectivity plots (Fig. 4.17), only 4-5 main convection cores with $>$ 50 dBZ are present across the 80 km domain at 5.5 hours. Over 10 cores were present at the same time in the CTRL250 case. These modes of convection were manifest in θ_e analyses (Fig. 4.19) similar to those in Bryan et al. (2003). At coarse grid spacing, convection was more slab-like, and as grid spacing narrowed the resolved turbulent motions caused more entrainment and smaller areas of intense convection (Fig. 4.20). This was a favorable result, as observed squall lines typically have multicellular convective lines (Parker and Johnson 2000).

The speed of the system was nearly constant for the first five hours of the simulations, where reflectivity was centered at approximately x = 75 km. By 5.5 hours, CTRL1KM and CTRL500 advanced approximately 2 km (not including the grid translation speed), whereas CTRL250 shifted nearly 10 km eastward. This trend continued through the end of the simulation, shown at 7 hours in Figure 4.17 with convection reaching approximately x = 110, 120, and 130 km in the CTRL1KM, CTRL500, and CTRL250 experiments, respectively.

Concomitant with the speed trend, the stratiform region was established earlier for finer grid spacing. At 5.5 hours, CTRL1KM and CTRL500 had very small regions of $\sim$40 dBZ surface reflectivity, spanning only a couple of kilometers, and very close to the convective line. CTRL250, however, had a large area of $>$35 dBZ surface reflectivity, spanning over 25 km in the north-south direction, and relatively distant from the convective line (Fig. 4.18). The transition zone low-reflectivity gap between the convective line and stratiform region was maintained, and the entirety of precipitation in CTRL250 covered a much larger area than either CTRL1KM or CTRL500.

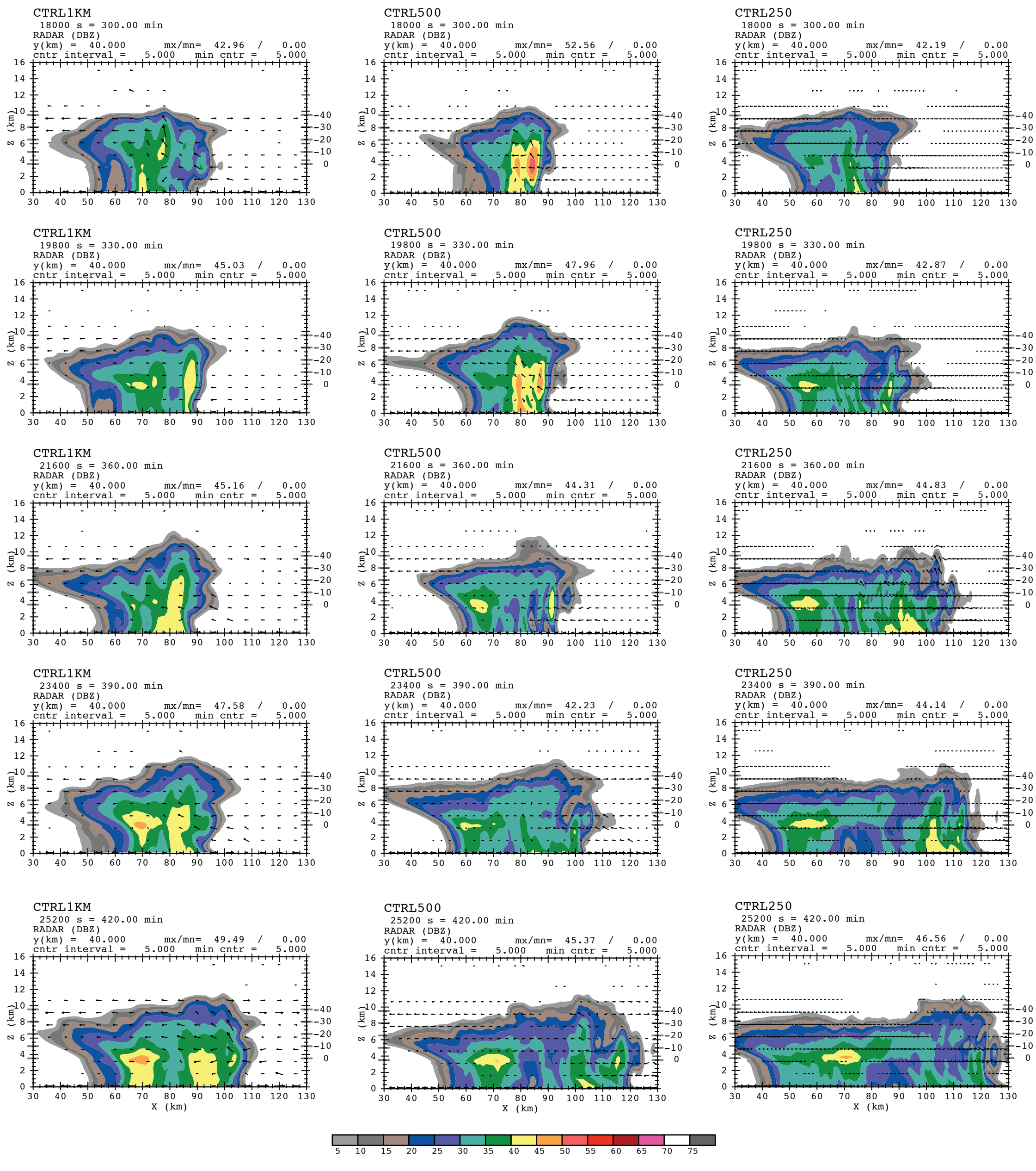

Figure 4.18: 10-km line-parallel average vertical reflectivity and wind vectors along centerline of 4.17.

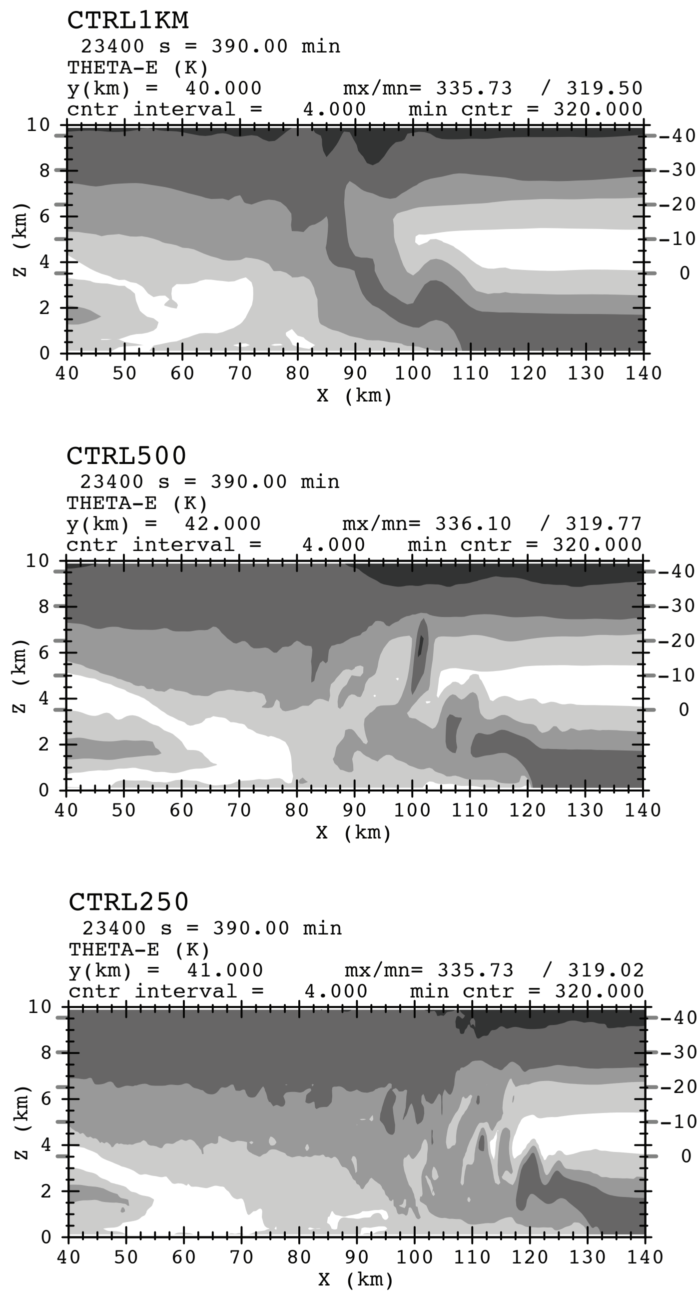

Figure 4.19: Vertical depiction of θ_e for CTRL1KM, CTRL500, and CTRL250 at (a) y=40, (b), y=42, and (c), y=41, respectively. Contours begin with white area for θ_e below 322K, increasing by 4K. Darkest shading is above 334K.

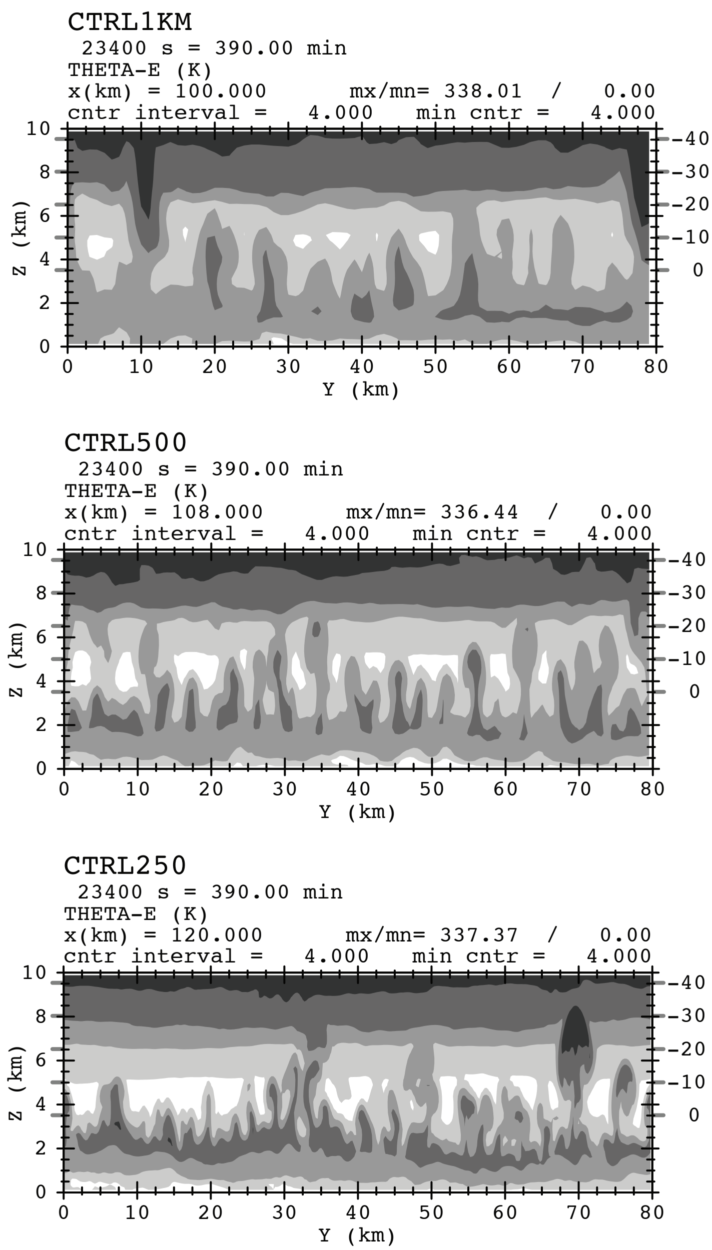

Figure 4.20: Along-line vertical cross sections ahead of convection at (a) x=100km, (b) x=108 km, and (c) x=120 km. Contours are as in 4.19.

4.2.1 Electrification and lightning variations from differences in grid spacing

Time series of IC and CG flashes for each case shows how sensitive the electrical properties are to the dynamical resolution (Fig. 4.21). A difference between the runs was the IC flash rate. In CTRL1KM, IC flashes were relatively steady at 100 per min until 4 hours, at which point they increased over the next half hour to 250 per min. These flashes cycled for the remainder of the simulation, but stayed in the 150-250 range. The CTRL500 experiment had an increase in IC flash rates almost immediately, from about 75 per min to 140 per min. The system had a steady flash rate for the next two hours, around 120 per min, then cycled from as high as 160 per min, averaging about 110 per min, to the low of 55 per min near the end of the simulation. In contrast to either CTRL1KM or CTRL500, the CTRL250 simulation began with the highest flash rates, only to go through two more periods of steady, lower flash rates. The earliest peak was nearly 140 flashes per min, then the system leveled out and maintained approximately 80 flashes per min until about 5.5 hours, when again the rate dropped to about 58 per min.

The rates for all CG flashes were very cyclic in the CTRL1KM case. With a few exceptions, both +CG and −CG flash rates tended to peak at the same time. Negative CG flash rates peaked around 3 per min, coincident with +CG flash rates of about 2 per min. The CTRL500 experiment was also cyclic, with much higher CG flash rates than either of the other two cases. Total CG flash rates exceed 8 per min just after 5 hours, when the system itself entered mature phase (i.e., the stratiform rain region was present). Through approximately 6.5 hours of simulation time, there was a nearly one-to-one correspondence between −CG and +CG. After 6.5 hours, −CG were more frequent (2-3 per min) and +CG flashes occurred less than once per minute. Rates for CG flashes in CTRL250 were relatively low, never exceeding 3 per min. Initially, −CG flashes were in the 0.5-2.5 per min range, but steadily

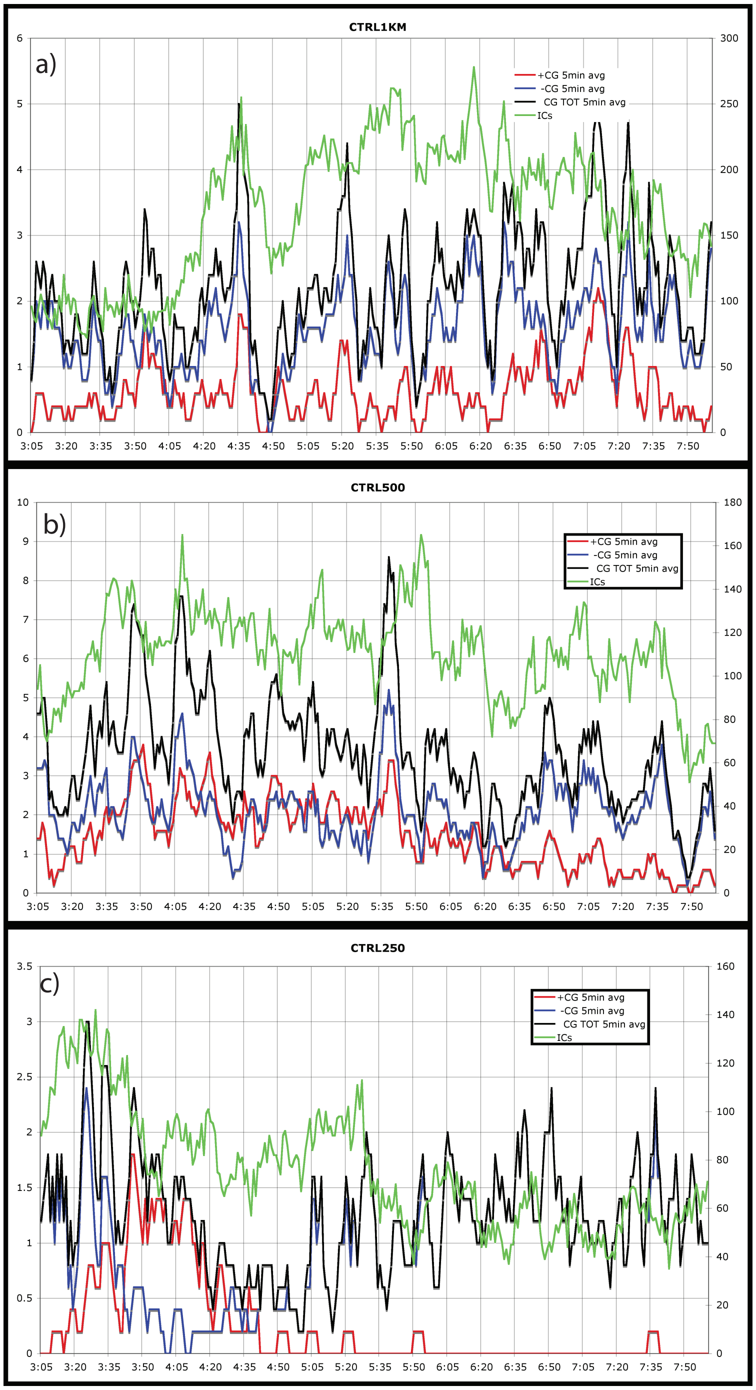

Figure 4.21: Lightning flash rates for a) CTRL1KM, b) CTRL500, and c) CTRL250. IC flashes are green on the right ordinate,Cloud-to-ground flashes are on the left ordinate with total CGs in black, +CG in red, −CG in blue. CG flashes are smoothed with a 5-minute running average. Note the differences in scales.

declined through 4 hours. Meanwhile, the +CG flash rate increased to almost 2 per min, then decreased through 4.75 hours until +CG were negligible for the remainder of the simulation, with only one in the last two hours.

While intracloud flash rates tended to decrease with increasing resolution, the maximum charge neutralized increased with increasing resolution (Fig. 4.22). Corresponding to the evolution trend, CTRL250 reached a maximum before CTRL500, which preceded CTRL1KM. The overall trend for decreasing flash rates with increasing resolution was compensated by the amount of charge discharged per flash and the total IC discharge. When the system was in steady state, the total charge neutralized per minute by intracloud flashes was in the range of 1400-3000 C for CTRL1KM, compared to 600-3100 C for CTRL500 or 800-2500 C for CTRL250. Normalizing the total charge by the number of flashes, the charge per flash was fairly similar, but demonstrated an increasing trend from about 7-14 C in CTRL1KM to approximately 15-30 C in CTRL250. Thus, although the flash rates decreased with increasing resolution, the amount of charge neutralized per flash increased.

4.3 Hypotheses Group

The essence of this research was to test the efficacy of laboratory-supported and theoretical electrification mechanisms and their ability to produce observed charge structure, particularly near the melting level, in a three dimensional model. The previous test groups were designed to determine appropriate microphysical parameters, underlying non-inductive charging schemes, and the choice of grid spacing, in order to proceed with an adequate benchmark experiment (CONTROL) on which to numerically test the proposed mechanisms. This section systematically tests each of the hypotheses laid out in Section 1.2, beginning with the main hypothesis experiment (DRAKE).

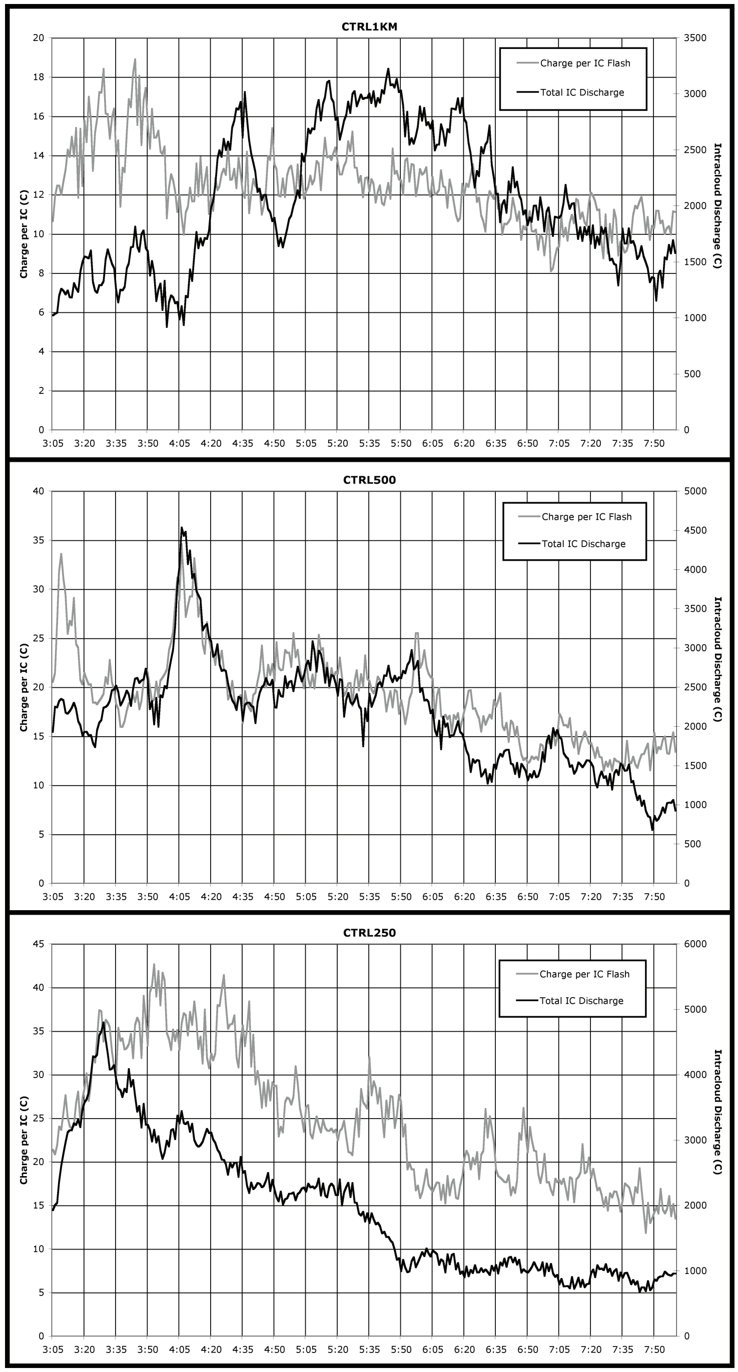

Figure 4.22: Total charge neutralized per minute by intracloud flashes, and per flash (C). Total discharge is in black on the right ordinate, per flash is in gray on the left ordinate. Note the differences in scales.

4.3.1 Non-inductive, collision-free charge separation

The co-location of strong charge layers with the 0°C isothermal layer seems to implicate melting as a possible cause for charge separation. Using Drake (1968) as a basis, the mechanism was tested in the DRAKE case. With identical dynamical evolution to CONTROL, the electrical solution is described as follows.

Shortly after "turning on" the primary non-inductive charging scheme at 3 hours, the convective line exhibited the main charge regions of a normal tripole, on average (Fig. 4.23). A significant difference between the two simulations was a lower negative charge region was present for the DRAKE case near the 0°C isotherm, even in the early stages of development (Fig. 4.24). Otherwise, both cases showed a small region of negative charge around −30°C, which appeared to be embedded within a much larger region of postive charge. This weaker charge region persisted during the development phase of the system. There were also slight differences in the uppermost charge regions, primarily manifest as weaker charge in the DRAKE case compared to the CONTROL case. The main charge regions were otherwise similar in extent and magnitude.

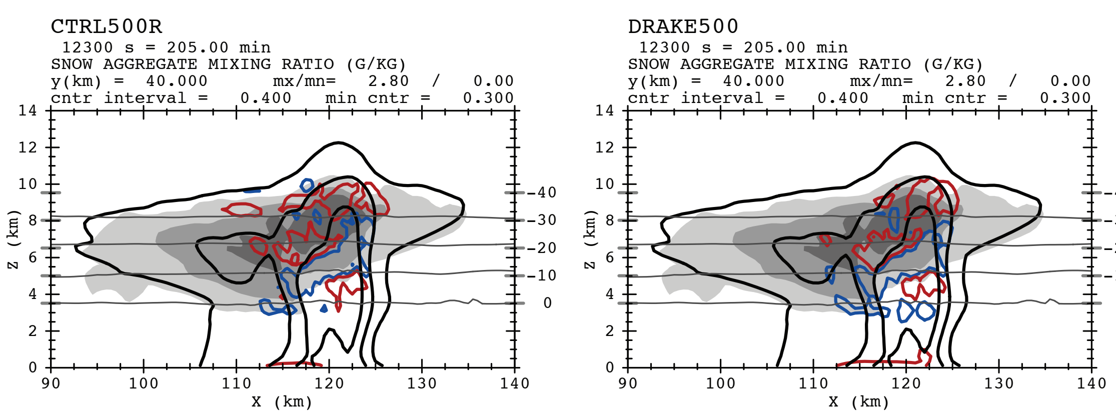

Figure 4.23: Domain-width averaged reflectivity and net charge above 0.1 nC m^{-3} (+ red, - blue) with shaded regions of mixing ratio (0.3, 1.0, 2.0) for the centerline of CTRL500 and DRAKE500.

Later in the simulation, the main charge regions present in the convective line in the DRAKE case extended rearward into the transition zone with a gentle slope (Fig. 4.24). Maximum and minimum local charge densities in the main charge regions frequently reached 10 and -8 nC m^{-3}, respectively. Although fairly small areas, regions of significant charge were closer to $\pm$4 nC m^{-3}. What appeared to be the top of the main positive charge region in the early times, now has distinct separation and an equally strong upper negative charge layer. These layers are significant enough to be visible in the domain width average for the CONTROL case, but were absent in DRAKE case. However, there are local occurrences of weak upper charge layers present in DRAKE for select 4 km averaged vertical cross sections (Fig. 4.25).

The lower negative charge that was present in the DRAKE case clearly extends into the stratiform region and is completely absent in CONTROL beyond 6 hours. Although the charge magnitude was weak, generally -0.2 nC m^{-3}, it was significant and spanned a large horizontal area. The negative charge region was accompanied by a positive corona charge at the surface indicating stronger upward electric fields at the ground. While this was the only case with widespread significant charge near the 0°C isotherm, observations show both polarities of charge, with positive charge above the negative charge region. The absence of a positive charge layer will be discussed in Section 5.3.1.

The only variation in flash rates among the Hypothesis Group tests was between CONTROL and DRAKE (Fig. 4.26). For all tests, intracloud and -CG flash rates were so similar, only CONTROL and DRAKE are plotted here as examples. Likewise, +CG flash rates were similar among all cases, other than DRAKE, which contained far fewer +CG than the rest of the group. For example, DRAKE produced only 12 +CG flashes in the last 2 hours of simulation time, whereas CONTROL produced 82.

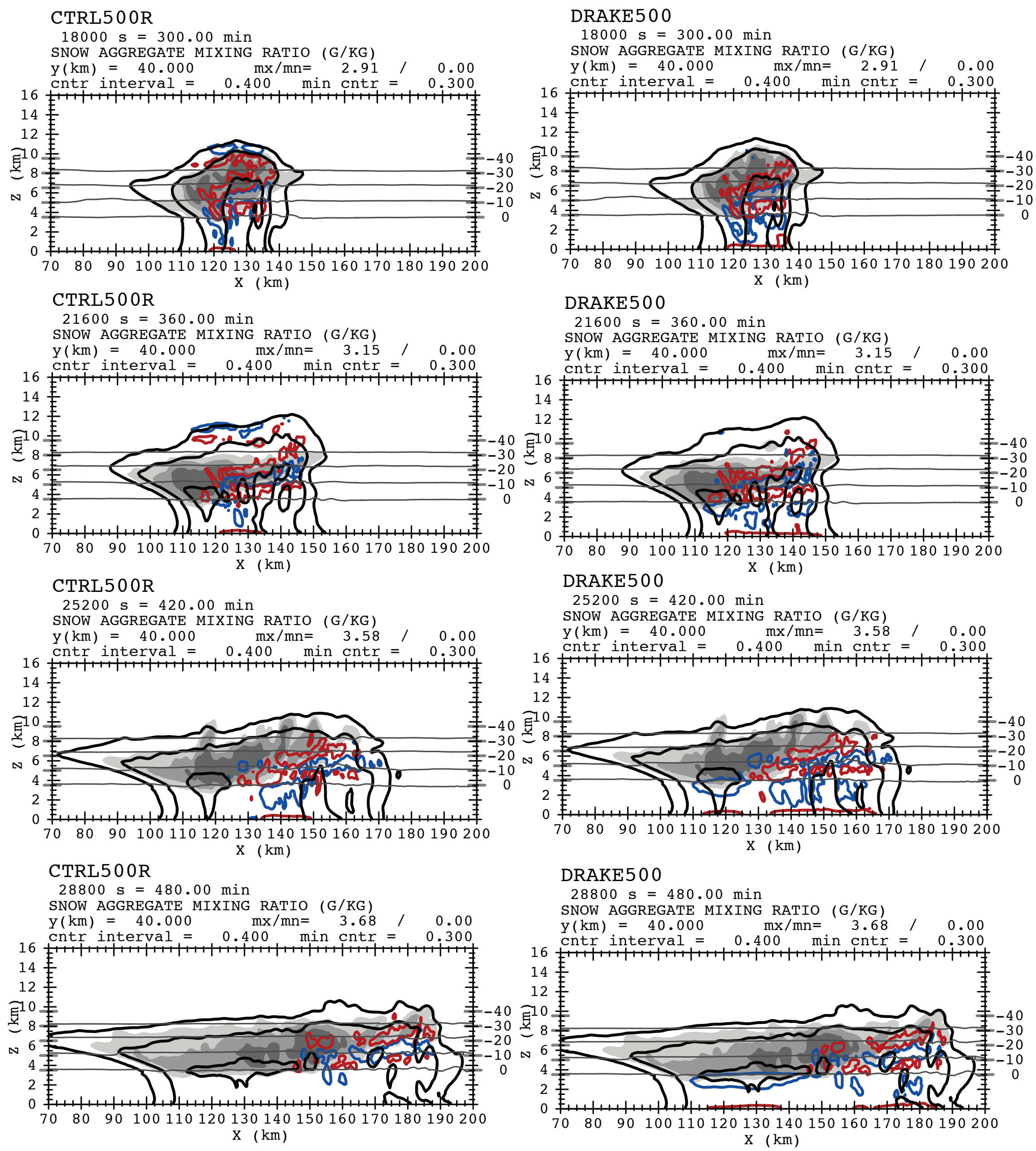

Figure 4.24: Domain-width averaged reflectivity and net charge above 0.1 nC m^{-3} (+ red, - blue) with shaded regions of mixing ratio (0.3, 1.0, 2.0) for CTRL500 and DRAKE500 at 1 hour intervals.

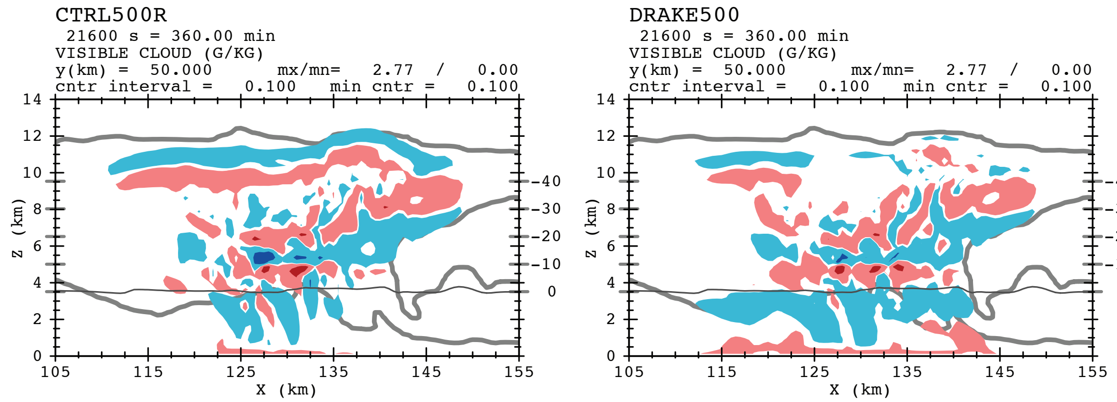

Figure 4.25: Net charge (nC m^{-3}) along y=50 km, averaged over 4km. Charge density (solid contours) in nC m^{-3} for values > 0.1 light red, > 1.0 dark red, < 0.1 light blue, and < 1.0 dark blue.

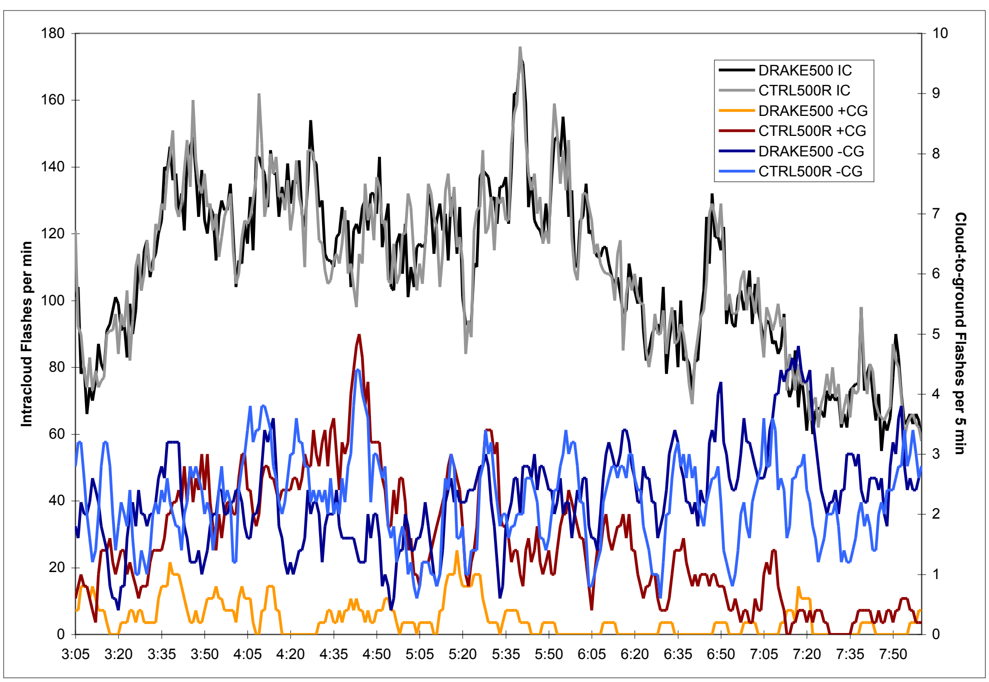

Figure 4.26: Intracloud flashes per minute, and ±CG per 5 minutes for CONTROL and DRAKE.

4.3.2 Charge acquired during deposition

Given the large amount of snow observed near the bright band, and thus near the main region of consideration, it is possible charge separation occurs through a snow process. For the case allowing charge to be acquired during deposition on snow (DONGHALLETT), the solution differences were not as pronounced as in DRAKE. Charge structure in the convective line had only slight variations from the CONTROL test, and maintained the normal tripole alignment (Fig. 4.27). Along-line averages showed slightly amplified negative and positive charges above the convective line, in the -30 to -50°C temperature range. There was very little difference in average charge amplitude in the transition zone. The stratiform region remained free of charge as in the CONTROL case.

In contrast, larger charge densities were present in the convective line of non-averaged cross-sections at a later time when the stratiform region was fully developed (Fig. 4.28). In this instance, the main charge centers cover a larger area in DONGHALLETT, and were also substantially larger in magnitude (± 3 versus ± 4.5 nC m^{-3}). Directly rearward of the main tripole and below -30°C, negative charge was reduced and positive charge was slightly stronger. Above this region, charge structure remained approximately the same, but positive charge had weaker magnitude. Increased areas of charge existed between the transition zone and stratiform region, although they did not have the continuity purported by observational analyses.

4.3.3 Inductive charging from raindrop disjection

The charging scheme derived from a rain process (CANOSALIST) did little to modify charge structure in an averaged sense (Fig. 4.29). The convective line maintained the normal tripole structure, as well as the sloping charge layers through the transition zone. The charge layers at the upper boundary of the storm existed through 6 hours as in CONTROL. No noticeable charge was present in the stratiform region

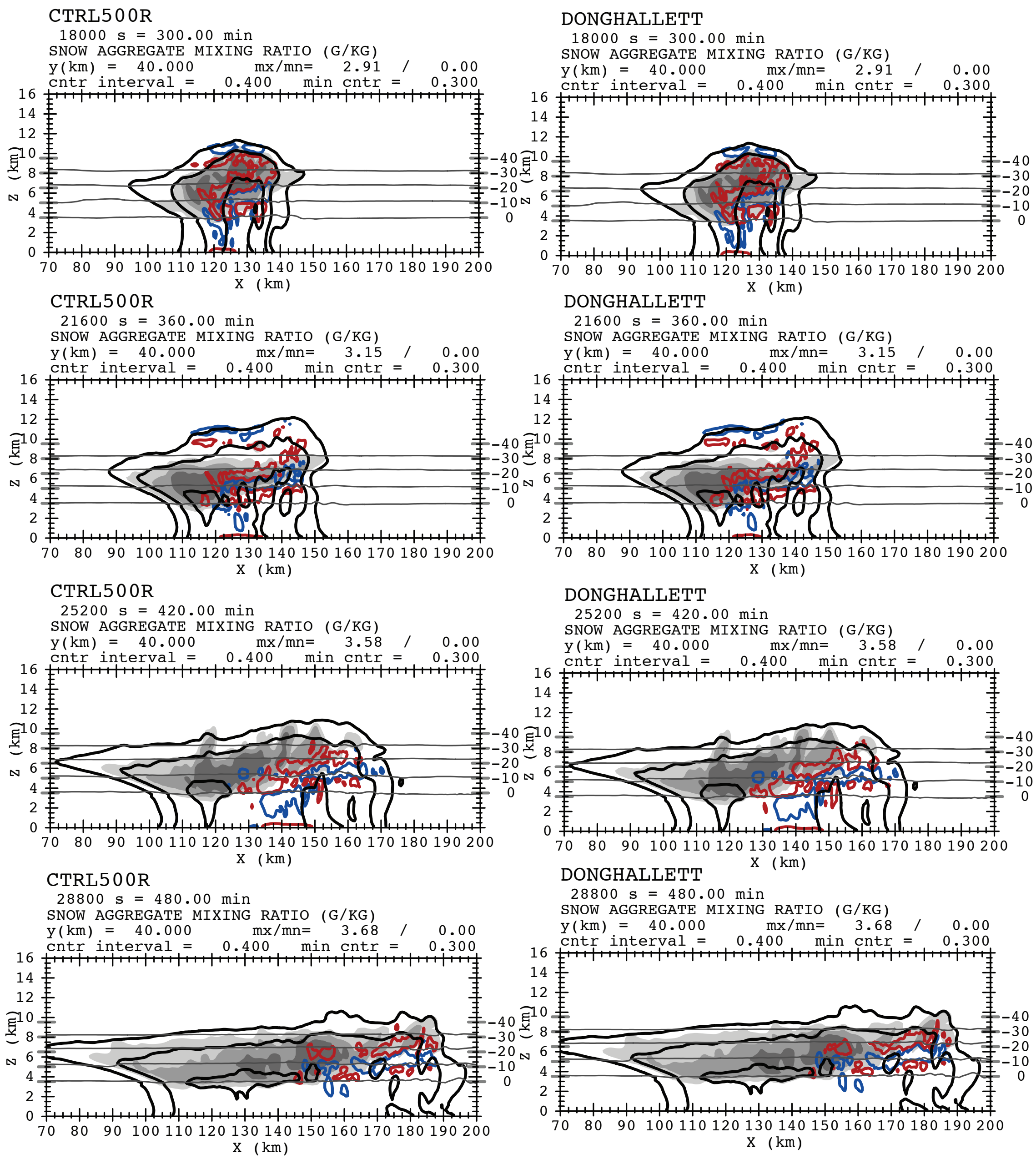

Figure 4.27: As in 4.24, for DONGHALLETT.

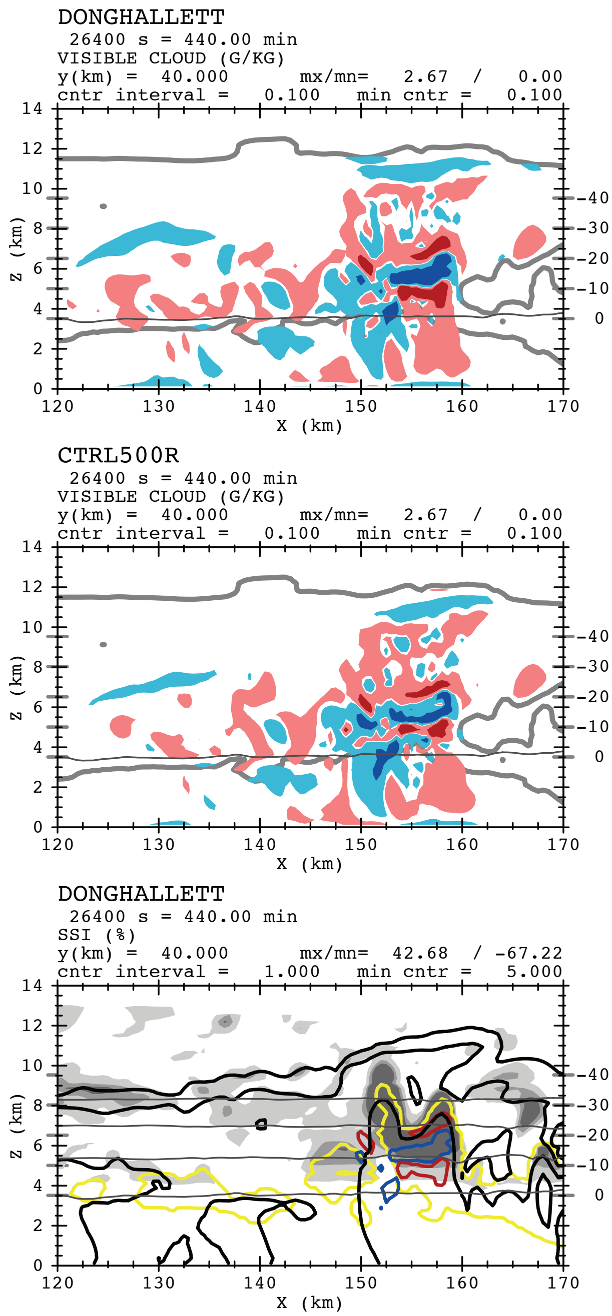

Figure 4.28: Top and middle: Charge density at centerline for 7 h 20 min (solid contours) in nC m^{-3} for values > 0.1 light red, > 1.0 dark red, < 0.1 light blue, and < 1.0 dark blue. Bottom: liquid water content above 0.01 g kg^{-1} (yellow), and ice supersaturation of 5,10,15% in grey shading. Red and blue contours are positive and negative net charge above 1 nC m^{-3}, respectively. Reflectivity is 5-75 by 15 dBZ.

itself. There were some small differences ahead of the convective line above −20°C, from about 150 to 165 km at 7 hours. At lower levels, charge magnitude was diminished in the transition zone, particularly at later times. The analysis at 8 hours shows weaker charge from 155 to 165 km below −10°C.

The minor differences between CONTROL and CANOSALIST in the magnitude and structure of charge density in the averaged analyses were also reflected in the non-averaged cross sections (Fig. 4.30b). Most often the inductive rain charging acted to increase the overall charge density but did not impact the structure significantly. In Fig. 4.30, the charge centers near x = 125 km just above the 0°C isotherm are much stronger in CANOSALIST than CONTROL. Because there was very little rain mass in this area, the charge was associated with graupel and snow, not directly with rain, and will be examined further in Section 5.3.3.

Intracloud flash rates were very similar to the CONTROL case, reaching a maximum of approximately 175 flashes per minute around 5 hours 40 minutes of simulation time. As in DRAKE and DONGHALLETT, the CG maximum around 4 hours 45 minutes did not occur in CANOSALIST. Both DONGHALLETT and CANOSALIST had a relative maximum in CG flash rates around 6 hours 15 minutes. The majority of these flashes were initiated in strong cells in the northern half of the system (Fig. 4.31). After reaching this maximum, −CG flashes continued at approximately the same rate, but +CG flashes decreased by over 50%.

4.3.4 Non-inductive, collisional charging without liquid cloud water

The domain width averaged analyses revealed only minor differences between the simulation that allowed charging without liquid cloud water (MST06) and the CONTROL experiment (Fig. 4.32). However, shorter range averages showed some differences that are likely due to differences in removal of charge by lightning (Fig. 4.33).

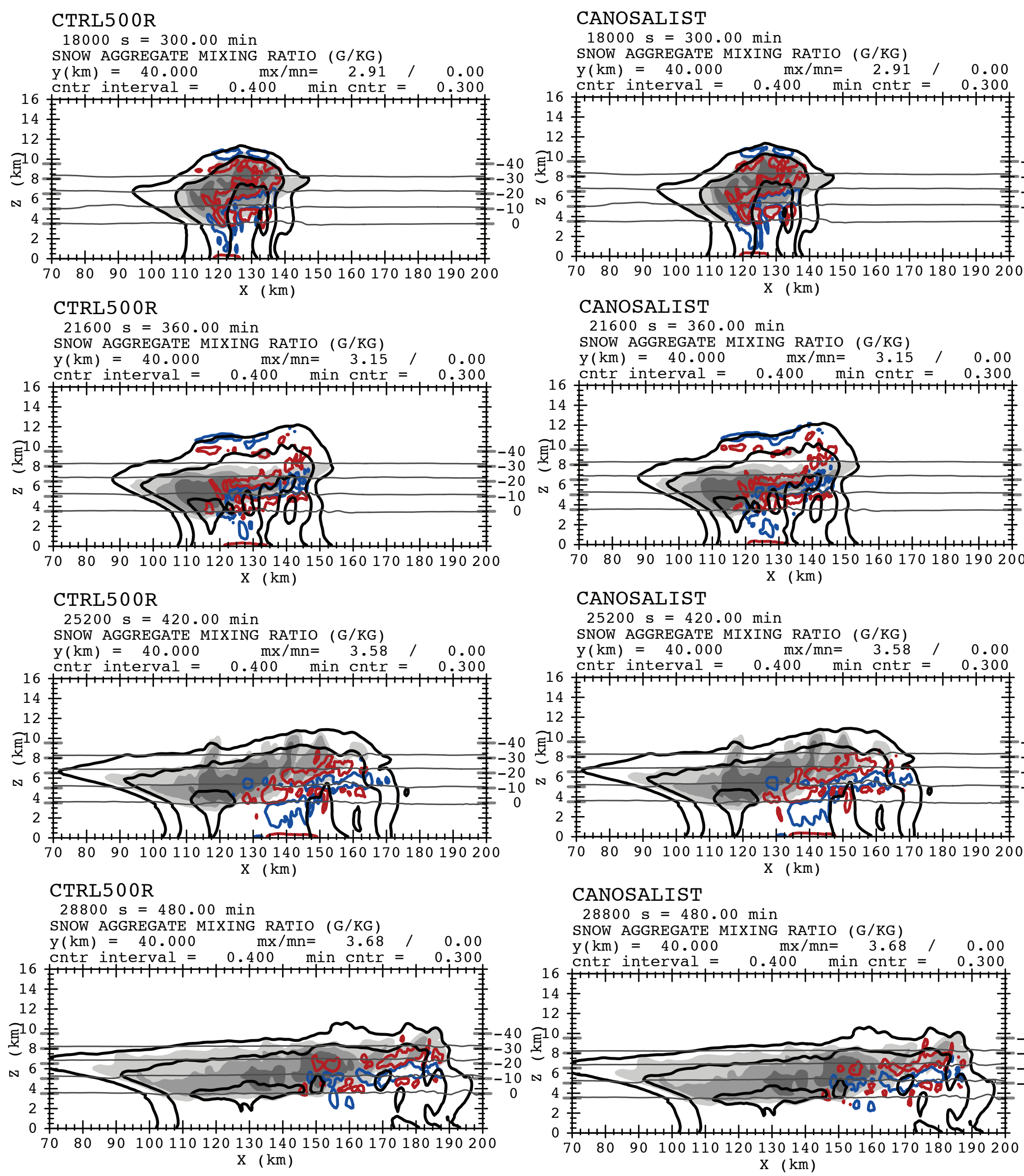

Figure 4.29: As in 4.24, for CANOSALIST.

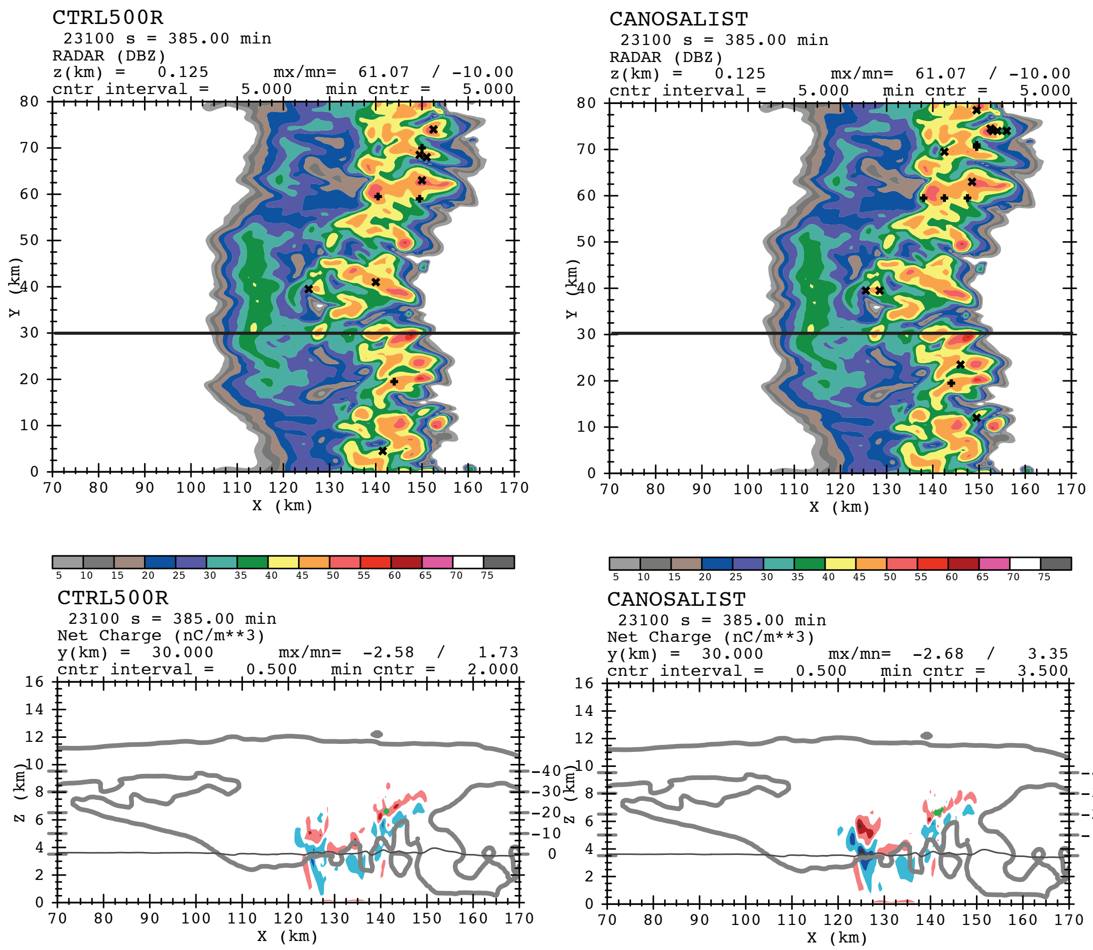

Figure 4.30: Top panels are surface reflectivity with CG flashes denoted by +(pos) and x(neg). Line shows location of vertical cross sections below. Bottom panels are vertical cross sections are net charge density (solid contours) in nC m^{-3} for values > 0.1 light red, > 1.0 dark red, < 0.1 light blue, and < 1.0 dark blue with flash initiation points (green dots).

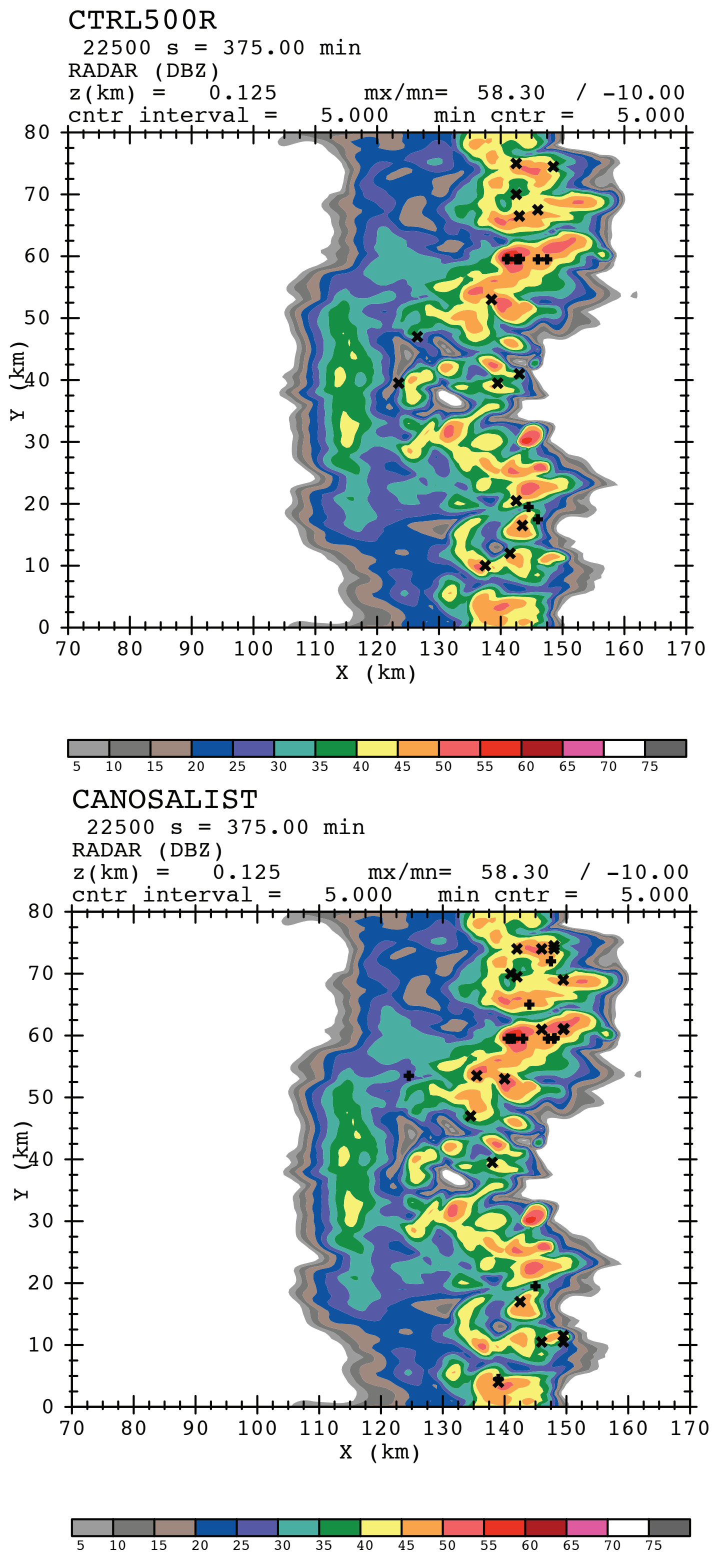

Figure 4.31: Surface reflectivity at 6h 15m and +(pos) -(neg) CG flashes.

The positive charge center at x = 160 km in CONTROL was much weaker in MST06. Instead, at x = 155 km in MST06, there was significant charge of both polarities that was not present in CONTROL.

A closer look at an non-averaged cross section revealed local differences in charging in relation to supersaturation to ice (Fig. 4.34). Note that the region of increased charge densities near x = 155 km was in an area of ice supersaturation, but on the edge of the area containing liquid cloud water, thus allowing the mechanism to be active.

The reflectivity maximum near x = 140 km coincided with an area of strong ice supersaturation and a lack of cloud water. The weak charge in this region was primarily carried on large aggregates and updrafts were very weak, thus there were very few collisions to allow for charge separation. A closer look at this region will be discussed in the next section.

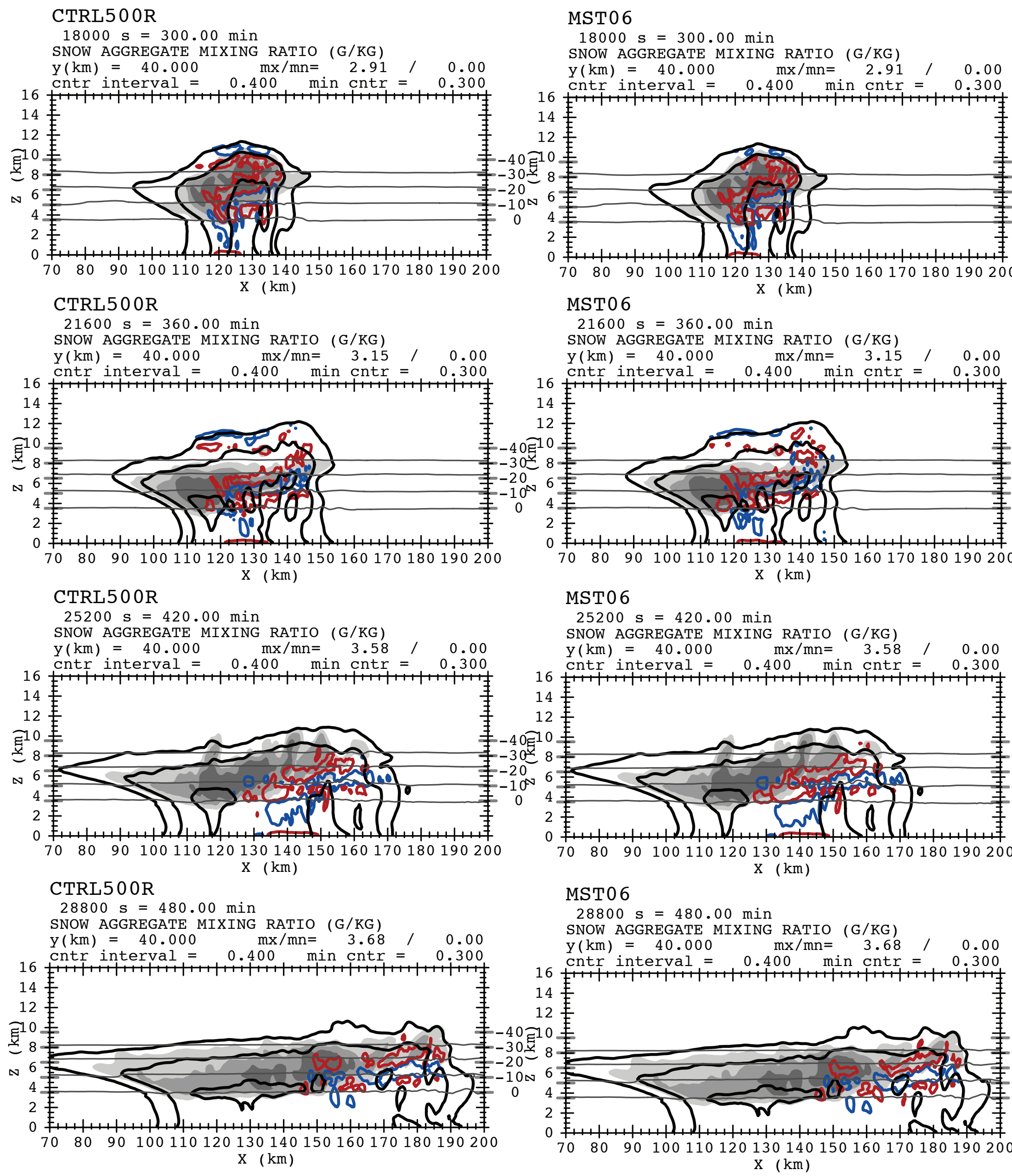

Figure 4.32: As in 4.24, for MST06.

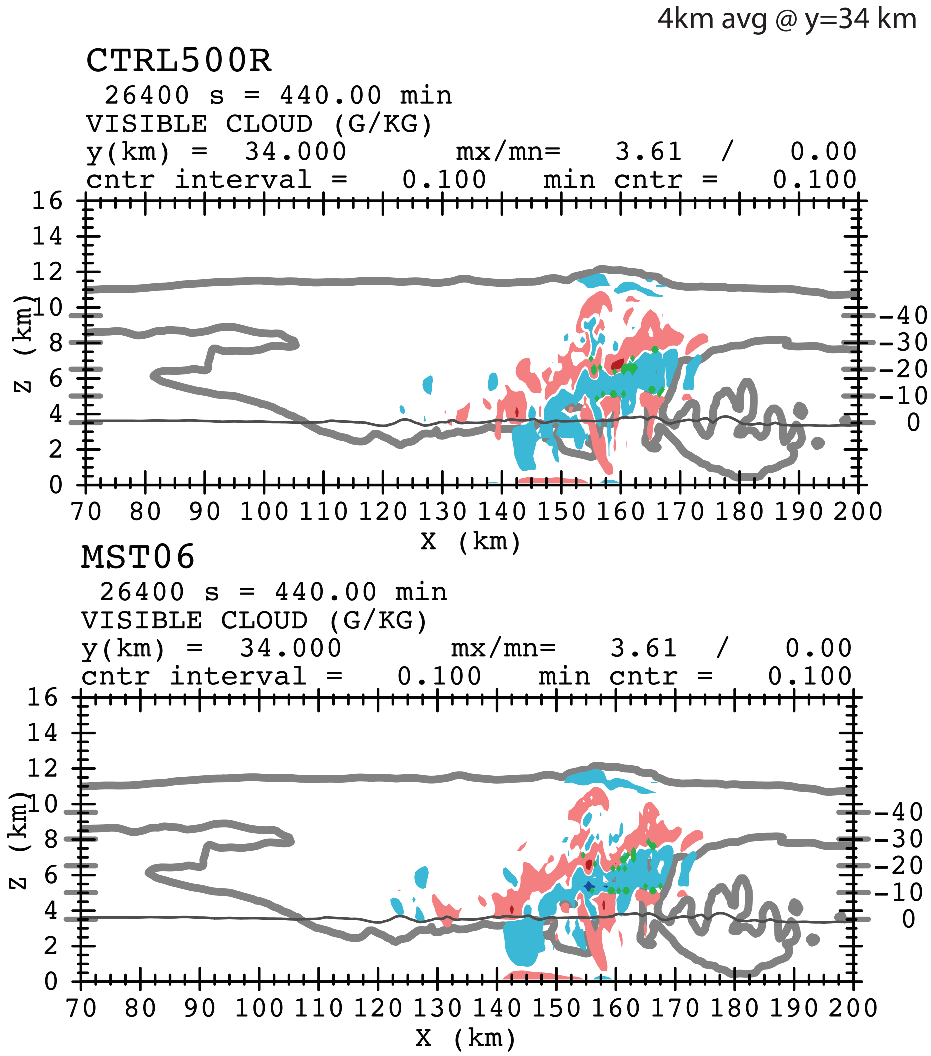

Figure 4.33: Vertical cross section (7h 20m) with 4-km average net charge and flash initiation points at y = 34 km. Light/dark red/blue is 0.1/1.0 nC m^{-3}.

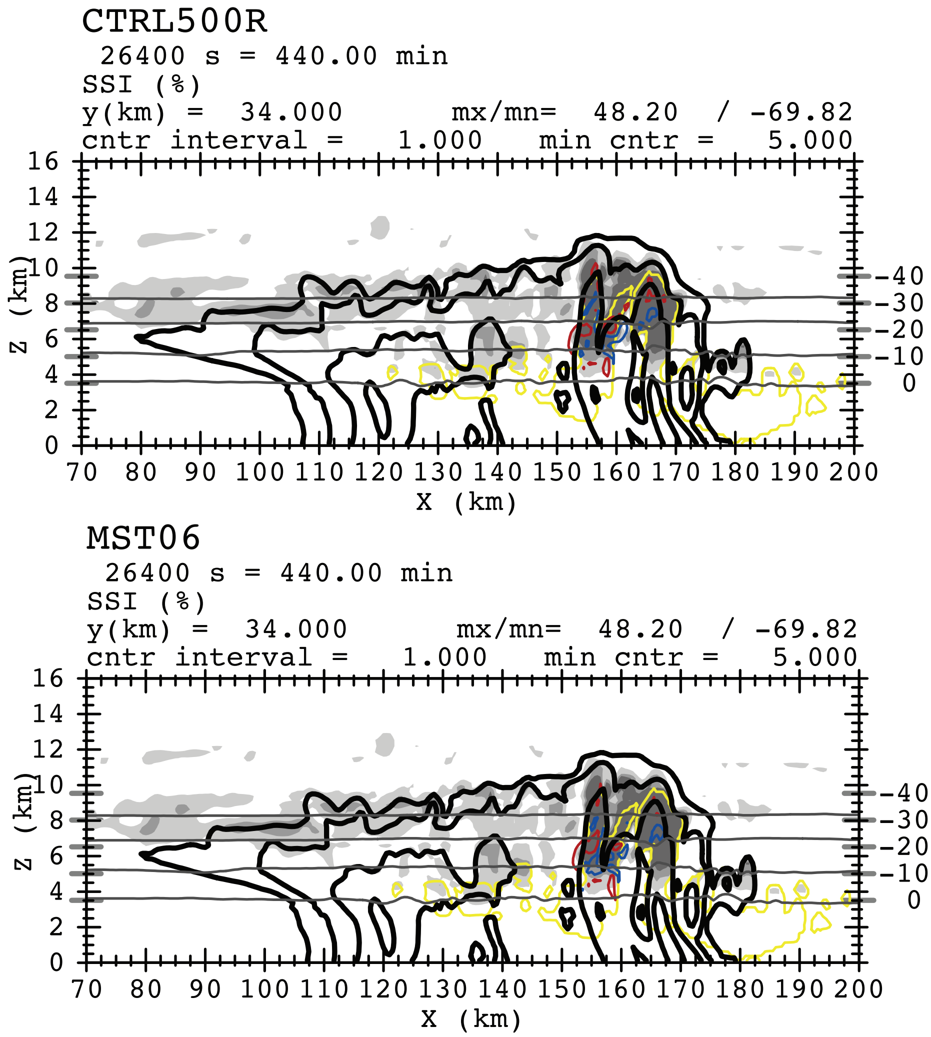

Figure 4.34: Net charge structure at 7h 20m with flash initiation points at centerline. Bottom panel is liquid water content above 0.01 g kg^{-1} (yellow), and supersaturation of 5,10,15% in grey shading. Red and blue contours are positively and negative net charge above 1 nC m^{-3}, respectively. Reflectivity is 5-75 by 15 dBZ. Cross section at y = 34 km.

Chapter 5

Discussion

From the experimental setup, the most noteworthy findings resulted from the inclusion of a liquid water fraction on graupel and snow and dependence on grid spacing. These findings are discussed in detail below. Once applied, the objective was to test various charging mechanisms for any effects on the stratiform charge structure. At this time, only one of the mechanisms was capable of producing significant charge in the stratiform region. The test results are further discussed, with analysis of additional research possible.

5.1 Effects of liquid water coating on wet snow and graupel

As shown in Sec. 4.1.1, there is a decided increase in graupel mass when allowing liquid water to reside on particle surfaces. The particles are larger and more numerous (Figs. 5.1 and 5.2). Some of the variability is explained by the phase lag in the system development. With the slower evolution demonstrated by reflectivity, the graupel concentration time series (Fig. 5.1) provides the clearest evidence of the phase lag. However, once the system reaches steady-state, the mixed phase particle system (CONTROL) maintains higher graupel physical quantities (Fig. 5.3).

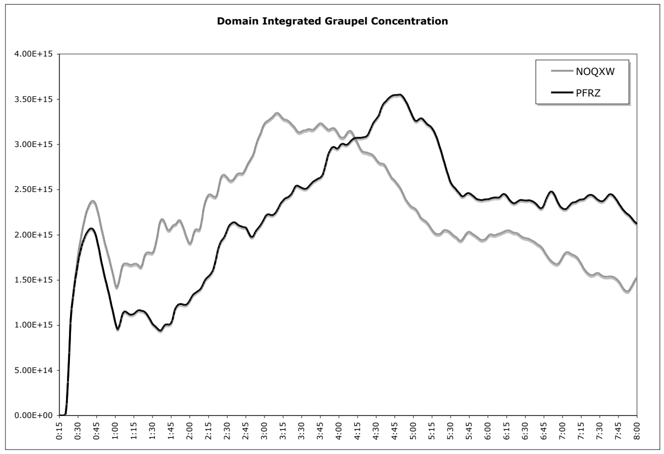

Figure 5.1: Domain integrated graupel concentration (total number).

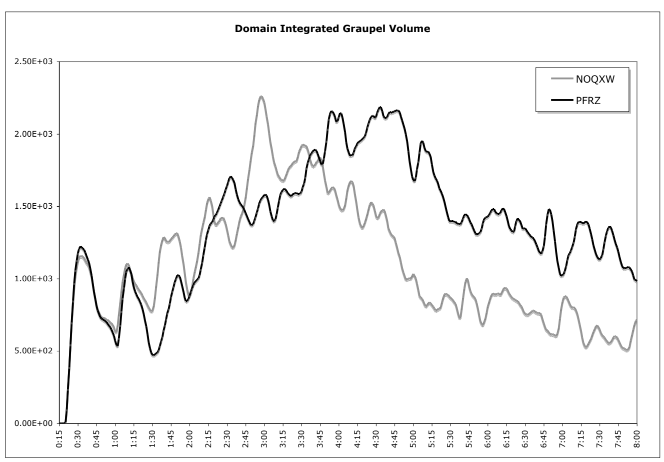

Figure 5.2: Domain integrated graupel volume for $q_h > 0.5$ g kg^{-1}(km^3).

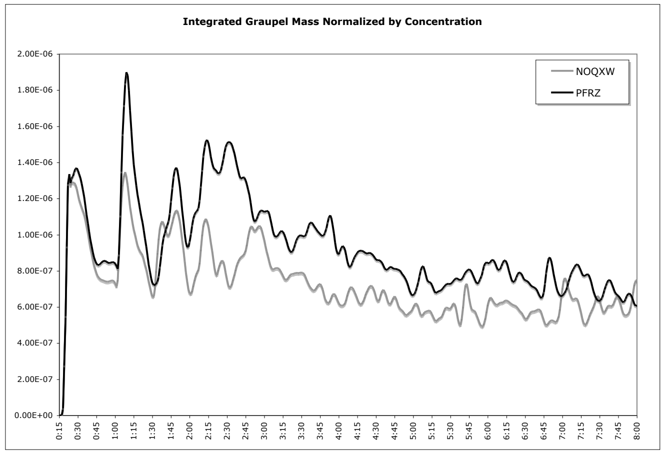

Figure 5.3: Domain integrated graupel mass normalized by total number (kg).

The apparent source of the graupel mass increase is the accretion of cloud water (Fig. 5.4) and, to a lesser extent, collection of cloud ice (Fig. 5.5). Cloud water content is relatively similar for CONTROL and NOQXW, whereas cloud ice mass (and consequently, concentration) increases 10-20% when liquid coated particles are included (Fig. 5.6). For both cases, at temperatures below freezing in a wet growth regime, a graupel particle is assumed to have a wet surface and therefore a collection efficiency of unity. When not in wet growth, and when a wet surface is not parameterized, the graupel-ice collection efficiency has an exponential temperature dependence that ranges from approximately 0.1 to 0.002. The collection efficiency for a particle with a non-zero liquid water fraction, yet not in a wet growth regime, remains at 1 (or 0.5 for graupel-snow collection).

Further support for the increase in ice mass is in part due to larger, more vigorous updrafts in CONTROL after 3.5 to 4 hrs (Fig. 5.7). Updraft mass flux a T=−20°C was generally much greater for the case with liquid water on hydrometeors. The updrafts created more ice and lofted more graupel in mid-levels of the convection (Fig. 5.8).

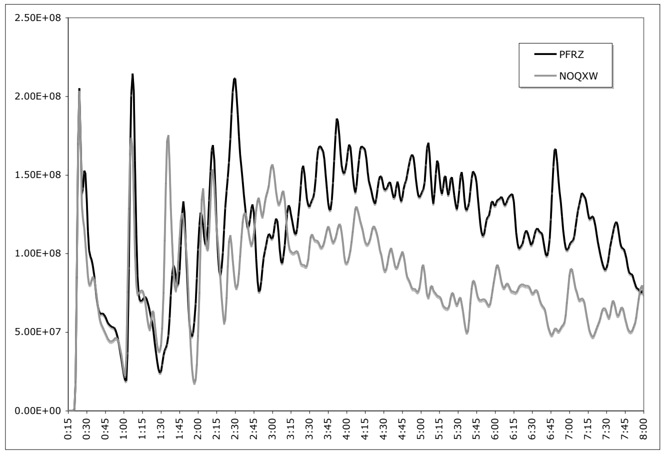

Figure 5.4: Domain integrated mass acquired by graupel through accretion of liquid cloud water (kg).

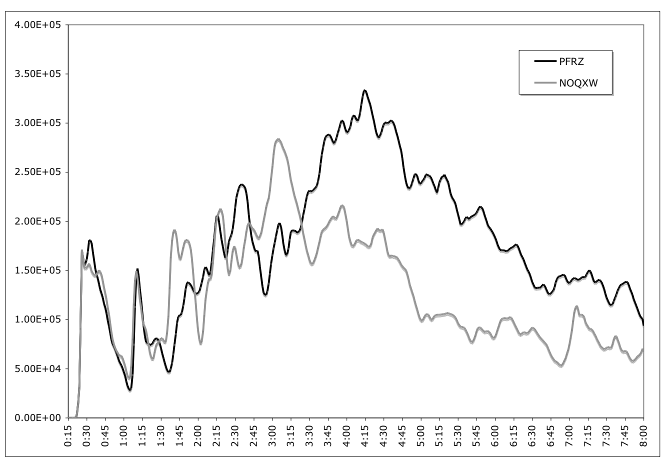

Figure 5.5: Domain integrated mass acquired by graupel through collection of cloud ice (kg).

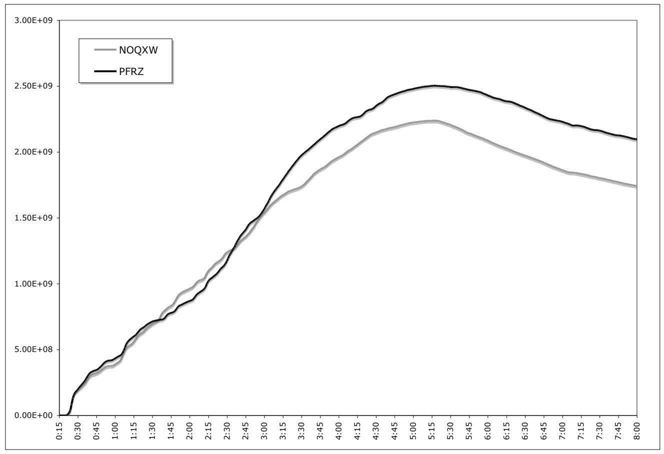

Figure 5.6: Times series of domain-integrated ice crystal mass (kg).

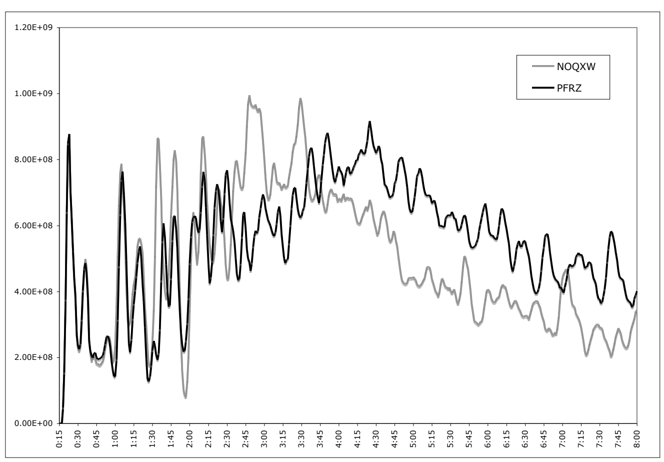

Figure 5.7: Updraft mass flux (kg) at T=-20°C.

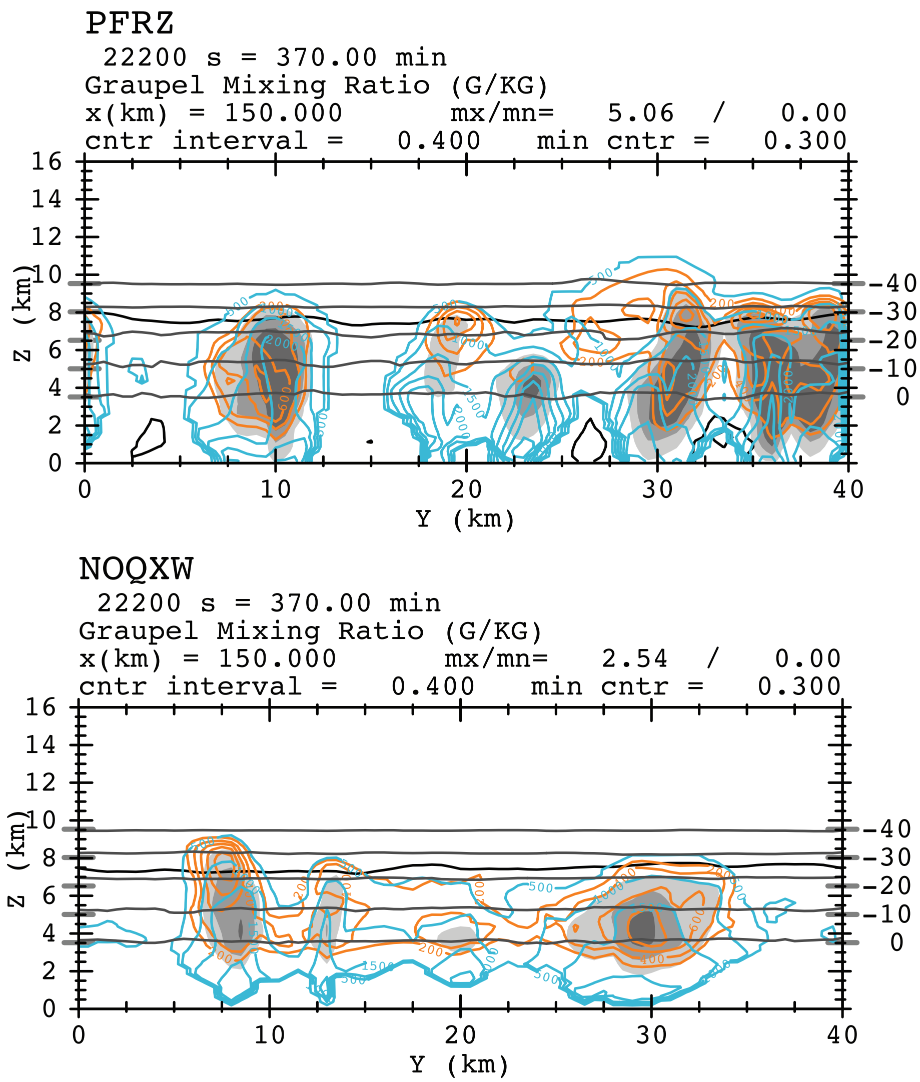

Figure 5.8: light/dark grey fill Q at 0.3 1.0 and 2.0 g/kg; D_{graup} in blue by 500 microns; graupel concentration in orange by 200 per L, reflectivity is 5-75 by 10dBZ; Temp by 10°C from -40 to 0°C.

5.1.1 Electrification

The implications of the larger mean graupel mass are apparent in the net charge results (Fig. 4.12). The lack of volatility in net charge is due to lightning discharging excess charge, yet the overall trend is higher net charge when including mixed phase particles. After approximately 3 hrs 45 mins, domain-integrated charge remains steady in CONTROL until approximately 5 hrs, whereas it steadily declines after 3 hrs 45 mins in NOQXW.

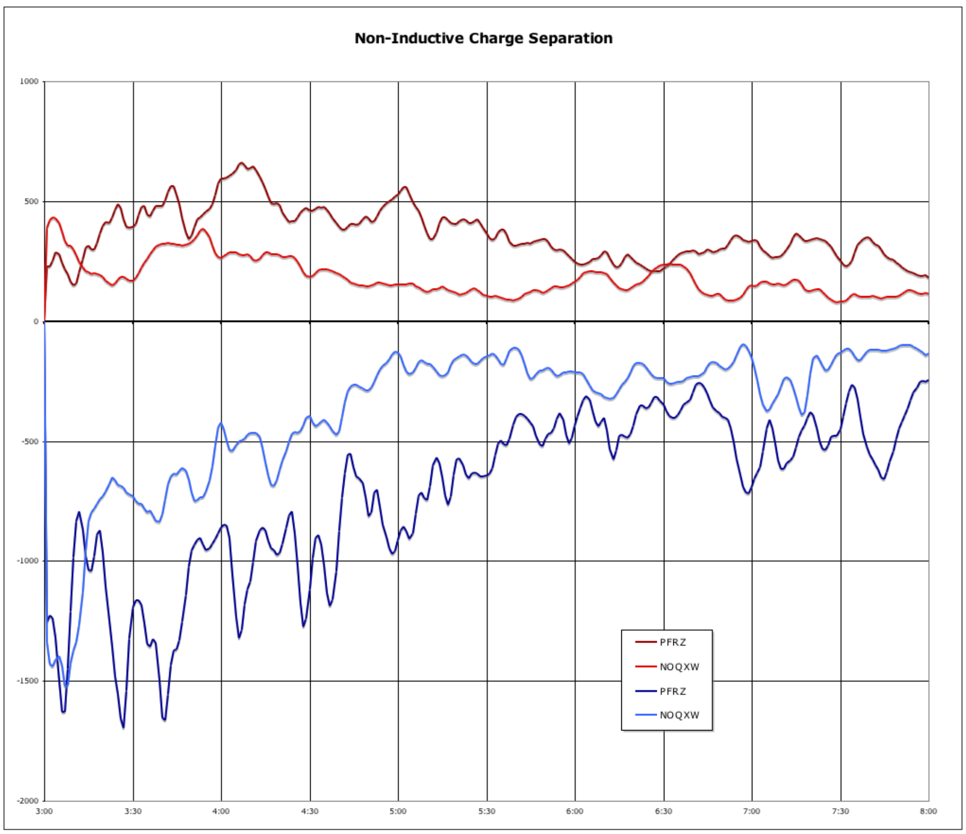

Figure 5.9: Domain integrated non-inductive charge separation rate for CONTROL (dark red/blue) and NOQXW (red/blue) in C s^{-1}.

The maintenance of charge in CONTROL between 3 hrs 45 mins and 5 hrs can be attributed to non-inductive charging (Fig. 5.9). Inductive charging is also stronger in CONTROL, but an order of magnitude smaller than non-inductive charging in absolute terms and thus less of a contribution. Specifically, charge separation through graupel-ice and graupel-snow collisions accounts for most of the increase in charge separation between the two cases (Figs. 5.10 and 5.11). Both graupel-ice and graupel-snow collisions separate more charge in CONTROL than NOQXW for the majority of the simulation. This is a result of the increase in size and number of graupel, and ice concentration.

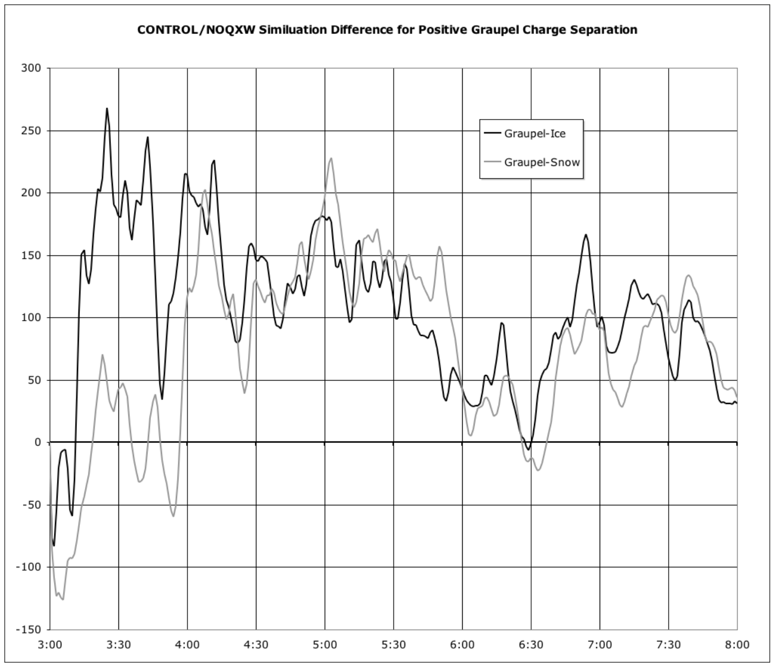

Figure 5.10: Domain integrated non-inductive positive charge separation rate difference for CONTROL-NOQXW for graupel-ice (black) and graupel-snow (gray) in C s^{-1}.

Notably, the first hour of the electrical portion has some variability. Charge acquired by graupel through graupel-snow collisions is stronger for NOQXW for the first 30 minutes. Likewise, graupel acquires more positive charge through graupel-ice collisions than graupel-snow during the first hour of the electrical simulation.

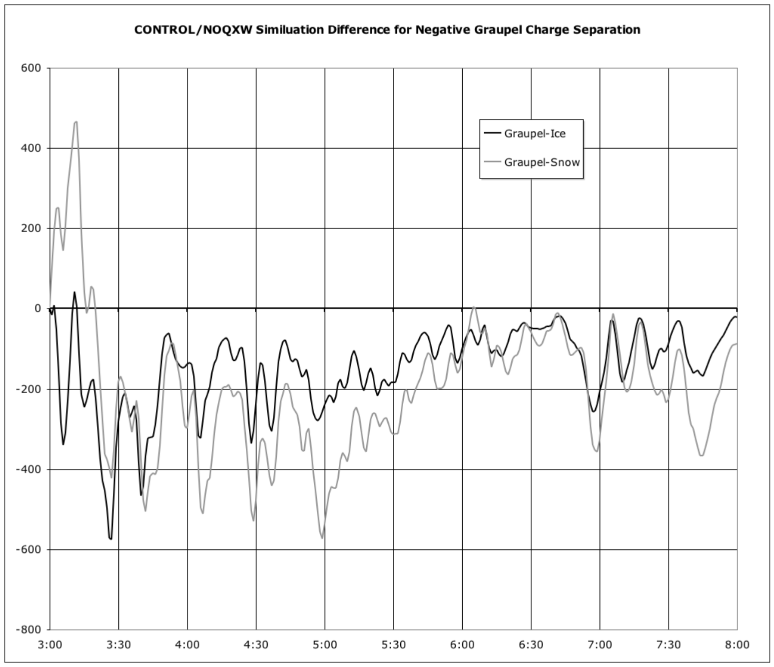

Figure 5.11: Domain integrated non-inductive negative charge separation rate difference for CONTROL-NOQXW for graupel-ice (black) and graupel-snow (gray) in C s^{-1}. Negative values represent more negative charge separation in CONTROL than NOQXW.

5.2 Solution dependence on grid spacing

A dynamical result of the resolution experiments was the faster evolution of the squall line with decreasing grid spacing. Updraft volume (> 20 m s^{-1}) reaches maximum values around 3 hours 30 minutes for CTRL250, 4 hours for CTRL500, and 5 hours for CTRL1KM (Fig. 5.12) . This is followed shortly by maximum values of graupel mass, although CTRL1KM reaches a second maximum following a strong updraft pulse around 6 hours (Fig. 5.13). Likewise, CTRL500 contained a second pulse around 5 hours 30 minutes.

Other ice species did not follow this trend. Snow mass was comparable for the lower resolution experiments, but much higher for CTRL250 (Fig. 5.14). Contrarily, the higher resolution solutions contained similar ice mass for most of the system evolution, with CTRL1KM values greatly reduced (Fig. 5.15).

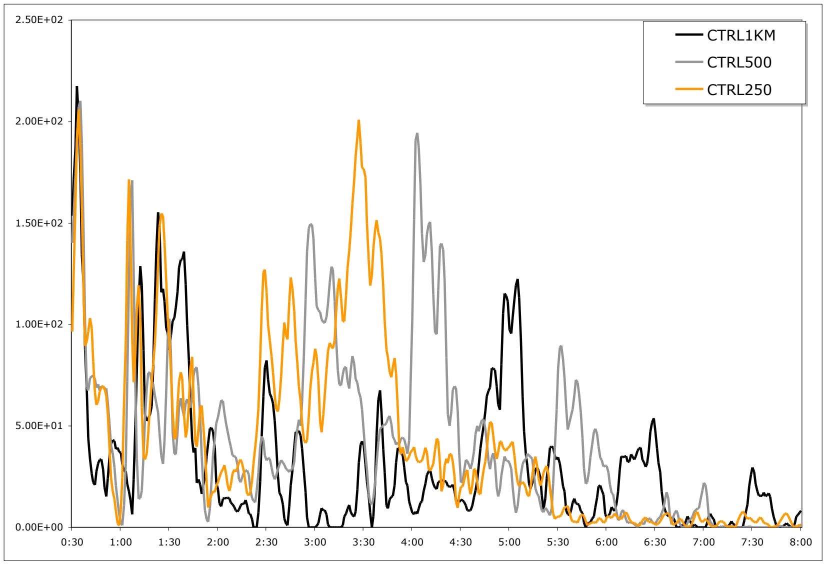

Figure 5.12: Domain Integrated updraftl volume for w > 20 m s^{-1} (kg m^{-3}).

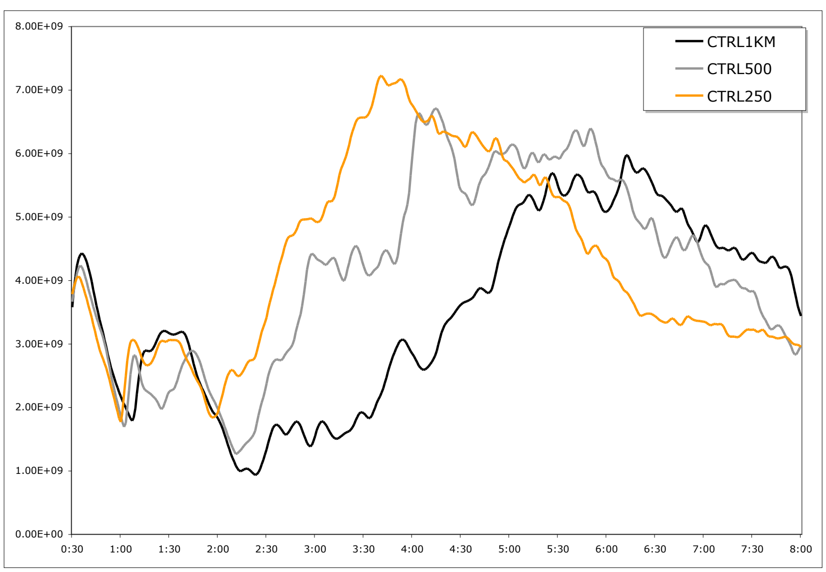

Figure 5.13: Domain Integrated graupel mass (kg).

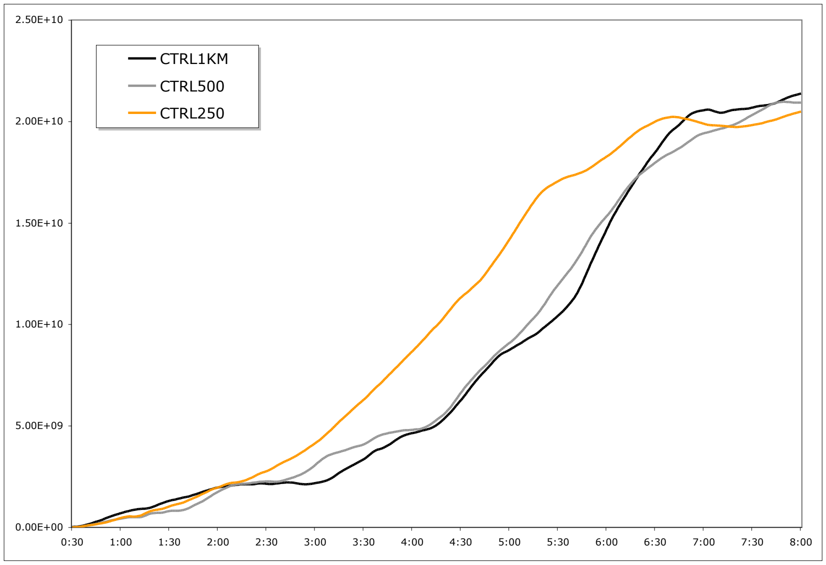

Figure 5.14: Domain Integrated snow mass (kg).

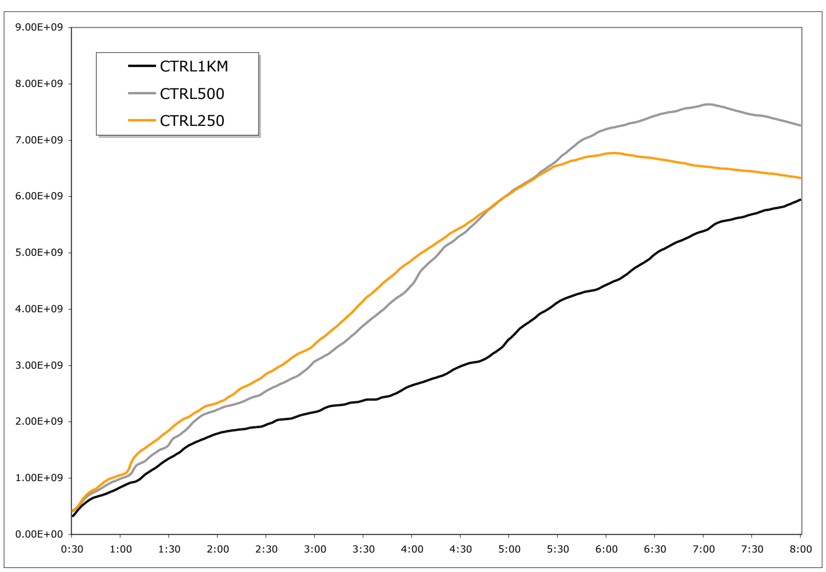

Figure 5.15: Domain Integrated cloud ice mass (kg).

The liquid water fraction initially mimicked the trends of graupel mass, as graupel was more prevalent than ice in the early stages of evolution (Fig. 5.16). Snow mass gradually overtakes graupel mass as the system matured. The slow fallspeeds of snow over a large area, as well as less vigorous convection to elevate and re-freeze liquid on graupel, resulted in a steady growth of liquid water on ice particles until snow mass stopped increasing.

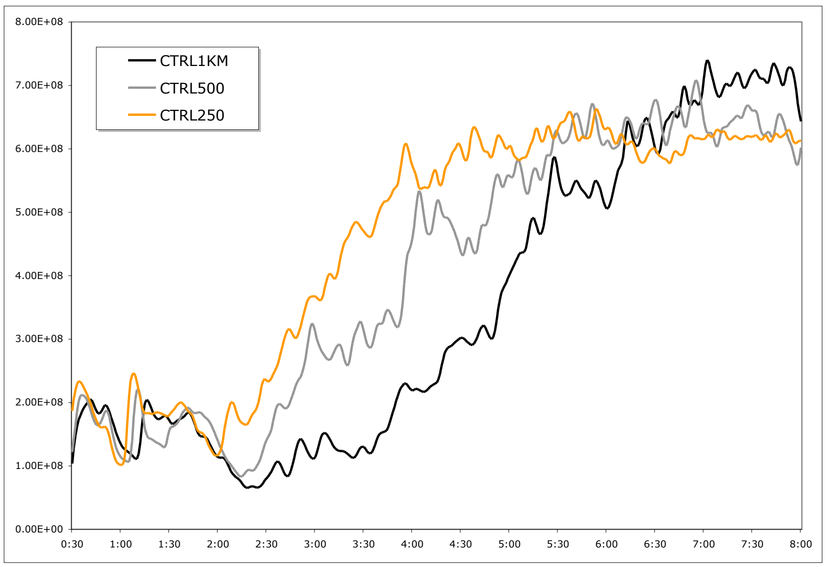

Figure 5.16: Integrated liquid water fraction (kg).

The faster evolution with decreasing grid spacing was evident in the electrification of the systems (Fig. 5.17). Net charge reached a maximum shortly after that of graupel volume. Cloud ice mass, however, continued to increase for at least 2 hours beyond the graupel maximum. Net charge steadily declined with decreasing graupel mass, offset by the increase in cloud ice mass. The relationship between the net charge and graupel mass trend is also shown through graupel-ice non-inductive charging (Fig. 5.18).

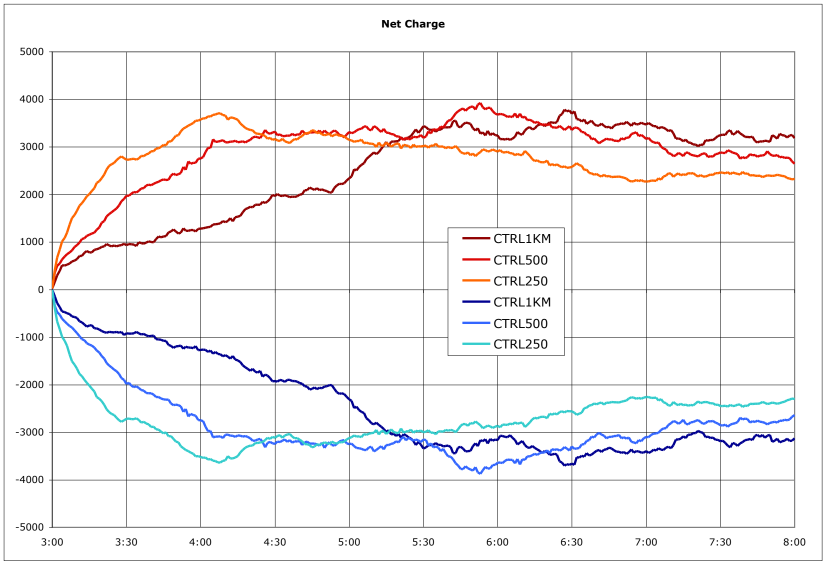

Figure 5.17: Integrated net pos/neg charge for three resolution tests (C).

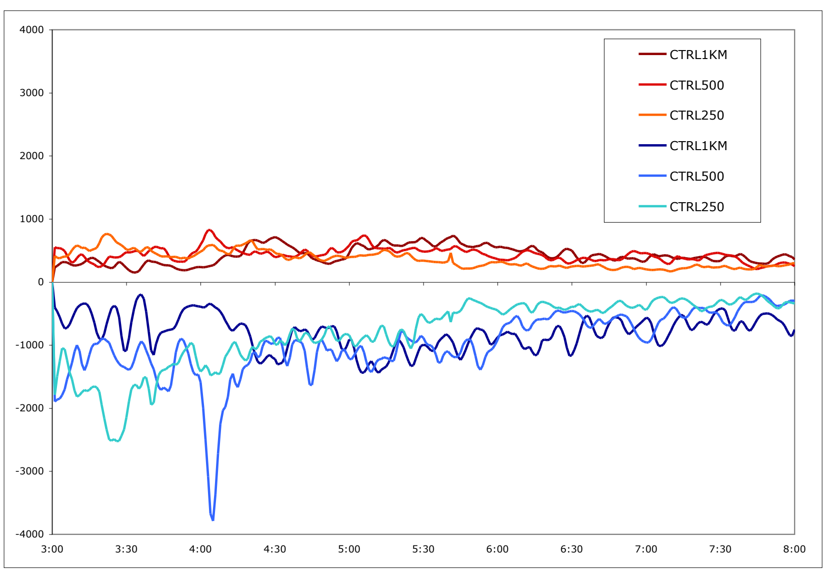

Figure 5.18: Positive (shades of red) and negative (shades of blue) charge separation for graupel-ice non-inductive charging (C).

5.3 Hypotheses verification of charge structure

5.3.1 Charging by a melting mechanism

The laboratory results of Drake (1968) suggest the precipitating particles acquired positive charge, thus releasing negative charge in the process. The current parameterization allows charging of melting graupel and snow through release of large ions. The numerical solutions incorporating this process demonstrate charge can be generated near the melting layer in the stratiform region (Fig. 4.24). However, the charge structure did not conform to what has been observed (Stolzenburg and Marshall 1994; Bateman et al. 1995; Shepherd et al. 1996; Marshall and Stolzenburg 2001; Stolzenburg et al. 2001).

Presented again in Fig. 5.19, weak charge was generated in DRAKE near the melting level once the system was in a mature state. The net charge in this region was on the order of ± 0.1 nC m^{-3}. The charge structure can be attributed to the release of negative ions. Negatively charged ions were present from the 0°C isotherm and lower. Charge density for ions rarely exceeded -0.8 nC m^{-3}.

The negative ion charge was offset by weaker positive charge on wet snow and rain water. A small band of snow carried positive charge on the order of 0.1 nC m^{-3} just below the 0°C isotherm. Below that, rain water carried the positive charge to the surface. The fall speed differential for the snow and rain particles from the low mobility ions allowed for some charge separation to occur. Some negatively charged ions remained near the 0°C isotherm, whereas others attached to precipitation and partially neutralized its charge. The result was an inversion of the observed charge structure, with the negative charge existing after the positive charge precipitated. Thus, the scheme is capable of simulating the negative charge region observed near the melting level. Additionally, the negative charge was associated with ions, which

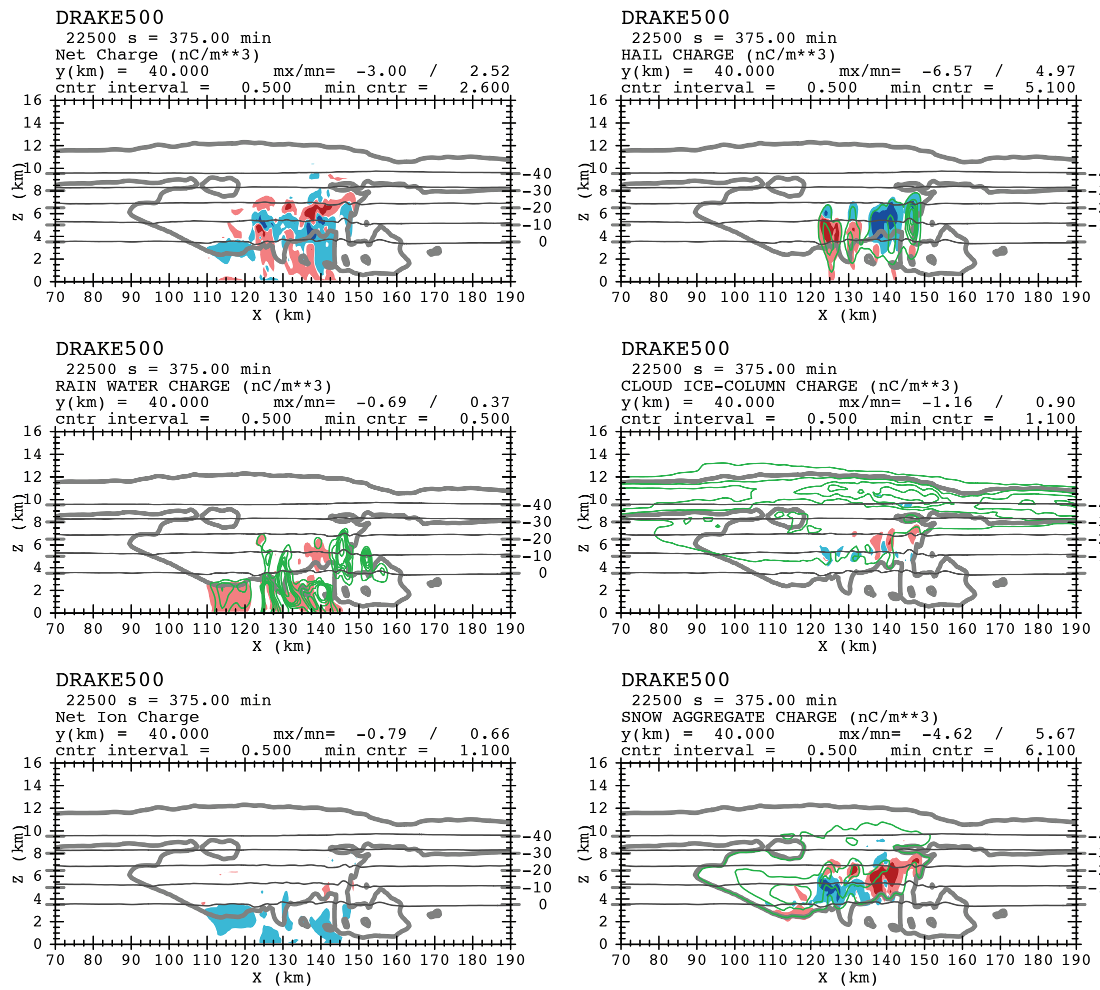

Figure 5.19: Regions of significant charge at 6 hrs 15 mins in the DRAKE case. Charge density (solid contours) in nC m^{-3} for values > 0.1 light red, > 1.0 dark red, < 0.1 light blue, and < 1.0 dark blue. Rain mixing ratio over the range 0-1.0 by 0.2 g/kg, then 1-20 by 1 g/kg. Graupel and snow mixing ratio over the range 0.1-6.1 by 1 g/kg. Ice mixing ratio over the range 0.01 to 1.01 by 0.2. Cloud outline is 0.1 g/kg and temperature by 10°C.

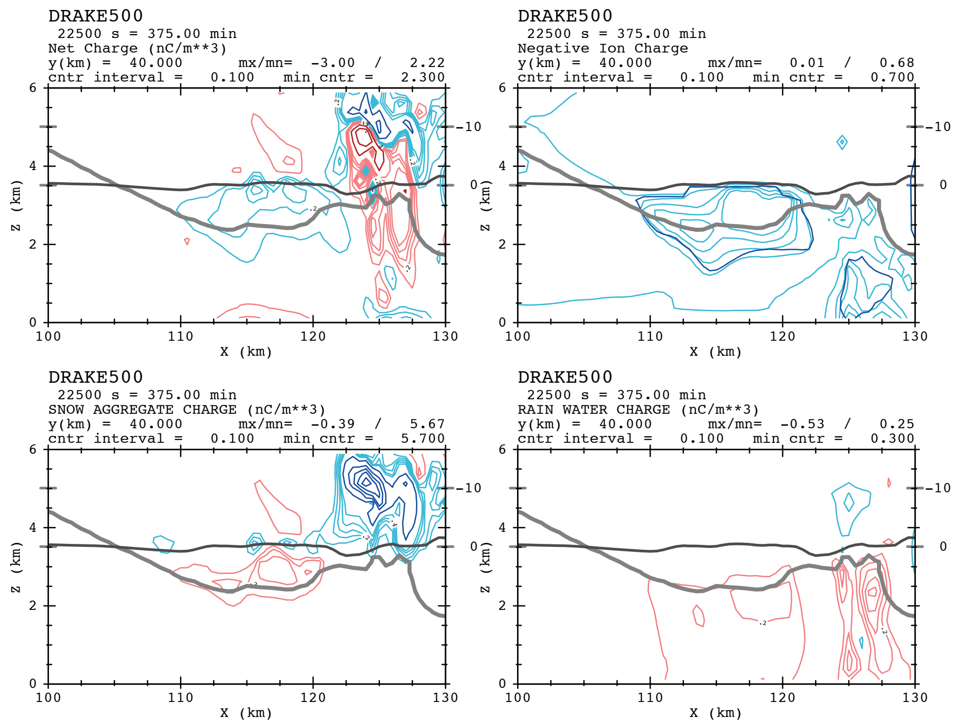

Figure 5.20: Closer look at net charge. Light red/blue lines are ± 0.1-0.5 nC m^{-3} by 0.1, Dark are 1-10 by 1. 0°C isotherm shown and 0.1 g/kg cloud outline. Ions show total negative ion net charge in light blue, and negative large ion net charge > 0.1 nC m^{-3} in dark blue.

is consistent with the suggestion of Bateman et al. (1995) that small particles carry appreciable negative charge.

It should be noted that there were some positive charge regions above the melting level, but with limited breadth. An example is the large area of positive charge in Fig. 5.20 at approximately x = 125 km and a height of 5 km can be attributed to net graupel charge (Fig. 5.19). Though the charge was associated with snow and graupel, it was not a result of the Drake (1968) process, but traditional non-inductive charge separation. Additionally, large ions frequently hit their artificial maximum, with charge then being relegated to small, more mobile ions. This may have affected the charge detail, but not the overall conclusion of an inverted charge structure. Finally, graupel rarely existed in the region above the melting layer. The Drake (1968) mechanism was based on experiments with graupel, but was extended to snow to apply the method.

5.3.2 Charging by water vapor deposition on snow

The results of Sec. 4.1.1 demonstrated the inclusion of a charging mechanism through vapor deposition on snow cannot single-handedly explain observed charge separation near the melting level of the stratiform region. While small amounts of charge were separated, at no time in the DONGHALLETT simulation did significant charge separation occur in the stratiform region through this process. Instead, the mechanism worked to amplify collisional non-inductive charge separation processes.

Figure 5.21 shows the representative contribution of Dong and Hallett (1992) to charge separation at the time of analysis in Section 4.3.2. The light blue shading is negative charge acquired by snow, resulting in net positive charge as negative ions were depleted. The mechanism was active in the stratiform region, near the cloud edge. Charge separation rates were minuscule relative to traditional non-inductive charging rates that are active in the convective region. Typical non-inductive charging

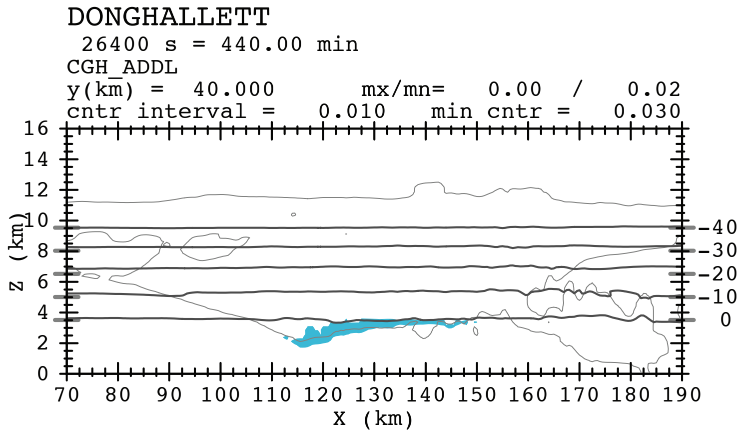

Figure 5.21: Light/dark red fill is >0.001/0.01 nC s^{-1} m^{-3} by 0.1, Light/dark blue fill is <−0.001/0.01 nC s^{-1} m^{-3}. 0°C isotherm shown and 0.1 g/kg cloud outline.

rates for the experiment were on the order of 100 nC s^{-1} m^{-3}, whereas depositional charging was only on the order of 0.001 nC s^{-1} m^{-3}, which was much too weak to generate significant charge density.

5.3.3 Charging by an inductive raindrop collision mechanism

Similar to the snow deposition charging test, raindrop disjection served mainly to amplify charge separation occurring through traditional, collisional non-inductive charging mechanisms. Isolating the effects of the mechanism, charge separation occurred near the melting layer of the stratiform region (Fig. 5.22). The figure coincides with the analysis time of Section 4.3.3, a time when the vertical electric field component resulted in the mechanism charging rain positively. However, the mechanism was capable of separating both polarities near the melting level at other stages (Fig. 5.24). Though charge separation occurred, the mechanism was ineffective and charge separation rates were on the order of 0.001 nC s^{-1} m^{-3}.

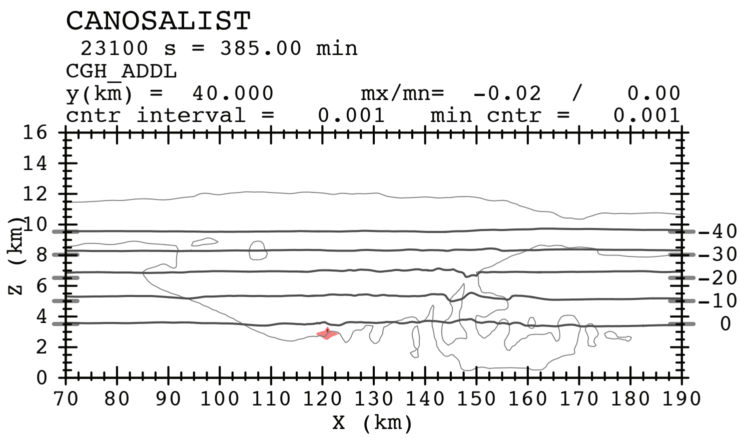

Figure 5.22: Light/dark red fill is >0.001/0.01 nC s^{-1} m^{-3} by 0.1, Light/dark blue fill is <−0.001/0.01 nC s^{-1} m^{-3}. 0°C isotherm shown and 0.1 g/kg cloud outline.

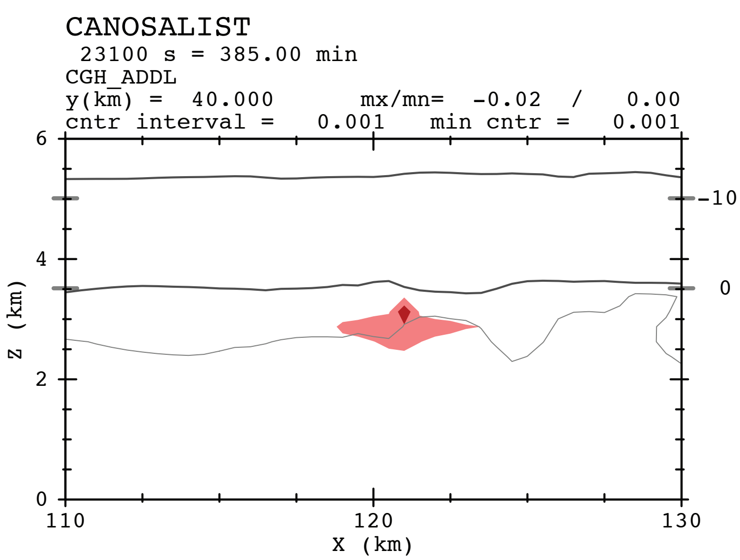

Figure 5.23: As in Fig. 5.22, but with more detail near the region the mechanism is active.

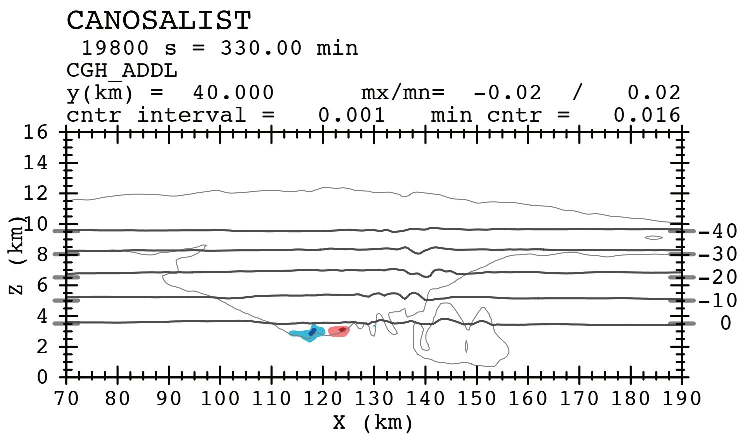

Figure 5.24: Light/dark red fill is >0.001/0.01 nC s^{-1} m^{-3} by 0.1, Light/dark blue fill is <−0.001/0.01 nC s^{-1} m^{-3}. 0°C isotherm shown and 0.1 g/kg cloud outline.

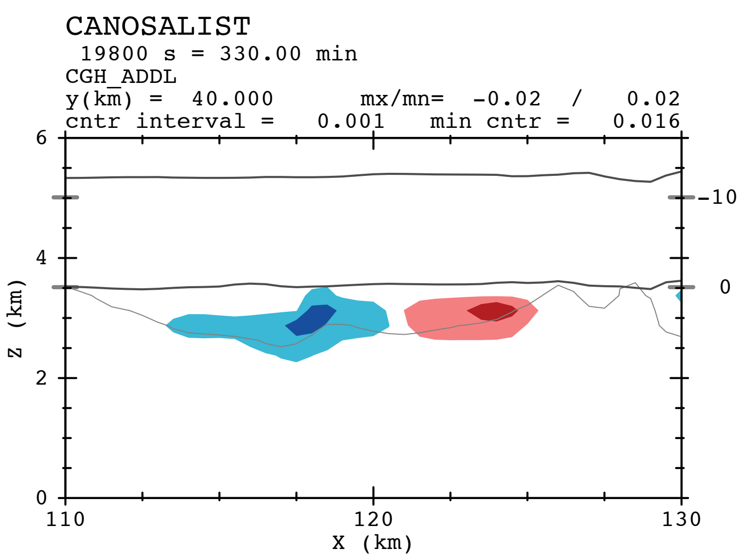

Figure 5.25: As in Fig. 5.22, but with more detail near the region the mechanism is active.

5.3.4 Charging by non-inductive mechanism without liquid water

Although minimal in this experiment, charging without liquid water can affect the regions where frozen cloud particles collide in absence of water (Fig. 5.26). For the analysis time, the figure clearly demonstrates the process was actively charging graupel on the edge of the updraft, where the air was supersaturated with respect to ice and no liquid water was present.

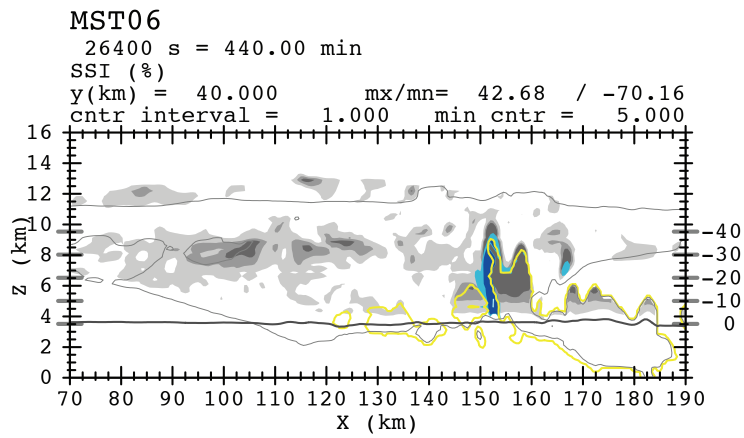

Figure 5.26: Light/dark blue fill is $<-0.5/1.0$ nC s^{-1} m^{-3}. Isotherm shown is 0°C and 0.1 g/kg cloud outline. Supersaturation 5-15% by 5% in dark shading, liquid water >0.01 g/kg in yellow

Although the mechanism did not produce significant charge in the melting layer, it was the largest contributor of the "alternative" mechanisms tested. Occasionally the mechanism was active nearer the stratiform region, but never sustained nor widespread. Charging densities exceeded 3 nC m^{-3}, often contributing as much charge separation as traditional inductive charging parameterizations.

Chapter 6

Conclusions

Large in scope, a number of conclusions can be drawn from this research. The research analyzed the effect of adding mixed-phase particles to the microphysical scheme (Ferrier 1994), the results of high-resolution simulations, and tested hypotheses regarding melting level charge separation (Drake 1968; Dong and Hallett 1992; Canosa and List 1993; Mitzeva et al. 2006b). The Resolution Group test results demonstrated the same conclusions of Bryan et al. (2003), that turbulent motions are better resolved with finer grid spacing. From those tests, it was determined 500 m horizontal grid spacing resolved enough convective motion to be adequate for the additional experiments.

In the Parameterization Group, the improvement of the model to include mixed-phase particles altered the microphysical structure of a LLTS type storm. Specifically, by using mixed-phase particles the system contained more numerous, larger graupel. Additionally, more cloud ice was formed as a result of larger updrafts. The inclusion of mixed-phase particles also slowed storm maturation.

In terms of charge structure, the inclusion of mixed-phase particles led to more charge separation. The increase in net charge was related to the increase in frozen particle production. The simulated 3-dimensional charge advection did not explain observed charge structure in the stratiform region, but was consistent with the sloping charge layer observations through the transition zone (Dotzek et al. 2005; Carey et al.

2005; Ely et al. 2008). Furthermore, substantially increased ice concentration through a parameterized Willis and Heymsfield (1989) process near the melting level remained inadequate, and did not result in significant charge separation.

Current "alternative" charging mechanisms tested in the Hypothesis Group were found to only partially explain the charge structure near the melting level of the stratiform region of a simulated LLTS system. The inclusion of a parameterized Drake (1968) process partially simulated the stratiform charge structure with appreciable negative charge near the melting level. The negative charge was associated with small particles, as suggested by Bateman et al. (1995). Neither the Dong and Hallett (1992) nor Canosa and List (1993) process separated enough charge to produce significant charge densities, with both nearly 2-3 orders of magnitude less than observation. Although not in the stratiform region, non-inductive charging without liquid water as in Mitzeva et al. (2006b) separated the most charge of the alternative mechanisms.

As the Drake (1968) parameterization was able to partially produce the charge structure near the melting level, additional research could be completed to combine the effects of one or more of the alternative mechanisms proposed, which were only tested here in isolation. In particular, as an inductive process, Canosa and List (1993) may have separated more charge with the preexisting field created by the Drake (1968) mechanism. Additionally, more thorough sensitivity experiments could be performed for the non-inductive, alternative mechanisms. Larger, less conservative values of charge separation from Mitzeva et al. (2006b) could be explored as applied to an MCS and in conjunction with the Drake (1968) mechanism. Moreover, the parameterizations for Drake (1968) and Dong and Hallett (1992) could be further developed to include additional environmental dependencies to test the efficacy of the charging mechanism. The parameterizations for this study were chosen to be consistent with previous research, but could be expanded upon in future research as described.

Bibliography

Aufdermaur, A. N. and D. A. Johnson, 1972: Charge separation due to riming in an electric field. *Quart. J. Roy. Meteor. Soc.*, **98**, 369–382.

Baker, B., M. B. Baker, E. R. Jayaratne, J. Latham, and C. P. R. Saunders, 1987: The influence of diffusional growth rates on the charge transfer accompanying rebounding collisions between ice crystals and soft hailstones. *Quart. J. Roy. Meteor. Soc.*, **113**, 1193–1215.

Bateman, M. G., W. D. Rust, B. F. Smull, and T. C. Marshall, 1995: Precipitation charge and size measurements in the stratiform region of two mesoscale convective systems. *J. Geophys. Res.*, **100**, 16341–16356.

Berry, E. X. and R. L. Reinhardt, 1974: An analysis of cloud drop growth by collection: Part II. Single initial distributions. *J. Atmos. Sci.*, **24**, 1825–1831.

Bigg, E. K., 1953: The supercooling of water. *Proc. Phys. Soc. London*, **B66**, 688–694.

Biggerstaff, M. I. and R. A. Houze, 1991: Kinematic and precipitation structure of the 10-11 june 1985 squall line. *Mon. Wea. Rev.*, **119**, 3034–3065.

Brooks, I. M. and C. P. R. Saunders, 1994: An experimental investigation of the inductive mechanism of thunderstorm electrification. *J. Geophys. Res.*, **99**, 10627–10632.

Brooks, I. M., C. P. R. Saunders, R. P. Mitzeva, and S. L. Peck, 1997: The effect on thunderstorm charging of the rate of rime accretion by graupel. *Atmos. Res.*, **43**, 277–295.

Bryan, G. H., J. C. Wyngaard, and J. M. Fritsch, 2003: Resolution requirements for the simulation of deep moist convection. *Mon. Wea. Rev.*, **131**, 2394–2416.

Canosa, E. F. and R. List, 1993: Measurements of inductive charges during drop breakup in horizontal electric fields. *J. Geophys. Res.*, **98**, 2619–2626.

Carey, L. D., M. J. Murphy, T. L. McCormick, and N. W. S. Demetriades, 2005: Lightning location relative to storm structure in a leading-line, trailing-stratiform mesoscale convective system. *J. Geophys. Res.*, **110**.

Chiu, C.-S., 1978: Numerical study of cloud electrification in an axisymmetric, time-dependent cloud model. *J. Geophys. Res.*, **81**, 5025–5049.

Cunning, J. B., 1986: The oklahoma–kansas preliminary regional experiment for storm- central. *Bull. Amer. Meteor. Soc.*, **67**, 1478–1486.

Davis, C., N. Atkins, D. Bartels, L. Bosart, M. Coniglio, G. Bryan, W. Cotton, D. Dowell, B. Jewett, R. Johns, D. Jorgensen, J. Knievel, K. Knupp, W.-C. Lee, G. McFarquhar, J. Moore, R. Przybylinski, R. Rauber, B. Smull, R. Trapp, S. Trier, R. Wakimoto, M. Weisman, and C. Ziegler, 2004: The bow echo and mcv experiment. *Bull. Amer. Meteor. Soc.*, 1075–1093.

Deardorff, J. W., 1980: Stratocumulus-capped mixed layers derived from a three-dimensional model. *Bound.-Layer Meteor.*, **18**, 495–527.

Dendy, J. E., Jr., 1982: Black box multigrid. *J. Comput. Phys.*, **48**, 366–386.

Dong, Y. and J. Hallett, 1992: Charge separation by ice and water drops during growth and evaporation. *J. Geophys. Res.*, **97**, 20361–20371.

Dotzek, N., R. M. Rabin, L. D. Carey, D. R. MacGorman, T. L. McCormick, N. W. S. Demetriades, M. J. Murphy, and R. L. Holle, 2005: Lightning activity related to satellite and radar observations of a mesoscale convective system over texas on 7-8 april 2002. *Atmos. Res.*, **76**, 127–166.

Drake, J. C., 1968: Electrification accompanying the melting of ice particles. *Quart. J. Roy. Meteor. Soc.*, **94**, 176–191.

Ely, B. L., R. E. Orville, L. D. Carey, and C. L. Hodapp, 2008: Evolution of the total lightning structure in a leading-line, trailing stratiform mesoscale convective system over houston, texas. *J. Geophys. Res.*, **113**.

Ferrier, B. S., 1994: A double-moment multiple-phase four-class bulk ice scheme. Part I: Description. *J. Atmos. Sci.*, **51**, 249–280.

Fovell, R. G. and Y. Ogura, 1988: Numerical simulation of a midlatitude squall line in two dimensions. *J. Atmos. Sci.*, **45**, 3846–3879.

Fritsch, J. M., R. J. Kane, and C. R. Chelius, 1986: The contribution of mesoscale convetive weather systems to the warm-season precipitation in the united states. *J. Climate Appl. Meteor.*, **25**, 1333–1345.

Gaskell, W., 1981: A laboratory study of the inductive theory of thunderstorm electrification. *Quart. J. Roy. Meteor. Soc.*, **107**, 955–966.

Goodman, S. J. and D. R. MacGorman, 1986: Cloud-to-ground lightning activity in mesoscale convective complexes. *Mon. Wea. Rev.*, **114**, 2320–2328.

Gunn, R. and G. D. Kinzer, 1949: The terminal velocity of fall for water droplets in stagnant air. *J. Meteor.*, **6**, 243–248.

Helsdon, J. H., Jr., 1980: Chaff seeding effects in a dynamical-electrical cloud model. *J. Appl. Met.*, **19**, 1101–1125.

Helsdon, J. H., Jr. and R. D. Farley, 1987: A numerical modeling study of a Montana thunderstorm: 2. Model results versus observations involving electrical aspects. *J. Geophys. Res.*, **92**, 5661–5675.

Helsdon, J. H., Jr., G. Wu, and R. D. Farley, 1992: An intracloud lightning parameterization scheme for a storm electrification model. *J. Geophys. Res.*, **97**, 5865–5884.

Hodapp, C. L., L. D. Carey, and R. E. Orville, 2008: Evolution of radar reflectivity and total lightning characteristics of the 21 april 2006 mesoscale convective system over texas. *Atmos. Res.*, **89**, 113–137.

Houze, R. A., S. A. Rutledge, M. I. Biggerstaff, and B. F. Smull, 1989: Interpretation of doppler weather radar displays of midlatitude mesoscale convective systems. *Bull. Amer. Meteor. Soc.*, **70**, 608–619.

Hunter, S. M., T. J. Schuur, T. C. Marshall, and W. D. Rust, 1992: Electric and kinematic structure of the oklahoma mesoscale convective system of 7 june 1989. *Mon. Wea. Rev.*, **120**, 2226–2239.

Jayaratne, E. R., C. P. R. Saunders, and J. Hallett, 1983: Laboratory studies of the charging of soft hail during ice crystal interactions. *Quart. J. Roy. Meteor. Soc.*, **109**, 609–630.

Jorgensen, D. P. and B. F. Smull, 1993: Mesovortex circulations seen by airborne doppler radar within a bow-echo mesoscale convective system. *Bull. Amer. Meteor. Soc.*, **74**, 2146–2157.

Klemp, J. B. and R. B. Wilhelmson, 1978: The simulations of three-dimensional convective storm dynamics. *J. Atmos. Sci.*, **35**, 1070–1096.

Lang, T. J. and S. A. Rutledge, 2008: Kinematic, microphysical, and electrical aspects of an asymmetric bow-echo mesoscale convective system observed during steps 2000. *J. Geophys. Res.*, **113**.

Lang, T. J., S. A. Rutledge, and K. C. Wiens, 2004: Origins of positive cloud-to-ground lightning flashes in the stratiform region of a mesoscale convective system. *Geophys. Res. Lett.*, **31**, L10105, doi:10.1029/2004GL019823.

Leary, C. A. and R. A. Houze, 1979: Melting and evaporation of hydrometeors in precipitation from the anvil clouds of deep tropical convection. *J. Atmos. Sci.*, **36**, 669–679.

Lo, K. K. and R. E. Passarelli, 1982: The growth of snow in winter storms: An airborne observational study. *J. Atmos. Sci.*, **39**, 697–706.

Lyons, W. A., M. Uliasz, and T. E. Nelson, 1998: Large peak current cloud-to-ground lightning flashes during the summer months in the contiguous united states. *Mon. Wea. Rev.*, **126**, 2217–2233.

MacGorman, D. R. and W. D. Rust, 1998: *The Electrical Nature of Storms*. Oxford Univ. Press, New York, 422 pp.

MacGorman, D. R., J. M. Straka, and C. L. Ziegler, 2001: A lightning parameterization for numerical cloud models. *J. Appl. Meteor.*, **40**, 459–478.

Mansell, E. R., D. R. MacGorman, C. L. Ziegler, and J. M. Straka, 2002: Simulated three-dimensional branched lightning in a numerical thunderstorm model. *J. Geophys. Res.*, **107**.

— 2005: Charge structure and lightning sensitivity in a simulated multicell thunderstorm. *J. Geophys. Res.*, **110**.

Mansell, E. R., C. L. Ziegler, and E. C. Bruning, 2010: Simulated electrification of a small thunderstorm with two-moment bulk microphysics. *J. Atmos. Sci.*, **67**, 171–194.

Marshall, T. C. and W. D. Rust, 1993: Two types of vertical electrical structures in stratiform precipitation regions of mesoscale convective systems. *Bull. Amer. Meteor. Soc.*, **74**, 2159–2170.

Marshall, T. C. and M. Stolzenburg, 2001: Voltages inside and just above thunderstorms. *J. Geophys. Res.*, **106**, 4757–4768.

Mason, B. L. and J. G. Dash, 2000: Charge and mass transfer in ice-ice collisions: Experimental observations of a mechanism in thunderstorm electrification. *J. Geophys. Res.*, **105**, 10185–10192.

Meyers, M. P., P. J. DeMott, and W. R. Cotton, 1992: New primary ice-nucleation parameterizations in an explicit cloud model. *J. Appl. Meteor.*, **31**, 708–721.

Mitzeva, R. P., J. Latham, and S. Petrova, 2006a: A comparative modeling study of the early electrical development of maritime and continental thunderstorms. *Atmos. Res.*, **82**, 26–36.

Mitzeva, R. P., C. P. R. Saunders, and B. Tsenova, 2006b: Parameterisation of non-inductive charging in thunderstorm regions free of cloud droplets. *Atmos. Res.*, **82**, 102–111.

Moulton, J. D., J. E. Dendy, Jr., and J. E. Hyman, 1998: The black box multigrid numerical homogenization algorithm. *J. Comput. Phys.*, **142**, 80–108.

Ogura, Y. and M.-T. Liou, 1980: The structure of a midlatitude squall line: A case study. *J. Atmos. Sci.*, **37**, 553–567.

Orville, R. E., R. W. Henderson, and L. F. Bosart, 1988: Bipole patterns revealed by lightning locations in mesoscale storm systems. *Geophys. Res. Lett.*, **15**, 129–132.

Parker, M. D. and R. H. Johnson, 2000: Organizational modes of midlatitude mesoscale convective systems. *Mon. Wea. Rev.*, **128**, 3413–3436.

Passarelli, R. E., 1978: An approximate analytical model of the vapor deposition and aggregation growth of snowflakes. *J. Atmos. Sci.*, **35**, 118–124.

Rasmussen, R. M. and A. J. Heymsfield, 1987: Melting and shedding of graupel and hail. part ii: Sensitivity study. *J. Atmos. Sci.*, **44**, 2764–2782.

Rawlins, F., 1982: A numerical study of thunderstorm electrification using a three dimensional model incorporating the ice phase. *Quart. J. Roy. Meteor. Soc.*, **108**, 779–800.

Reynolds, S. E., M. Brook, and M. F. Gourley, 1957: Thunderstorm charge separation. *J. Meteor.*, **14**, 426–436.

Rotunno, R., J. B. Klemp, and M. L. Weisman, 1988: A theory for strong, long-lived squall lines. *J. Atmos. Sci.*, **47**, 3067–3077.

Rutledge, S. A. and R. A. Houze, 1987: A diagnostic modeling study of the trailing stratiform region of a midlatitude squall line. *J. Atmos. Sci.*, **44**, 2640–2656.

Rutledge, S. A., C. Lu, and D. R. MacGorman, 1990: Positive cloud-to-ground lightning in mesoscale convective systems. *J. Atmos. Sci.*, **47**, 2085–2100.

Rutledge, S. A. and D. R. MacGorman, 1988: Cloud-to-ground lightning activity in the 10–11 June 1985 mesoscale convective system observed during OK PRE-STORM. *Mon. Wea. Rev.*, **116**, 1393–1408.

Rutledge, S. A., J. R. A. Houze, M. I. Biggerstaff, and T. Matejka, 1988: The Oklahoma-Kansas mesoscale convective system of 10-11 June 1985: Precipitation structure and single-doppler radar analysis. *Mon. Wea. Rev.*, **116**, 1409–1430.

Saunders, C. P. R., H. Bax-Norman, C. Emersic, E. E. Avila, and N. E. Castellano, 2006: Laboratory studies of the effect of cloud conditions on graupel/crystal charge transfer in thunderstorm electrification. *Quart. J. Roy. Meteor. Soc.*, **132**.

Saunders, C. P. R., W. D. Keith, and R. P. Mitzeva, 1991: The effect of liquid water on thunderstorm charging. *J. Geophys. Res.*, **96**, 11007–11017.

Saunders, C. P. R. and S. L. Peck, 1998: Laboratory studies of the influence of the rime accretion rate on charge transfer during crystal/graupel collisions. *J. Geophys. Res.*, **103**, 13949–13956.

Saunders, C. P. R., S. L. Peck, G. G. A. Varela, E. E. Avila, and N. E. Castellano, 2001: A laboratory study of the influence of water vapour and mixing on the charge transfer process during collisions between ice crystals and graupel. *Atmos. Res.*, **58**, 187–203.

Schuur, T. J. and S. A. Rutledge, 2000a: Electrification of stratiform regions in mesoscale convective systems. Part I: An observational comparison of symmetric and asymmetric MCSs. *J. Atmos. Sci.*, **57**, 1961–1982.

— 2000b: Electrification of stratiform regions in mesoscale convective systems. Part II: Two-dimensional numerical model simulations of a symmetric MCS. *J. Atmos. Sci.*, **57**, 1983–2006.

Schuur, T. J., B. F. Smull, W. D. Rust, and T. C. Marshall, 1991: Electrical and kinematic structure of the stratiform precipitation region trailing an Oklahoma squall line. *J. Atmos. Sci.*, **48**, 825–842.

Seifert, A. and K. D. Beheng, 2006: A two-moment cloud microphysics parameterization for mixed-phase clouds. Part 1: Model description. *Met. Atmos. Phys.*, **92**, 45–66.

Sentman, D. D., E. M. Wescott, D. L. Osborne, D. L. Hampton, and M. J. Heavner, 1995: Preliminary results from the Sprites94 aircraft campaign: 1. Red Sprites. *Geophys. Res. Lett.*, **22**, 1205–1208.

Shepherd, T. R., W. D. Rust, and T. C. Marshall, 1996: Electric fields and charges near 0°C in stratiform clouds. *Mon. Wea. Rev.*, **124**, 919–938.

Skamarock, W. C., M. L. Weisman, and J. B. Klemp, 1994: Three-dimensional evolution of simulated long-lived squall lines. *J. Atmos. Sci.*, **51**, 2563–2584.

Smull, B. F. and R. A. Houze, 1985: A midlatitude squall line with a trailing region of stratiform rain: Radar and satellite observations. *Mon. Wea. Rev.*, **113**, 117–133.

— 1987a: Dual-doppler radar analysis of a midlatitude squall line with a trailing region of stratiform rain. *J. Atmos. Sci.*, **44**, 2128–2148.

— 1987b: Rear inflow in squall lines with trailing stratiform precipitation. *Mon. Wea. Rev.*, **115**, 2869–2889.

Stolzenburg, M. and T. C. Marshall, 1994: Testing models of thunderstorm charge distribution with Coulomb's law. *J. Geophys. Res.*, **99**, 25921–25932.

Stolzenburg, M., T. C. Marshall, and W. D. Rust, 2001: Serial soundings of electric field through a mesoscale convective system. *J. Geophys. Res.*, **106**, 12371–12380.

Stolzenburg, M., T. C. Marshall, W. D. Rust, and B. F. Smull, 1994: Horizontal distribution of electrical and meteorological conditions across the stratiform region of a mesoscale convective system. *Mon. Wea. Rev.*, **122**, 1777–1797.

Stolzenburg, M., W. D. Rust, and T. C. Marshall, 1998: Electrical structure in thunderstorm convective regions 3. Synthesis. *J. Geophys. Res.*, **103**, 14097–14108.

Straka, J. M. and E. R. Mansell, 2005: A bulk microphysics parameterization with multiple ice precipitation categories. *J. Appl. Meteor.*, **44**, 445–466.

Takahashi, T., 1974: Numerical simulation of warm cloud electricity. *J. Atmos. Sci.*, **31**, 2160–2181.

— 1978: Riming electrification as a charge generation mechanism in thunderstorms. *J. Atmos. Sci.*, **35**, 1536–1548.

— 1979: Warm cloud electricity in a shallow axisymmetric cloud model. *J. Atmos. Sci.*, **36**, 2236–2258.

— 1984: Thunderstorm electrification – a numerical study. *J. Atmos. Sci.*, **41**, 2541–2558.

— 1987: Determination of lightning origins in a thunderstorm model. *J. Meteor. Soc. Japan*, **65**, 777–794.

Thorpe, A. J., M. J. Miller, and M. W. Moncrieff, 1982: Two-dimensional convection in non-constant shear: a model of mid-latitude squall lines. *Quart. J. Roy. Meteor. Soc.*, **108**, 739–762.

Weisman, M. L. and J. B. Klemp, 1982: The dependence of numerically simulated convective storms on vertical wind shear and buoyancy. *Mon. Wea. Rev.*, **110**, 504–520.

Wicker, L. J. and W. C. Skamarock, 2002: Time-splitting methods for elastic models using forward time schemes. *Mon. Wea. Rev.*, **130**, 2088–2097.

Wicker, L. J. and R. B. Wilhelmson, 1995: Simulation and analysis of tornado development and decay within a three-dimensional supercell thunderstorm. *J. Atmos. Sci.*, **52**, 2675–2703.

Williams, E. R., 1989: The tripole structure of thunderstorms. *J. Geophys. Res.*, **94**, 13151–13167.

Willis, P. T. and A. J. Heymsfield, 1989: Structure of the melting layer in mesoscale convective system stratiform precipitation. *J. Atmos. Sci.*, **46**, 2008–2025.

Wisner, C., H. D. Orville, and C. Meyers, 1972: A numerical model of a hail-bearing cloud. *J. Atmos. Sci.*, **29**, 1160–1181.

Ziegler, C. L., 1985: Retrieval of thermal and microphysical variables in observed convective storms. Part I: Model development and preliminary testing. *J. Atmos. Sci.*, **42**, 1487–1509.

Ziegler, C. L. and D. R. MacGorman, 1994: Observed lightning morphology relative to modeled space charge and electric field distributions in a tornadic storm. *J. Atmos. Sci.*, **51**, 833–851.

Ziegler, C. L., D. R. MacGorman, J. E. Dye, and P. S. Ray, 1991: A model evaluation of non-inductive graupel-ice charging in the early electrification of a mountain thunderstorm. *J. Geophys. Res.*, **96**, 12833–12855.

Ziegler, C. L., P. S. Ray, and D. R. MacGorman, 1986: Relations of kinematics, microphysics and electrification in an isolated mountain thunderstorm. *J. Atmos. Sci.*, **43**, 2098–2114.

Zrnić, D. S., N. Balakrishnan, C. L. Ziegler, V. N. Bringi, K. Aydin, and T. Matejka, 1993: Polarimetric signatures in the stratiform region of a mesoscale convective system. *J. Appl. Meteor.*, **32**, 678–693.

Appendix A

Errata

A.1 Model Errors

Nearing completion of this work, two model errors were discovered that had an effect on the solutions when using mixed-phase particles. The first (PFRZ) was an error that affected the microphysical solutions, and consequently the electrical solutions. The impact was minimal and did not change the overall conclusions. Corrected results were used in the analysis of the Parameterization Group as changes in microphysical behavior were being scrutinized. The Resolution and Hypotheses groups contain the error, but were not corrected because the Resolution experiments were too computationally expensive to recreate and the Hypotheses experiments strictly test electrical parameterizations.

The error incorrectly double counted select latent heat terms when mixed phase solutions were used. The model accounts for latent heat derived by melting, freezing, and accretion. With the inclusion of partial melting or freezing, heat from several of those processes was also accounted for within the partial melting and freezing integration. Several of the terms failed to be omitted in the final latent heat calculation, thus were double-counted. Enough variation was identified to necessitate re-running the simulations for microphysical evaluation.

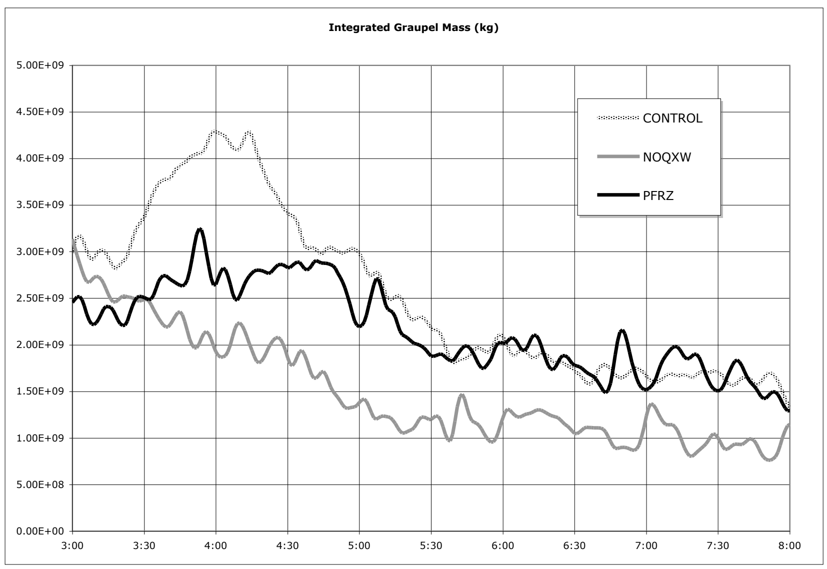

Figure A.1: Time series of domain integrated graupel mass in kg for the initial CONTROL simulation, the corrected PFRZ simulation, and the simulation without mixed-phase particles, NOQXW.

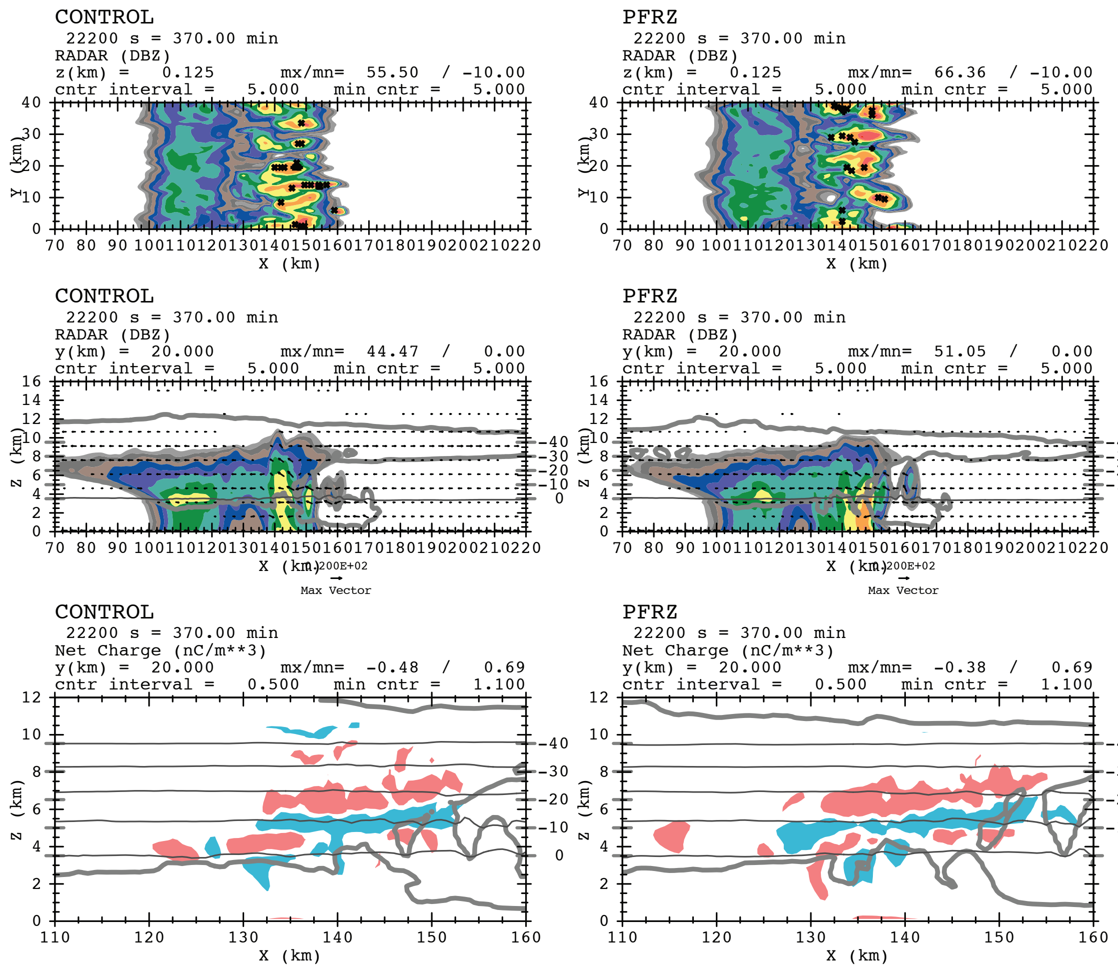

Figure A.2: Representative fields for the initial CONTROL simulation and the corrected PFRZ simulation. From left to right: Inferred surface reflectivity with ±CG, inferred reflectivity with 0.1 g/kg cloud outline and wind vectors, charge density (solid contours) in nC m^{-3} for values > 0.1 light red, > 1.0 dark red, < 0.1 light blue, and < 1.0 dark blue. Note the change in axes for the charge density panel to show more detail.

The second error (CTRLQRFIX3) did not affect the microphysical solutions, only electrification. The error was the result of reassigning charge from snow or graupel when it melts to rain. Initially, the term tracking the charge transfer for rain was erroneously set to zero. However, a compensating term tracking the melt water mass prior to shedding was erroneously added to rain charge, and approximately balanced the loss of the shed rain charge.

The model was corrected and the control experiment was re-run for comparison. The results were not significantly different, and did not affect the conclusions derived from the simulation containing the error. To further obviate the need to re-run all simulations, two additional experiments were performed with $\pm 0.5°C$ thermal variation to demonstrate consistency with the conclusions.

Appendix B

Model Details

B.1 Model Details

The microphysical model was originally developed by Ziegler (1985) for six species of mass, of which a subset included number concentration prediction. The model was updated by Mansell et al. (2010) to include CCN prediction and bulk graupel density as in Straka and Mansell (2005). That foundation is described below.

To begin, the underlying particle distributions were given in terms of a gamma function as

$$n(v) = A_n \frac{v^{\nu}}{\bar{v}^{\nu+1}} \exp[-B_n(\frac{v}{\bar{v}})^{\mu}] \tag{B.1}$$

where

$$A_n = \frac{\mu N_t}{\Gamma(\frac{\nu+1}{\mu})} B_n^{(\nu+1)/\mu} \tag{B.2}$$

and

$$B_n = \left[\frac{\Gamma(\frac{\nu+1}{\mu})}{\Gamma(\frac{\nu+2}{\mu})}\right]^{-\mu}. \tag{B.3}$$

The prognostic equations for mixing ratio of each microphysical scalar were given by:

$$\frac{dQ_v}{dt} = -QRCEV - QSCEV - QHCEV - QSSBV - QHSBV \\ - \delta(QIINT + QISBV + QHDPV + QSDPV + QIDPV), \tag{B.4}$$

$$\frac{dQ_w}{dt} = -QRACW - QSACW - QRCNW - QHACW \\ - \delta(QIACW + QWFRZC + QWCTFZC + QICICHR), \tag{B.5}$$

$$\begin{aligned} \frac{dQ_r}{dt} = QRACW + QRCNW + QRCEV - QSSHR - QHSHR \\ - (1-\delta)(QHMLR + QSMLR + QIMLR) \\ - \delta(QIACR + QRFRZ) - QHACR, \end{aligned} \tag{B.6}$$

$$\begin{aligned} \frac{dQ_i}{dt} = QSMUL + QHMUL1 + \delta(QIINT + QIDPV + QIACW \\ + QWFRZC + QWCTFZC + QICICHR) \\ - \delta(QSCNI + QRACI + QSACI) \\ + QHACI + \delta QISBV + (1-\delta)QIMLR - QHCNI, \end{aligned} \tag{B.7}$$

$$\begin{aligned} \frac{dQ_s}{dt} = -QHACS - QHCNS + \delta(QSCNI + QSACI + QSDPV) \\ + (1-\delta)QSMLR + QSSHR + QSSBV - QSMUL, \end{aligned} \tag{B.8}$$

$$\begin{aligned} \frac{dQ_{sw}}{dt} = -QSACW + QSCEV - QSMLR + QSSHR \\ - QSFZS - F_{sw}QHACS - \delta F_{sw}QHCNS, \end{aligned} \tag{B.9}$$

$$
\begin{aligned}
\frac{dQ_h}{dt} = QHCEV + QHACR + QHACW + QHACS + QHACI \\
+ QHCNS + QHCNI + QHSHR + (1-\delta)QHMLR \\
+ \delta(QIACRF + QRFRZ + QRACIF + QHDPV) \\
- QHSBV - QHCEV - QHMUL1,
\end{aligned}
\tag{B.10}
$$

$$
\begin{aligned}
\frac{dQ_{hw}}{dt} = -QHACW + QHCEV - QHMLR + QHSHR - QHFZH \\
+ \delta QHACR + F_{sw}QHACS + \delta F_{sw}QHCNS,
\end{aligned}
\tag{B.11}
$$

where $\frac{dQ_{sw}}{dt}$ and $\frac{dQ_{hw}}{dt}$ describe the liquid water fraction prediction for snow and graupel, respectively, which was presented in Sec. 3.1. Also, δ was defined by

$$
\delta = \begin{cases} 1 & T < 0°C \\ 0 & T \geq 0°C. \end{cases}
\tag{B.12}
$$

The prognostic equations for the corresponding number concentration solutions were given as follows:

$$
\begin{aligned}
\frac{dN_w}{dt} = -CAUTN - CRACW - CSACW - CHACW \\
- \delta(CIACW + CWFRZC + CWCTFZC),
\end{aligned}
\tag{B.13}
$$

$$
\begin{aligned}
\frac{dN_r}{dt} = CRCNW - (1-\delta)(CHMLR + CSMLR) - CSSHR - CHSHR \\
- \delta(CIACR + CRFRZ) - CHACR + CRCEV - CRACR,
\end{aligned}
\tag{B.14}
$$

$$
\begin{aligned}
\frac{dN_i}{dt} = CHMUL1 + CSMUL \\
+ \delta(CIINT + CWFRZC + CWCTFZC + CICICHR) \\
- \delta(CSCNI + CRACI + CSACI + CHACI \\
+ CHCNI - CISBV) - (1-\delta)CIMLR,
\end{aligned}
\tag{B.15}
$$

$$\frac{dN_s}{dt} = \delta CSCNI - CHACS - CHCNS \\ + (1-\delta)CSMLR + CSSHR + CSSBV - CSACS, \tag{B.16}$$

$$\frac{dN_h}{dt} = CRFRZ + \delta CIACR + CHCNS + CHCNI \\ + (1-\delta)CHMLR + CHSBV. \tag{B.17}$$

B.1.1 Autoconversion

Autoconversion of cloud water to rain water followed Ziegler (1985). The rate of cloud water mass converting to rain as a result of collision-coalescence was given as

$$QRCNW = \frac{L_2}{\rho_0 \tau} \tag{B.18}$$

with corresponding number concentration

$$CRCNW = \frac{3.5{\times}10^9 L_2}{\tau}. \tag{B.19}$$

The rate was controlled by terms L_2, the assumed mass of the droplets, and τ, a time scale. The droplet mass was defined as

$$L_2 = 2.7{\times}10^{-2}[(0.5{\times}10^{20} r_b^3 \bar{D}_w) - 0.4]\rho_w N_w v_w \tag{B.20}$$

for a variance-scaled droplet radius, r_b, given by

$$r_b = \bar{R}_w (1+\nu_w)^{\frac{1}{6}} \tag{B.21}$$

with mean droplet radius $\bar{R}_w$. The time scale also depended on the scaled droplet radius as

$$\tau = \frac{3.7{\times}10^{-6}}{(r_b - 7.5{\times}10^{-6})\rho_0 q_w} \tag{B.22}$$

for $r_b > 7.5{\times}10^{-6}$ m.

For ice larger than 100μm in diameter, but limited to $\frac{1}{2}$, the conversion of ice aggregates to snow was adapted in Mansell et al. (2010) from Ziegler (1985) for two moments as:

$$QSCNI = \frac{\bar{D}_i}{2{\times}10^{-4}} QIDPV \tag{B.23}$$

with number concentration

$$CSCNI = \frac{1}{2}\frac{\rho_0}{\rho_i \bar{v}_i} QSCNI. \tag{B.24}$$

Snow and ice conversion to graupel followed Mansell et al. (2010) as an update of Straka and Mansell (2005) using rime density for each species, $\rho_{x,rime}$:

$$\rho_{x,rime} = c_{r1}\left[\frac{0.3{\times}10^6 D_w |V_x - V_w|}{-T_c}\right]^{c_{r2}}. \tag{B.25}$$

Then, the mass of snow or ice converted to graupel was predicted by the difference between wet growth and depositional growth

$$QHCNX = QXACW - QXDPV \tag{B.26}$$

$$CHCNI = \frac{N_x}{Q_x} QHCNX \tag{B.27}$$

when rime density exceeded 300 kg m^{-3}.

B.1.2 Accretion

For larger droplets, raindrop accretion of cloud water was treated as Ziegler (1985) for mean rain radii of $\bar{R}_r > r_H$ or $N_r > N_H$. The terms r_H and N_H are thresholds originally developed by Berry and Reinhardt (1974) to provide time for condensation and autoconversion to create a sufficient distribution of larger droplets before activating. Once the size or number threshold was exceeded, the rate was given as

$$QRACW = a_2 N_r N_w \frac{\rho_w}{\rho_0}\bar{v}_w\left(\frac{\nu_w + 2}{\nu_w + 1}\bar{v}_w + \bar{v}_r\right) \tag{B.28}$$

$$CRACW = a_2 N_r N_w (\bar{v}_w + \bar{v}_r) \tag{B.29}$$

for R > 50μm. Smaller droplets with R $\leq$ 50μm accreted cloud water at a rate of

$$QRACW = a_1 N_r N_w \frac{\rho_w}{\rho_0} \bar{v}_w \left[\frac{(\nu_w + 3)(\nu_w + 2)}{(\nu_w + 1)^2} \bar{v}_w^2 + \frac{\nu_r + 2}{\nu_r + 1} \bar{v}_r^2 \right] \tag{B.30}$$

$$CRACW = a_1 N_r N_w \left[\frac{\nu_w + 2}{\nu_w + 1} \bar{v}_w^2 + \frac{\nu_r + 2}{\nu_r + 1} \bar{v}_r^2 \right]. \tag{B.31}$$

B.1.3 Collection

Similarly, for temperatures above $-5°$C, rain can collect ice following

$$CRACI = E_{ri} a_2 N_r N_i \left[\frac{\nu_i + 2}{\nu_i + 1} \bar{v}_i + \bar{v}_r \right] \tag{B.32}$$

$$QRACI = \frac{Q_i}{\rho_0} CRACI \tag{B.33}$$

Collection between hydrometeors other than snow was given by the stochastic collection equation developed by Seifert and Beheng (2006), and described in Mansell et al. (2010), for differential fall speed V_{xy} given by

$$\Delta V_{xy} = (V_x - {V_y}^2 + 0.04 V_x V_y)^{\frac{1}{2}}. \tag{B.34}$$

The mass collected was given by

$$QXACY = \frac{\pi}{4} E_{xy} N_x Q_y \Delta V_{xy} (A_x {D_x}^2 + B_{xy} D_x D_y + C_y {D_y}^2), \tag{B.35}$$

where A_x, B_{xy}, and C_y are given in Seifert and Beheng (2006). The change in concentration was thus

$$CXACY = \frac{\rho_0}{\rho_y \bar{v}_y} QXACY. \tag{B.36}$$

Snow interactions were handled separately, using Zrnić et al. (1993). For snow collection of cloud water droplets or cloud ice, the following was used:

$$QSACY = a_2 \epsilon E_{sx} N_s N_y \left[\frac{(\nu_y + 2) v_y}{\nu_y + 1} + v_s \right] \left(\frac{\rho_y \bar{v}_y}{\rho_0} \right) \tag{B.37}$$

$$CSACY = \frac{\rho_0}{\rho_y \bar{v}_y} QSACY. \tag{B.38}$$

Snow self-collection, or aggregation, also followed Zrnić et al. (1993) for number concentration only, as mixing ratio is unchanged for self-collection:

$$CSACS = 601.12\exp(0.05T)N_s^2 q_s. \tag{B.39}$$

Rain self-collection was treated as in Ziegler (1985) for two ranges of droplet radii. The number concentration of rain changed as follows:

$$CRACR = \begin{cases} E_{w0}a_2 N_r^2 v_r & D_r \geq 100\mu m \\ E_{w0}a_1(N_r v_r)^2 \frac{\alpha_r+2}{\alpha_r+1} & D_r < 100\mu m, \end{cases} \tag{B.40}$$

where

$$E_{w0} = \begin{cases} 1 & D_r < 6.1{\times}10^{-4} \\ \exp[-50(50D_r - 6{\times}10^{-4})] & 6.1{\times}10^{-4} \leq D_r \geq 2{\times}10^{-3} \\ 0 & D_r > 2{\times}10^{-3}. \end{cases} \tag{B.41}$$

B.1.4 Raindrop Freezing

Raindrop freezing into graupel is treated as in Ziegler (1985), based on the Wisner et al. (1972) parameterization of Bigg (1953). First, the number of drops that freeze was predicted, then the mass of those drops as:

$$CRFRZ = B'N_r\bar{v}_r[\exp(A'T_c) - 1]QRFRZ = \frac{\nu_r+2}{\nu_r+1}\frac{\rho_r}{\rho_0}CRFRZ \tag{B.42}$$

where A′=0.66 and B′=100, according to Bigg (1953).

B.1.5 Ice Initiation

Heterogeneous freezing of drops as ice crystals are collected used the rain fall speed formula derived by Gunn and Kinzer (1949). The rate of change for mass and concentration were thus given as

$$\begin{aligned} QIACR = \left(\frac{\rho_r}{\rho_0}\right) 0.2172[0.5223\bar{D}_r^5 + 49711\bar{D}_r^6 - 1.673{\times}10^7\bar{D}_r^7 \\ + 2.404{\times}10^9\bar{D}_r^8 - 1.229{\times}10^{11}\bar{D}_r^9]N_i N_r f_i f_r \end{aligned} \tag{B.43}$$

$$CIACR = 0.2172[0.2302\bar{D}_r^2 + 15823\bar{D}_r^3 - 4.168{\times}10^6\bar{D}_r^4 \\ + 4.920{\times}10^8\bar{D}_r^5 - 2.133{\times}10^{10}\bar{D}_r^6]n_i n_r f_i f_r. \tag{B.44}$$

Ice crystal initiation through vapor nucleation was handled as Ferrier (1994) for temperatures less than -5°C. The mass rate was given as

$$QIINT = \delta\frac{m_i}{\rho_0}\max(0,w)\frac{\partial N_{in}}{\partial z}, \tag{B.45}$$

where n_{in} is given by

$$N_{in} = 50\left[\frac{q_v - q_{is}}{q_{ws} - q_{is}}\right]^{\alpha_1}\exp(-\beta_1 T_c) \tag{B.46}$$

and m_i is the assumed mass of $6.88{\times}10^{-13}$ kg for the nucleated crystal. The variables α_1 and β_1 are 4.5 and 0.6, respectively, following Meyers et al. (1992). The number of ice crystals nucleated was therefore

$$CIINT = \left(\frac{\rho_0}{m_i}\right)QIINT. \tag{B.47}$$

Cloud ice produced through rime splintering followed Ziegler et al. (1986). For the range between -2 and -8°C, or

$$F(T) = \begin{cases} -(T+2)(T+8)/9 & -8^\circ < T < -2^\circ C \\ 0 & else, \end{cases} \tag{B.48}$$

ice multiplication was given by

$$CHMUL1 = \frac{F(T){\times}\exp(-7.23{\times}10^{-15})}{250v_c}CHACW \tag{B.49}$$

$$QHMUL1 = \frac{1.504{\times}10^{-11}}{\rho_0}CHMUL1. \tag{B.50}$$

Appendix C

List of microphysical terms and symbols

Table C.1: List of symbols.

Symbol	Description
a	empirical constant for charge separation
a_1	accretion constant
a_2	accretion constant
a_h	fall speed constant for graupel
A	empirical constant for charge separation
A'	raindrop freezing coefficient
A_n	term in distribution function
A_x	collection coefficients from Seifert and Beheng (2006)
b	empirical constant for charge separation
b_h	fall speed constant for graupel
B	buoyancy
B_n	term in distribution function
B'	raindrop freezing coefficient
B_{xy}	collection coefficients from Seifert and Beheng (2006)
$\bar{c}$	speed of sound
c_{r1}	rime density coefficient
c_{r2}	rime density coefficient
C_d	drag coefficient
C_e	turbulence coefficient
C_i	specific heat of ice
C_m	turbulence coefficient
C_p	specific heat of air at constant pressure
C_w	specific heat of water
C_y	collection coefficients from Seifert and Beheng (2006)
D	particle diameter
D_i	turbulent mixing term for momentum
$D_{n,w}$	cloud droplet characteristic diameter
$D_{n,h}$	graupel characteristic diameter
$D_{n,s}$	snow characteristic diameter
D_θ	turbulent mixing term for temperature
D_{q_i}	turbulent mixing terms for mixing ratios
D_{ui}	turbulent mixing terms
$\bar{D}_i$	mean ice diameter
$\bar{D}_r$	mean rain diameter
$\bar{D}_w$	mean cloud droplet diameter

Symbol	Description
E	sub-grid scale kinetic energy
E_{gw}	graupel-droplet collection efficiency
E_r	rebound probability for inductive charging
E_{ref}	reference electric field for Canosa and List (1993)
E_{rs}	collection efficiency for rain with snow in Canosa and List (1993)
E_{w0}	function for rain self-collection
E_{xy}	collection efficiency between components x and y
E_z	vertical component of the electric field
EW	effective liquid water content
f_i	fraction of ice crystals above threshold diameter
f_j	Coriolis parameter
f_r	fraction of raindrops above threshold diameter
F_{dgt}	fraction of droplets experiencing grazing trajectories
F_{fmh}	maximum freezing rate for graupel
F_{fms}	maximum freezing rate for snow
F_h	ventillation coefficient for graupel
F_{hwm}	liquid water fraction for mixed-phase graupel
F_{qlh}	maximum liquid mass available to freeze on graupel
F_{qls}	maximum liquid mass available to freeze on snow
F_{qzh}	heat balance equation for graupel
F_{qzr}	heat balance equation for rain
F_{qzs}	heat balance equation for snow
F_r	ventillation coefficient for rain
F_s	ventillation coefficient for snow
F_{swm}	liquid water fraction for mixed-phase snow
g	gravitational acceleration
G	background cosmic ray ion generation rate
K_a	thermal conductivity of air
K_{frag}	rate of mechanical ice fragmentation of snow
K_h	eddy mixing coefficient
K_m	momentum eddy mixing coefficient
l	turbulent length scale
L_2	assumed mass of droplets for autoconversion
L_f	latent heat of fusion
L_v	latent heat of vaporization
m_i	assumed mass of nucleated ice crystal, 6.88×10^{-13} kg
M_1	melting constant
M_2	melting constant
M_{frag}	assumed mass for mechanical ice fragments
M_θ	microphysical sources/sinks for temperature
M_{q_n}	microphysical sources/sinks for mixing ratio
$n_\pm$	ion concentration
n_{0h}	number concentration intercept for graupel
$n_{l\pm}$	large ion concentration
n_x	particle distribution for species x
N_{in}	concentration of nucleated ice crystals
N_x	graupel concentration for species x
Pr	Prandtl number
q	charge acquired during melting process
q^*	preliminary estimate for total mixed-phase mixing ratio
q_-	event charge separation for negatively charging hydrometeor
q_+	event charge separation for positively charging hydrometeor
q_h	graupel mixing ratio

Symbol	Description
q_h^*	preliminary estimate for total mixed-phase graupel mixing ratio
q_{hw}	liquid water portion of mixing ratio for mixed-phase graupel
q_{hw}^*	preliminary estimate for liquid water portion of graupel mixing ratio
q_{ice}	mixing ratio of hydrometeors in solid phase
q_{is}	ice saturation mixing ratio
q_{liq}	mixing ratio of hydrometeors in liquid phase
q_n	mixing ratios for hydrometeors
q_{naz}	event charge separation in anomalous zones
q_r	rain mixing ratio
q_s	snow mixing ratio
q_s^*	preliminary estimate for total mixed-phase snow mixing ratio
$q_{ss}(0)$	water saturation mixing ratio at 0°C
q_{sw}	liquid water portion of mixing ratio for mixed-phase snow
q_{sw}^*	preliminary estimate for liquid water portion of snow mixing ratio
q_v	water vapor mixing ratio
$\bar{q}_v$	mean water vapor mixing ratio
q_w	cloud droplet mixing ratio
q_{ws}	water saturation mixing ratio
$\delta q'_{xy}$	charge transferred per collision
r_b	variance-scaled droplet radius
$\bar{R}_w$	mean cloud droplet radius
R_d	gas constant for dry air
RAR	rime accretion rate
RAR_{crit}	critical value of rime accretion rate for charge reversal
S	sub-grid momentum term
S_{att}	ion attachment rate
S_{evap}	release of charge from complete evaporation of hydrometeor
S_{ltg}	charge removal from lightning flash
S_{pd}	point discharge current from the surface
$Sc^{\frac{1}{3}}$	Schmidt number
T	temperature
T_c	temperature in °C
u'	perturbation wind
u_i	three-dimensional wind vector
$\bar{u}$	mean wind
v	particle volume
$\bar{v}_x$	mean particle volume for species x
V	mass-weighted fall speed
V_h	fall speed of graupel
V_r	fall speed of rain
V_s	fall speed of snow
V_w	fall speed for cloud droplet
V_x	fall speed for species x
W_1	wet growth constant
W_2	wet growth constant
α	shape parameter
α_1	exponent in ice nucleation following Meyers et al. (1992)
α_h	shape parameter for graupel
α_r	shape parameter for rain
β_1	exponent in ice nucleation following Meyers et al. (1992)
Γ	Gamma function
δ	step function for temperature $>$ or $\leq$ 0°C
δ_{ij}	Kronecker delta

Symbol	Description
ϵ	collection kernel ratio from Zrnić et al. (1993)
ϵ_a	permittivity of air
ε_{ijk}	Levi-Civita function in three dimensions
θ	potential temperature
θ'	perturbation potential temperature
θ_e	equivalent potential temperature
$\bar{\theta}$	mean potential temperature
$\bar{\theta}_v$	mean virtual potential temperature
$cos\theta$	graupel-droplet collisional angle
μ	exponent in size distribution
$\mu_\pm$	ion mobility
ν	shape parameter
ν_k	kinematic viscosity
ν_r	shape parameter for rain
ν_w	shape parameter for cloud water
π'	exner function perturbation pressure
ρ	density
$\bar{\rho}$	mean density
ρ_0	surface air density
ρ_{00}	reference MSL air density
ρ_{0h}	reference graupel density
ρ_a	air density
ρ_h	graupel density
ρ_i	ice density
ρ_r	rain density
ρ_w	cloud water density
$\rho_{x,rime}$	rime density
ϱ	charge density
ϱ_h	graupel charge
ϱ_{xy}	charge separation rate between two hydrometeor species
τ	time scale used for autoconversion
ϕ	electrical potential
ψ	diffusivity of water vapor in air

Table C.2: List of source and sink terms used for mixing ratio prediction

Term	Description
QHACI	Graupel collection of cloud ice
QHACR	Graupel colleciton of rain
QHACS	Graupel colleciton of snow
QHACW	Graupel collection of cloud water
QHCEV	Evaporation of wet graupel
QHCNI	Conversion of cloud ice to graupel
QHCNS	Conversion of snow to graupel
QHDPV	Graupel deposition
QHFZH	Freezing rate of mixed-phase graupel
QHMLR	Melting rate of mixed-phase graupel
QHMUL1	Ice multiplication through rime splintering
QHSBV	Sublimation of graupel
QHSHR	Liquid water shedding from graupel into rain
QIACR	Heterogenous freezing of rain into ice
QIACRF	Graupel conversion through ice interaction with rain
QIACW	Cloud ice collection of cloud water
QICICHR	Hobbs-Rangno ice enhancement following Ferrier (1994)
QIDPV	Ice deposition
QIINT	Vapor nucleation of ice
QIMLR	Cloud ice melting to rain
QISBV	Sublimation of cloud ice
QRACI	Rain collection of ice
QRACIF	Graupel conversion through rain interaction with ice
QRACW	Accretion
QRCEV	Rain evaporation
QRCNW	Autoconversion
QRFRZ	Homogeneous freezing of rain following Bigg (1953)
QSACI	Snow collection of ice
QSACR	Snow collection of rain
QSACW	Snow colleciton of cloud water
QSCEV	Snow evaporation
QSCNI	Conversion of cloud ice to snow
QSDPV	Snow deposition
QSFZS	Freezing rate of mixed-phase snow
QSMLR	Melting rate of mixed-phase snow
QSMUL	Ice multiplication from snow fragmentation
QSSBV	Sublimation of snow
QSSHR	Liquid water shedding from mixed-phase snow into rain
QWCTFZC	Contact freezing nucleation
QWFRZC	Homogeneous freezing of cloud drops following Bigg (1953)

Table C.3: List of source and sink terms used for number concentration prediction

Term	Description
CAUTN	Autoconversion of cloud water to rain
CHACI	Graupel collection of hail
CHACR	Graupel collection of rain
CHACS	Graupel collection of snow
CHACW	Graupel collection of cloud water
CHCNI	Autoconversion of cloud ice to graupel
CHCNS	Autoconversion of snow to graupel
CHMLR	Complete melting of graupel to rain
CHMUL1	Ice multiplication through rime splintering
CHSBV	Vaporization of wet graupel
CHSHR	Rain shed from wet graupel
CIACR	Cloud ice interactions with rain
CIACW	Cloud ice interactions with cloud water
CICICHR	Hobbs-Rangno cloud ice enhancement
CIINT	Vapor nucleation of ice
CIMLR	Complete melting of cloud ice to rain
CISBV	Vaporization of cloud ice
CRACI	Rain collection of ice
CRACR	Rain self-collection
CRACW	Rain collection of water
CRCEV	Evaporation
CRCNW	Autoconversion of cloud water to rain
CRFRZ	Homogeneous freezing of rain
CSACI	Snow collection of cloud ice
CSACS	Snow aggregation
CSACW	Snow collection of cloud water
CSCNI	Autoconversion of cloud ice to snow
CSMLR	Complete melting of snow to rain
CSMUL	Ice multiplication through snow fracturing
CSSBV	Vaporization of wet snow
CSSHR	Rain shed from wet snow
CWCTFZC	Contact freezing nucleation
CWFRZC	Homogeneous freezing of cloud water